




UNIVERSITÀ
DEGLI STUDI
DI PADOVA

UNIVERSITA' DEGLI STUDI DI PADOVA

Dipartimento di Ingegneria Industriale DII

Corso di Laurea Magistrale in Ingegneria Aerospaziale

IMPACT OF A FAN SIMULATOR ON A COMPLEX AERO-ENGINE
INTAKE AERODYNAMICS

Relatore: Prof. Ernesto Benini 

Correlatore: Prof. David Macmanus, Dr. Pavlos Zachos

Matteo Alpe con matricola

1128568

Anno Accademico 2016/2017

ABSTRACT

Convoluted aero-engine intakes have become increasingly important over the last few years due to their application in the most recent aircraft used in military and civil aviation. New technologies and configurations, such as distributed propulsion or highly integrated engines for the aircraft of the future, have enhanced the interest in smaller, lighter systems. Significant effort and resources have been invested in complex new installations in order to meet the new requirements. In this context, S-ducts play an important role in the design and development of such systems. The geometry of an S-Duct causes distortion of the flow inside the duct itself, thus affecting the system downstream. For this reason, it is paramount to understand and properly describe the flow field in the duct in order to quantify and characterise its impact on the turbomachinery, and so avoid any unwanted decrease in the performance of the engine. The aim of this project was to study the flow field inside the duct and to analyse the impact on the flow of a static fan simulator placed at the exit, compared with the results for the duct without static fan. The study was conducted using CFD tools (ICEM CFD and Fluent) and applied both a steady (RANS) and a transient (DDES) analysis in order to describe the unsteady nature of the flow. Post-processing of the results involved studying different contours of RANS and time-averaged DDES. In addition, descriptors of the distortion were carefully studied. Finally, after an exhaustive analysis of a new method of post-processing called Dynamic Mode Decomposition (DMD), a first attempt at applying the model was made.

The results revealed a negligible impact of the fan simulator on the upstream region of the duct, but a substantial decrease in flow distortion levels and a reshape of the flow at the exit plane of the S-duct (AIP), when compared with the duct without fan. The engine face has an important effect on the flow and the study made enhanced the scientific knowledge of this phenomena.

Keywords:

S-Duct, Detached Eddy Simulation, Distortion descriptors, DMD.

ACKNOWLEDGEMENTS

First of all, my gratitude goes to Dr Pavlos Zachos and Prof. David MacManus to accept me inside the Complex Intakes group, giving me the possibility not only to develop my technical knowledge but also teaching me how to work and behave in a high-pressure environment. A special thank also goes to Daniel Gil-Prieto who helped me in many difficult situations during this project.

In addition, I would like to thank Prof E. Benini from Università degli Studi di Padova who gave me the possibility to attend the MSc in Thermal Power at Cranfield University and who helped throughout this challenging year.

The greatest gratitude goes to my family: my father, my mother and my brother. Their continuous support not only during this whole year, but during all my academic life helped me to overcome all the hard situations I encountered. Without them, all I have achieved so far it would not have been possible.

I would like to thank also my Uncle Paolo and Aunt Silvana for the support, the guidance and the interest shown during all my studies.

A final thank to all the friends in Italy and in Cranfield University who supported or accompanied me during this adventure that I will never forget.

TABLE OF CONTENTS

ABSTRACT	i
ACKNOWLEDGEMENTS.....	ii
LIST OF FIGURES.....	v
LIST OF TABLES	x
LIST OF EQUATIONS.....	xi
LIST OF ABBREVIATIONS	xiv
1 INTRODUCTION.....	17
1.1 Background.....	17
1.2 Aims and Objectives	18
2 LITERATURE REVIEW	21
2.1 Flow Distortion	21
2.1.1 Performance of the intake	22
2.1.2 Previous investigations of S-ducts.....	25
2.1.3 Flow Distortion.....	31
2.1.4 Action of distortion on the engine	34
2.1.5 Distortion Descriptors	41
2.1.6 Impact of the engine on flow unsteadiness	48
2.2 Topology of the flow.....	52
2.2.1 Separation and reattachment	53
2.2.2 Structure of the vortices	55
2.3 Computational Fluid Dynamics: fundamentals.....	56
2.3.1 RANS	57
2.3.2 LES and DES	59
2.4 Summary	61
2.4.1 Most recent developments	61
2.4.2 State of the art and project roadmap	65
3 METHODOLOGY	67
3.1 Geometry	67
3.2 Mesh	71
3.2.1 Approach and quality of the mesh	71
3.2.2 Mesh similarity and mesh requirements	76
3.3 Simulations	79
3.3.1 RANS	79
3.3.2 DDES	84
3.4 Post-processing	86
3.4.1 RANS	86
3.4.2 DDES	87
4 RESULTS.....	89
4.1 Sensitivity analysis.....	89
4.2 Resolution of the Boundary Layer: Y^+	91

4.3 Flow field Characteristic.....	93
4.3.1 RANS	94
4.3.2 DDES	100
4.3.3 Comparison of RANS and DDES	103
4.4 Separation	104
4.5 Comparison: fan case vs no fan case	108
4.6 Descriptors of the distortion	114
4.6.1 Distortion statistics: AIP.....	114
4.6.2 Swirl descriptors at different rings of the AIP	120
5 ADVANCED PROCESSING METHODS.....	129
5.1 Dynamic mode decomposition: recent applications and studies	129
5.2 DMD and SP-DMD: methodology	134
5.2.1 Mathematical background of DMD and SP-DMD	135
5.3 Application of Dynamics Mode Decomposition	142
5.3.1 Verification of MATLAB code for SP-DMD analysis	142
5.3.2 DMD code applied to DDES data.....	148
6 CONCLUSIONS AND RECCOMENDATIONS.....	151
6.1 Main findings.....	151
6.2 Recommendations for future research.....	154
REFERENCES	157
APPENDICES	165

LIST OF FIGURES

Figure 2-1 Example of unsteadiness in an S-duct from ONERA experiment [14]; Schlieren-like visualisation of flow on the symmetry plane and at the AIP from a DES simulation.....	21
Figure 2-2 General arrangement of a turbofan engine with an intake for subsonic applications [17].....	22
Figure 2-3 Convoluted intake in a rear engine configuration for commercial aircraft [17].....	23
Figure 2-4 Simple schematic to show the interface between engine, intake and the AIP position.	23
Figure 2-5 Example from RANS simulation of S-duct flow characteristics; a) Swirl angle distribution, b) total pressure (right) distribution at the AIP, c) wall streak-line [20].....	26
Figure 2-6 Swirl Angle definition [11].....	26
Figure 2-7 Geometry, parameters definition and plane position in the system studied by Wellborn et al. [21].	27
Figure 2-8 Flow field of Wellborn's S-duct [21]. A) crossflows due to action of pressure gradients, B) Recirculation, C) axial flow at the exit.....	28
Figure 2-9 Total pressure distribution at different planes in the wellborn experiment [21].....	29
Figure 2-10 Total pressure distribution at the AIP using both transient and steady methods, compared with experimental data [14].....	30
Figure 2-11 Comparison between RANS and ZLES with the experimental data of Wellborn et al. [6].....	30
Figure 2-12 Shape of double bend S-duct and total pressure distribution at the AIP from a CFD calculation [11].	32
Figure 2-13 Flow evolution inside a double bend S-duct [11].....	32
Figure 2-14 Twin swirl pair at the AIP of an S-Duct [11].....	33
Figure 2-15 Twin swirl formation in a S-duct [11].	34
Figure 2-16 Bulk Swirl formation in an S-duct [11].	35
Figure 2-17 Three staged fan map change due to distortion [19].	36
Figure 2-18 Position and types of distortion in a turbofan engine [16].....	37
Figure 2-19 Action of the bulk swirl on the rotor blades [11].....	38
Figure 2-20 Coupling of total pressure and swirl [11].	39

Figure 2-21 Definition of the parameters by SAE committee [11].	40
Figure 2-22 example of θ section of the spoiled region at the compressor face [16].	42
Figure 2-23 a) critical sector angle; b) division of the AIP surface in rakes [15].	43
Figure 2-24 Swirl angle for one-per-revolution symmetric paired swirl [11].	46
Figure 2-25 Swirl directivity in one revolution for different swirl patterns [11].	47
Figure 2-26 Swirl pairs in one revolution for different swirl patterns [11].	48
Figure 2-27 Inlet engine flow field in the wind milling rotor [25].	49
Figure 2-28 Effect of the engine on the flow inside the intake [26].	50
Figure 2-29 Inlet total pressure distortion levels in: (a) uncoupled case, (b) fan and intake coupled system, (c) choked coupled system [26].	51
Figure 2-30 a) Short compressor flow redistribution b) Long compressor flow redistribution [27].	52
Figure 2-31 Skin friction lines; separation and attachment [28].	53
Figure 2-32 Separation and reattachment; away from the wall [28].	54
Figure 2-33 General vortex structure and particularly: “tornado-like vortex” (a) and (b) [28].	55
Figure 2-34 Horsehoe vortex structure; (a) 3D representation, (b) plane section [28].	56
Figure 2-35 Characterization and field of application of different CFD models [29].	58
Figure 2-36 Comparison of the normalised velocity in the three directions and swirl angle at the AIP between DDES (time-averaged flow field) and SPIV [9].	62
Figure 2-37 Pressure recovery coefficient and Swirl (with standard deviations) for different offsets H/L [2].	64
Figure 2-38 joint PDF maps: SD-SP swirl descriptors; a) High Offset, b) Low offset [4].	64
Figure 2-39 Road map of the thesis project.	66
Figure 3-1 3D representation of the system.	68
Figure 3-2 Schematic of the S-duct and representation of the nomenclature used.	68
Figure 3-3 Fan simulator used by Cranfield University in the experiments [8].	69

Figure 3-4 Regions of the Fan simulator and position of the spinner; 1. Cylinder, 2. Blades, 3. Spinner.	70
Figure 3-5 Qualitative schematic of the position of each plane (p. abbreviation for plane).	72
Figure 3-6 Non-conformal mesh and different location of the nodes.	73
Figure 3-7 a) Mesh structure of the S-duct from inlet (right) to the interface (left), b) perpendicular section of the mesh of the duct.	75
Figure 3-8 Mesh of the spinner and final part of the S-Duct.	76
Figure 3-9 Mesh of the fan simulator.	77
Figure 3-10 Mesh of the clean case (no fan simulator) made by A. Soli [12]....	79
Figure 3-11 Boundary conditions for the control volume of the system.	81
Figure 3-12 Inlet total pressure profile.	82
Figure 3-13 Residuals of RANS simulation	83
Figure 3-14 a) Mass flow at the inlet; b) Mass flow check; c) Inlet Mach number; d) Total pressure at the AIP plane; RANS simulation	83
Figure 3-15 Residuals of the last 15 convective times simulation; zoomed section in order to see the behaviour of the scaled residuals.	85
Figure 3-16 a) Mass flow at the inlet; b) Inlet Mach number; c) Total pressure at the AIP plane	87
Figure 4-1 Graphical representation of the change in the descriptors on increasing the number of nodes (N).	91
Figure 4-2 Y^+ along the walls of the S-duct; from inlet to the AIP.	92
Figure 4-3 2D view on three sides of the S-duct; from inlet to AIP.	93
Figure 4-4 Y^+ in the fan simulator.	93
Figure 4-5 Mach distribution along the symmetry plane; RANS simulation.	95
Figure 4-6 w-component of velocity at different planes; RANS simulation.	95
Figure 4-7 Static pressure coefficient distribution along the symmetry plane; RANS simulation.	96
Figure 4-8 u-component of velocity at different planes; RANS simulation.	97
Figure 4-9 v-component of velocity at different planes; RANS simulation.	99
Figure 4-10 Pressure recovery coefficient at different planes and along the symmetry plane; RANS simulation.	99

Figure 4-11 u-velocity at the AIP plane and along the symmetry plane; time-averaged DDES simulation.....	100
Figure 4-12 v-velocity at the AIP plane and along the symmetry plane; time-averaged DDES simulation.....	101
Figure 4-13 w-velocity at the AIP plane and along the symmetry plane; time-averaged DDES simulation.....	102
Figure 4-14 Comparison of PR between time averaged DDES and RANS at the AIP.....	104
Figure 4-15 Static pressure distribution along the wall and standard deviation.	105
Figure 4-16 Time averaged shear stress; general distribution of the shear stress along the wall of the S-duct.	106
Figure 4-17 a) Skin friction lines along the wall; b) Schematic of the separation structure [42].....	107
Figure 4-18 Comparison between U-velocities, standard deviation and streamlines at the AIP plane; time-averaged DDES.	109
Figure 4-19 Comparison between Mach numbers at the AIP and symmetry plane; time-averaged DDES.....	110
Figure 4-20 Comparison between PR values and correspondent standard deviation at AIP plane; time-averaged DDES.	112
Figure 4-21 Comparison of pressure coefficient and correspondent standard deviation at the AIP section; time-averaged DDES.	113
Figure 4-22 Ring arrangement in a general section.	114
Figure 4-23 Cloud maps investigating distortion descriptors at AIP plane.....	119
Figure 4-24 Description of the SD-SP map [4].	121
Figure 4-25 SP-SD cloud maps; Comparison of the two DDES simulations at the AIP.....	122
Figure 4-26 SI-SD cloud maps; Comparison of the two DDES simulations at the AIP.....	123
Figure 4-27 SI-SP cloud maps; Comparison of the two DDES simulations at the AIP.....	124
Figure 5-1 Modes and reconstructed flow over a flat plate with SP-DMD [47].	130
Figure 5-2 a) time evolution mode 2, b) magnitude mode 2, c) phase mode 2 [47].....	130

Figure 5-3 Pressure and axial velocity peaks from S-P DMD, NPR=14.67 [48].	132
Figure 5-4 Ovalization mode on symmetry plane and axial plane from SP-DMD analysis [48]......	132
Figure 5-5 Comparison between POD and DMD spatial mode; c) TR-PIV location on the LPT blade [39]......	133
Figure 5-6 Growth rate distribution and comparison between DMD and POD temporal frequency [49]......	133
Figure 5-7 Description of eq. (5-8) in DMD; meaning of each matrix [47]......	139
Figure 5-8 General map of the algorithm used to implement DMD method....	140
Figure 5-9 Sparsity-promoting algorithm.	141
Figure 5-10 a) Geometry used for the LES simulation of the screeching supersonic jet; b) train of diamond-shaped shock cells in static temperature contour [57]......	143
Figure 5-11 Comparison between amplitude vs frequency plots of Jovanović et al. scientific paper and the MATLAB code; Agreement is found [49].	145
Figure 5-12 Comparison of performance loss plots and number of modes of Jovanović et al. scientific paper and the MATLAB code; Agreement is found [49]......	145
Figure 5-13 a) Eigenvalues resulting from standard DMD algorithm (circles) and the selected eigenvalues from SP-DMD algorithm (crosses); b) Correspondent amplitude of modes; a)-b) from MATLAB code.	147
Figure 5-14 Eigenvalues resulting from standard DMD algorithm (circles) and the selected eigenvalues from SP-DMD algorithm (crosses) and correspondent amplitudes for a lower number of optimal modes Nz ; MATLAB code.	147
Figure 5-15 a) Amplitude vs frequency of the eigenvalues; b-c) Amplitude vs Real part eigenvalues; MATLAB code applied on DDES data of the fan simulator case.	149

LIST OF TABLES

Table 1 S-duct parameters [4].	63
Table 2 Summary of the leading dimensions.	70
Table 3 Summary of the position of each plane of interest.	71
Table 4 Position of the interfaces.	73
Table 5 Nodes and quality; first region of the mesh.	74
Table 6 Nodes and quality; second region of the mesh.	75
Table 7 Nodes and quality; third region of the mesh.	76
Table 8 comparison between the mesh used in this project and A. Soli's mesh.	78
Table 9 Oscillation levels compared to RANS converged value.	86
Table 10 Parameters of the sensitivity analysis.	90
Table 11 Summary of distortion statistics at the AIP plane for time-averaged DDES and RANS.	117
Table 12 Probability P of a phenomena to appear over the area range SPxSD	125
Table 13 Probability P of a phenomena to appear over the area range SixSD	126

LIST OF EQUATIONS

(2-1).....	24
(2-2).....	24
(2-3).....	25
(2-4).....	40
(2-5).....	40
(2-6).....	40
(2-7).....	41
(2-8).....	41
(2-9).....	43
(2-10).....	43
(2-11).....	43
(2-12).....	44
(2-13).....	44
(2-14).....	44
(2-15).....	44
(2-16).....	44
(2-17).....	45
(2-18).....	45
(2-19).....	46
(2-20).....	46
(2-21).....	47
(2-22).....	47
(2-23).....	47
(2-24).....	54
(2-25).....	57
(2-26).....	58
(2-27).....	58
(2-28).....	59

(2-29).....	59
(2-30).....	59
(4-1).....	89
(4-2).....	89
(4-3).....	89
(4-4).....	89
(4-5).....	90
(4-6).....	118
(4-7).....	118
(4-8).....	120
(5-1).....	135
(5-2).....	136
(5-3).....	136
(5-4).....	136
(5-5).....	137
(5-6).....	137
(5-7).....	138
(5-8).....	138
(5-9).....	139
(5-10).....	140
(5-11).....	140
(5-12).....	140
(A-1).....	158
(A-2).....	158
(A-3).....	160
(A-4).....	161
(B-1).....	161
(B-2).....	162
(B-3).....	162

(B-4).....	163
(B-5).....	163
(B-6).....	163
(B-7).....	163
(B-8).....	163
(B-9).....	163
(B-10).....	164
(B-11).....	164

LIST OF ABBREVIATIONS

Acronyms

AIP	Aerodynamic Interface Plane
ARP	Aerospace Recommended Practice
AR	Area Ratio
BL	Boundary Layer
BC	Boundary Condition
CFD	Computational Fluid Dynamics
DES	Detached Eddy Simulation
DDES	Delayed Detached Eddy Simulation
DMD	Dynamic Mode Decomposition
DNS	Direct Numerical Simulation
GCI	Grid Convergence Index
HPC	High pressure compressor
IGV	Inlet Guide Vane
IPC	Intermediate pressure compressor
IPT	Intermediate pressure turbine
LPC	Low pressure compressor
LPT	Low pressure turbine
LES	Large Eddy Simulation
PIV	Particle Image Velocimetry
RANS	Reynolds Averaged Navier Stokes
SAE	Society of Automotive Engineers
SPIV	Stereo Particle Image Velocimetry
SST	Shear Stress Transport
SVD	Singular Value Decomposition
SP-DMD	Sparsity-Promoting Dynamic Mode Decomposition
TKE	Turbulent Kinetic Energy
TR-PIV	Time Reconstructed Particle Image Velocimetry

Symbols

x, y, z	System of reference coordinates
---------	---------------------------------

D	S-Duct cross section diameter, [m]
R	S-Duct cross section radius, [m]
R_c	S-Duct curvature radius, [m]
R_{in}	S-Duct inlet radius, [m]
H	S-Duct centreline offset, [m]
L	S-Duct axial length, [m]
s	S-Duct centreline coordinate, [m]
u, v, w	Velocity vector Cartesian components, [m/s]
M	Mach number
Re	Reynolds number
St	Strouhal number
V_{in}	In-Plane Velocity, [m/s]
t_c	S-Duct Convective time, [s]
c_p	Pressure coefficient
Δt	DDES simulation time step, [s]
R_c	Curvature Radius of the S-Duct bend, [m]
\dot{m}	Mass flow, [kg/s]
y+	Non-dimensional wall distance
P_0	Total Pressure, [Pa]
T_0	Total Temperature, [K]
p	Static Pressure, [Pa]
t	Static temperature, [K]
α	Swirl Angle, [°]
U_θ	Circumferential Velocity, [m/s]
PR	Pressure Recovery
MPR	Multiple-per-revolution
SI	Swirl Intensity
SD	Swirl Directivity
SP	Swirl Pairs
CI	Circumferential Intensity
RI	Radial Intensity
DC60	Total Pressure Distortion Coefficient
SC60	Swirl Distortion Coefficient

CDI	Circumferential Distortion Index
RDI	Radial Distortion Index

Subscripts

In	S-Duct Inlet Plane
Out	S-Duct Outlet Plane
AIP	S-Duct AIP

Operators

$\langle \cdot \rangle$	Time-averaged value
$(\cdot)^*$	Conjugate-transpose of a matrix
\cdot	Elementwise multiplication of two matrices
$(\cdot)^T$	Transpose of a matrix

Reference values

$D_{ref} = 150 \text{ mm}$	Reference diameter
$w_{ref} = 60 \text{ m/s}$	Reference axial velocity
$P_{0,ref} = 99.25 \text{ kPa}$	Reference total pressure
$P_{0,in} = 100.0 \text{ kPa}$	Inlet total pressure
$M_{ref} = 0.27$	Reference Mach number

1 INTRODUCTION

1.1 Background

Ducts of different shapes are present in aero engines in order to connect and link different parts and components. Due to the impact on the performance of the system [1], one of the most important ducts is at the front of the engine, namely the intake, and, depending on the application, different types of installations can be observed. During recent years interest in S-ducts, in other words ducts with an “S” shape, has grown especially where configurations of embedded or partially embedded systems are concerned [2]. The reasons for this growth in interest lie not only in the critical requirements of size, compactness and performance of the intake system [3], but also because of the scientific effort and resources invested in research into distributed propulsion, an innovative approach to the design of future aircraft [4]. In this context, due to the different positions in which the engine is placed, a shaped duct was needed to connect the inlet to the rest of the aero engine intake systems.

In the aviation history there are many examples of aircraft using this technology [5] and particularly in the case of commercial aircraft, a shaped duct was adopted to meet the requirements of engine design. For example, in the Lockheed L-1011 TriStar, Boeing 727 or in a narrow-body airliner like the Tupolev Tu-154M [5], in order to align the thrust produced by a third rear engine with the thrust of two conventional engines and the axis of the airplane, an S-duct was needed. In terms of benefits, the presence of this innovative thrust production system, compared to a “straight-through” layout, mainly achieves a decrease in the system’s total weight and total drag of the aircraft [6]. Nowadays, three engines are no longer used in large commercial airplanes, mainly because the power and reliability of the most recent engines is much greater compared to the ones in the 1970s. Nevertheless, business aircraft such as Dassault Falcon 7X and the Dassault Falcon 900 [5], still use a tri-jet configuration with an S-duct in the central engine to connect the inlet located below the stabilizer to the exhaust at the rear of the plane.

Interest in this technology is not only related to civil aircraft; in the last few years in particular, due to increases in the demand for highly integrated engines for military applications, a renewed interest in S-duct has been observed. This is particularly true for both manned and unmanned vehicles where different in sizes, weights and performance of the shaped duct are needed.

In addition, not only can more efficient aircraft design be achieved with reduction in drag and weight [4], but a decrease in noise levels can be observed. This is a critical aspect especially in civil applications given the strict legislations on noise near airports and in highly populated areas [7].

The biggest challenge related to shaped ducts is the creation of flow distortion [8] and flow separation [9] which affects the performance of systems downstream, namely after the exit plane of the S-duct, conventionally referred to as the Aerodynamic Interface Plane (AIP) [10]. In particular, high levels of flow distortion and unsteadiness are observed at the AIP [10], affecting a possible compressor first stage relatively close to it [1]. These undesired flow phenomena lead to an increase in total pressure, a reduction in compressor flow capacity and in turn a significant decrease in surge margin observed in the compressor map [11].

Consequently, the combination of the benefits of an S-duct and the problems related to the integration of such complex intake configurations in the engine have led to numerous studies employing both experimental and CFD techniques.

1.2 Aims and Objectives

The aim of this work is to assess the impact of a static fan simulator on the flow inside the S-Duct and, in particular, to compare the results obtained with the data from a configuration without a static fan model at the exit. The results from the clean case were presented and fully described by both A. Soli [12] and F. Wilson [13] in their Cranfield University MSc Thesis.

Firstly, starting from the geometry, the mesh is made by adopting a non-conformal approach in ICEM. Secondly, a RANS simulation of the flow will be

carried out on Fluent in order to have an initial comprehension of the averaged flow field. At the same time, a comparison of the results with the clean case and the determination of the position of the flow separation will be done. Nevertheless, due to the nature of the steady simulation applied, namely pure RANS, it is not possible to detect unsteadiness.

For this reason, a DDES transient simulation will be applied in order to capture the unsteadiness and better describe the unwanted flow phenomena which negatively affect any systems downstream. The calculation will be done on different planes in the duct and in the fan region, considering in particular the AIP, which corresponds to the exit of the duct.

The objective is to determine the changes in the flow field due to the presence of a fan simulator at a flow Mach number of 0.27 in the case of an high off-set geometry of the duct. The geometry of the static fan is simple and consists of spinner at the front, subsonic blades to choke the flow at the throat and the central cylinder. In this way, namely choking the flow, it is possible to approximate the behaviour of a rotor using a much simpler static configuration [2]. The spinner is wholly inside the S-Duct and in particular the AIP plane corresponds exactly to the end of the spinner region. In this position, the effect of the static fan on the flow field is at its maximum and the largest impact will be observed.

Finally post-processing will be carried out in order to better quantify the distortion levels inside the duct and obtain a real understanding of the impact of the fan simulator. Basic analysis of flow distortion patterns and flow distortion descriptors was applied. Moreover, a lot of effort was put into the understanding, description and implementation of a new cutting edge method to post process the transient data. It is called Dynamic Mode Decomposition (DMD).

2 LITERATURE REVIEW

This section will provide the background which will help us to understand the results presented in the later chapters. In particular the description of the state-of-the-art of S-ducts will be based mainly on previous studies conducted at Cranfield University. A brief introduction to the basics of flow distortion will be followed by the characterization of a three-dimensional flow and a brief description of the CFD models adopted. Finally, in the summary, the most recent developments from Cranfield University will be presented

2.1 Flow Distortion

The aim of this section is to briefly present and characterize the general distortion of the flow associated with a complex installation (Figure 2-1). Firstly, the impact of distortion levels on intake performance is presented, followed by a discussion of the implications of distorted flow generated by an S-duct in the engine performance. Finally, the most common descriptors used to analyse the distorted flow as assessed by SAE will be presented.

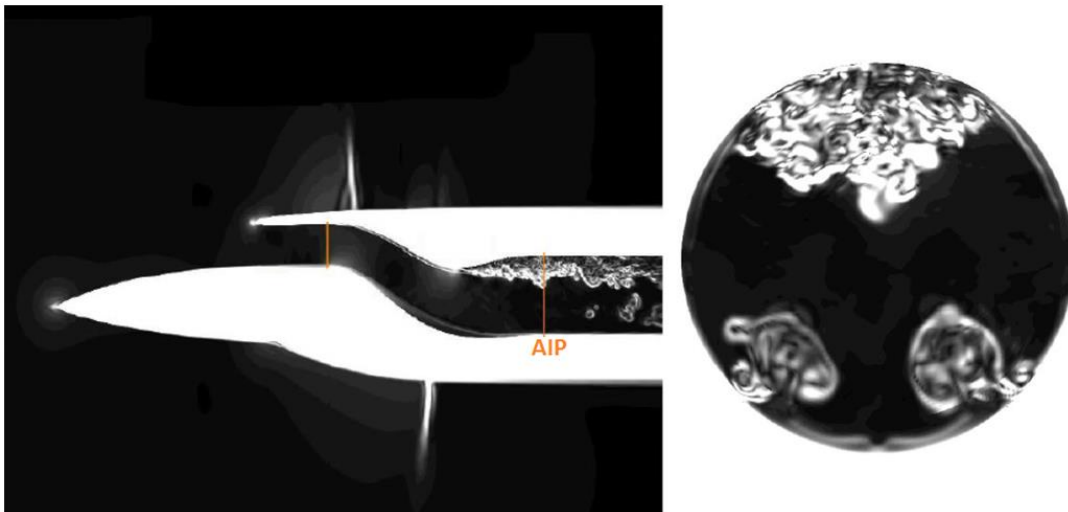


Figure 2-1 Example of unsteadiness in an S-duct from ONERA experiment [14]; Schlieren-like visualisation of flow on the symmetry plane and at the AIP from a DES simulation.

2.1.1 Performance of the intake

The intake allows the air coming from the atmosphere to reach the low pressure compressor, namely the fan in the case of a turbofan engine (Figure 2-2). Consequently, the distortion levels inside the flow significantly affect the overall performance of the engine, leading to a decrease in the surge margin of the system [15]. To avoid unstable operation of the engine a uniform flow at the inlet is recommended. Commonly at the exit of the intake, namely where the compressor stage is placed, a flow Mach number between 0.4 and 0.6 is required in order to maintain the desired performance [16].

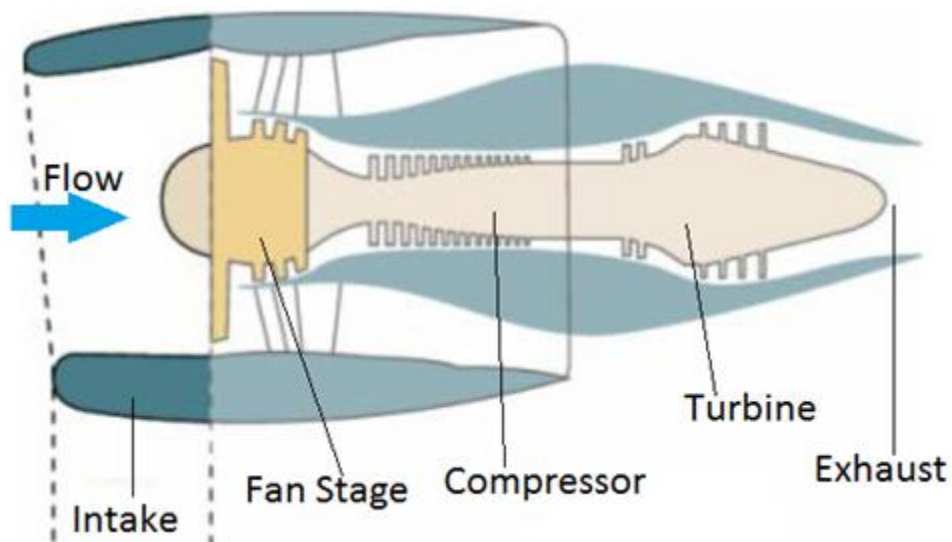


Figure 2-2 General arrangement of a turbofan engine with an intake for subsonic applications [17].

Accordingly, depending on the Mach number of the aircraft, the intake needs to accelerate or decelerate the flow in order to meet the requirements in mass flow demand [16].

In the study and description of the flow inside the S-duct, a more complex intake (Figure 2-3), paramount importance is given to the Aerodynamic Interface Plane (AIP) [11]. In particular the AIP is an arbitrarily defined section located at the interface between the intake and the engine face (Figure 2-4). Nevertheless, some general guidelines for the definition of this plane can be found in SAE ARP 1420 [18] which are summarized in this project in the following points:

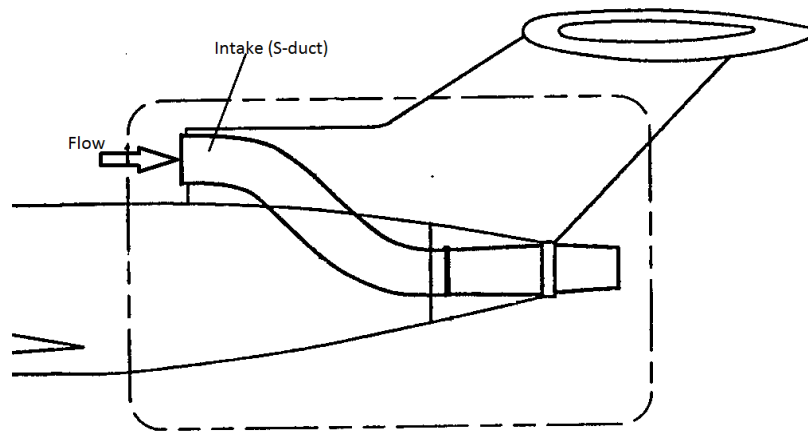


Figure 2-3 Convoluted intake in a rear engine configuration for commercial aircraft [17].

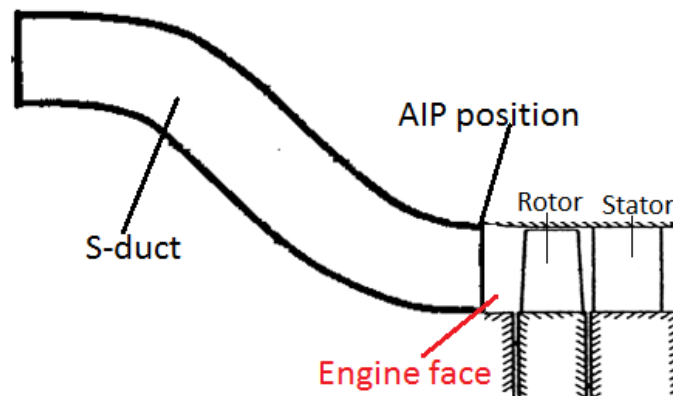


Figure 2-4 Simple schematic to show the interface between engine, intake and the AIP position.

1. The AIP should be positioned in a circular or annular section of the duct [18].
2. The AIP should be placed as close as possible to the engine face [18].
3. The mass flow passing through the AIP and the engine face has to be the same [18].
4. The position of the AIP has to capture the distortion caused by auxiliary air systems [18].
5. The position of sensors should not affect engine performance [18].

The importance of the AIP is related to the fact that engine performance is normally calculated at the AIP itself, using an averaged total pressure value. Looking in greater detail at the performance of an intake, we see that the efficiency associated with ram compression, which is dependent on the flight Mach number, is commonly quantified using a total pressure recovery coefficient (PR) [11]. It is defined as the ratio between the value of averaged total pressure at the AIP plane ($P_{0,AIP}$) and the free stream total pressure, usually taken as reference value ($P_{0,ref}$). For this reason we can write (eq. 2-1):

$$PR = \frac{P_{0,AIP}}{P_{0,ref}} \quad (2-1)$$

Taking into consideration the determination of the total pressure at the AIP surface, different methods can be used in order to estimate the averaged value. A first approach tries to consider the distorted nature of the flow by looking at entropy increase across the AIP [11].

However, to calculate total pressure at the AIP, a different definition (eq. 2-2) is usually adopted, namely the area-averaged total pressure [19]:

$$P_{0,AIP} = \int_A P_0 dA \quad (2-2)$$

where the value of A corresponds to the AIP surface. It is important to note that, in the event of high distortion values, more complicated methods are used since the models presented now are accurate enough only for uniform airflow at the AIP. On the other hand, it is preferable to consider the spatial total-pressure distortion at the AIP when a highly non uniform flow is detected. These methods will be presented in the following sections.

Distortion at the AIP can be defined as a temporal or spatial deviation of flow properties from a steady state [18]. SAE documents ARP 1419 [19] and 1420 [18] describe four different types of distortion related to an intake in terms of: static pressure, total pressure, total temperature and swirl [19]. As far as the S-duct is concerned, total pressure and swirl distortion are predominant, while

total temperature distortion can be observed only in the downstream region after the intake [19]. Usually, the presence of total temperature distortions at the AIP is mainly related to ingestion phenomena such as: steam ingestion, exhaust gas re-ingestion due to the presence of thrust reversers and armament firing gas ingestion [11]. Static pressure distortion, on the other hand, is related to ingestion phenomena when the aircraft is on the ground and can be avoided with appropriate handling [19]. Therefore, for the purposes of this work they will not be considered since they are not of direct interest, while total pressure and swirl distortion will be analysed and described in detail (Figure 2-5).

The definition of total pressure, in the context of the study of an S-duct at the AIP, can be seen in eq. (2-2) and will be further analysed in section 2.1.4. Now, it is important to present the concept of swirl (Figure 2-6) as described by SAE report ARP 1419 [19].

Swirl is a measurable parameter only if flow angularity is defined, where flow angularity is the deviation of the local velocity vector (U) and a vector normal to the AIP (U_x) [11]. In this way, a circumferential and a radial component of the velocity vector are generated and by applying simple trigonometry the mathematical definition of the swirl angle α can be found.

$$\alpha = \tan^{-1} \left(\frac{U_\theta}{U_x} \right) \quad (2-3)$$

Basically, the swirl angle α is defined at a point as the circumferential angle of flow from the axial direction [19], as determined in eq. (2-3) and depicted in Figure 2-6.

2.1.2 Previous investigations of S-ducts

As already mentioned, over recent years the importance of S-ducts has prompted extensive studies of the aerodynamics involved. One of the first studies can be found in the work of Wellborn et al. [21]. This experiment, in which oil was used to visualize the flow and measurements were taken with probes, represented a starting point for subsequent investigations made.

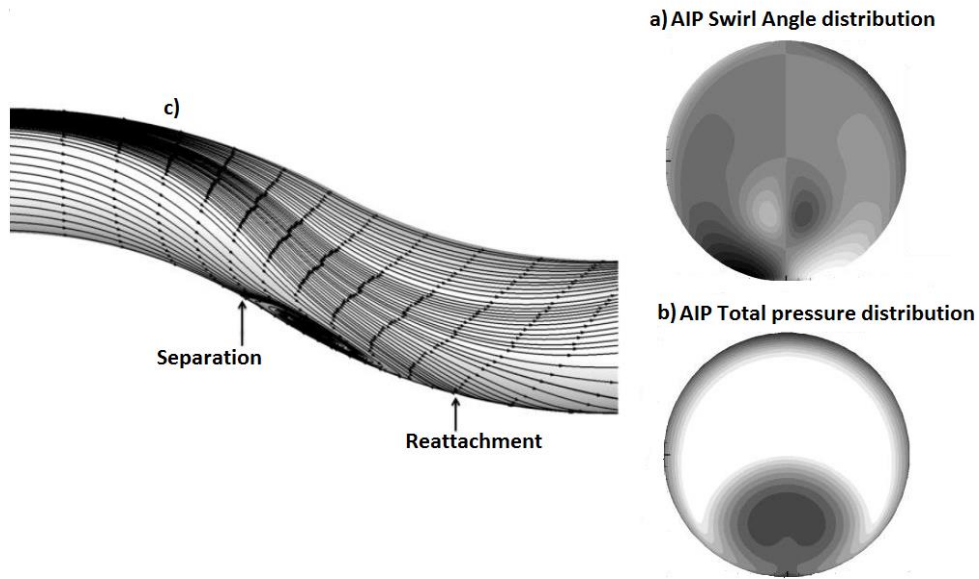


Figure 2-5 Example from RANS simulation of S-duct flow characteristics; a) Swirl angle distribution, b) total pressure (right) distribution at the AIP, c) wall streak-line [20].

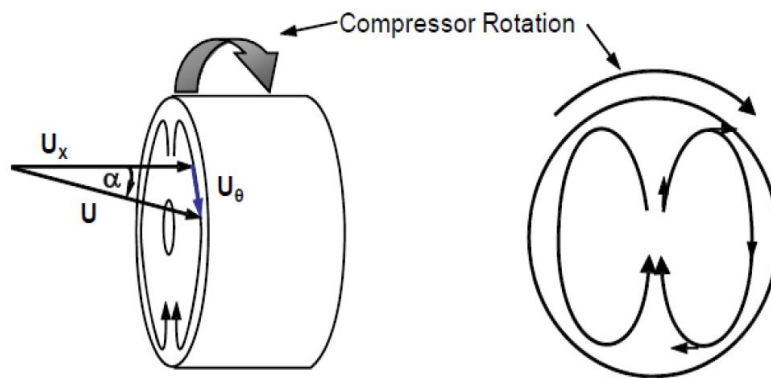


Figure 2-6 Swirl Angle definition [11].

It refers to an S-Duct with Area Ratio (AR) of 1.52, where area ratio represents the ratio between the outlet and the inlet area of the S-Duct. The duct centreline was defined using two circular arcs of an angle $\theta_{max}/2$ of 30° [21]. Consequently, an offset-to-length (H/L) of 0.27 characterizes the duct. All the cross sections perpendicular to the duct are circular [21]. The geometry is shown in Figure 2-7.

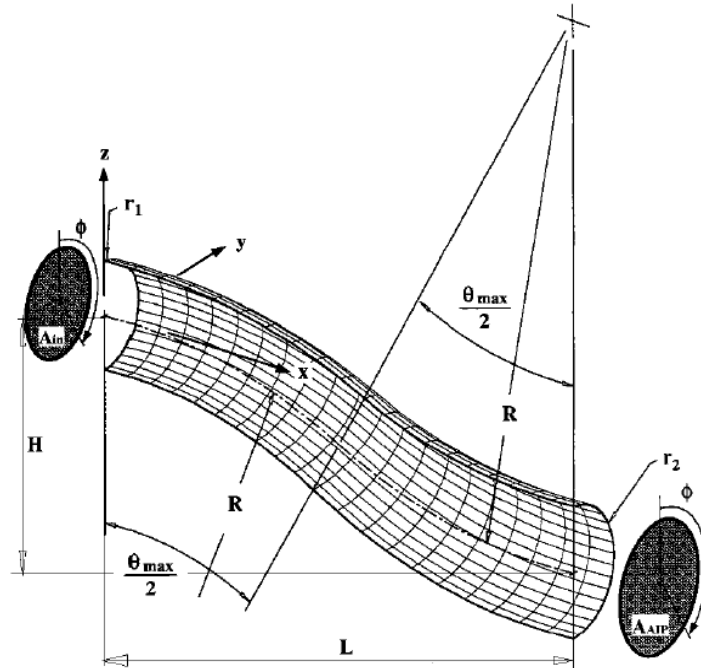


Figure 2-7 Geometry, parameters definition and plane position in the system studied by Wellborn et al. [21].

The importance of this experiment can be summarized as follows:

1. The flow inside the S-duct is symmetric in nature [21].
2. The separation of the flow appears along the lower wall [21].
3. In the S-duct a boundary layer cross flow is observed [21].

Moreover, due to the presence of pressure gradients created by the second bend, at the exit of the duct the flow was axial. These elements are at the basis of the later discussions about the description of the distorted flow in the duct. A representation of the experiment can be seen in Figure 2-8. In this picture thanks to the use of streak lines of fluorescent oil [21], both the overall flow pattern and the separated region can be seen. Figure 2-9 shows more clearly Wellborn's results at different sections of the duct in terms of total pressure.

In particular, it can be seen that at planes C, D and AIP the convection of boundary layer flow far from the surface into the core flow is quite pronounced [21]. As a consequence, in particular at the AIP a region with low total pressure values was found.

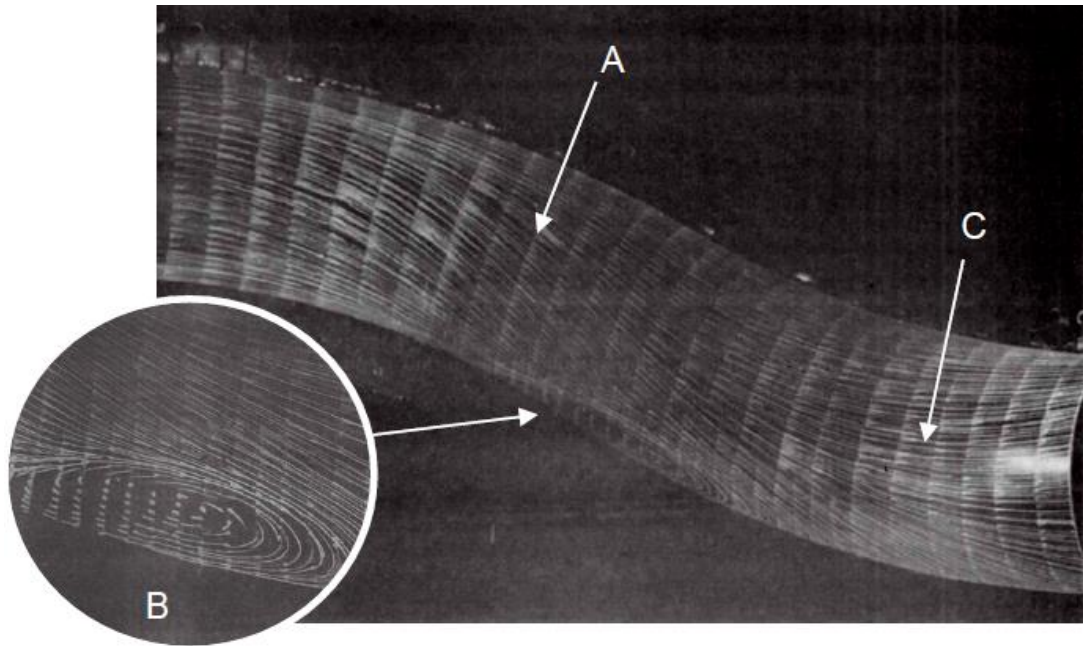


Figure 2-8 Flow field of Wellborn's S-duct [21]. A) crossflows due to action of pressure gradients, B) Recirculation, C) axial flow at the exit

Figure 2-8 and Figure 2-9 can be regarded as an application and practical description of the three previous statements about the symmetric nature of the flow, the position of the separation and the presence of a boundary layer cross flow. Improvements in computer performance led to a combination of experiments with computational fluid dynamics (CFD), used as a prediction and validation tool. As A. Delot et al. [22] and P. A. Watson et al. [6] explained, agreement between experiments and CFD simulations is highly dependent on the turbulence model chosen [22]. Moreover, Reynolds averaged Navier-Stokes (RANS) methods, though quite cheap in terms of computational effort, are not able to describe the real unsteadiness in the flow field but only the time averaged flow properties. The only way to capture the full unsteadiness present is to use a time variant method such as Large Eddy Simulation (LES) and Detached Eddy Simulation (DES). These methods will be described in the following sections.

One of the first studies of an S-Duct where experimental data were used in combination with CFD simulation to describe the flow, is presented in the work of Delot et al. reported in [14].

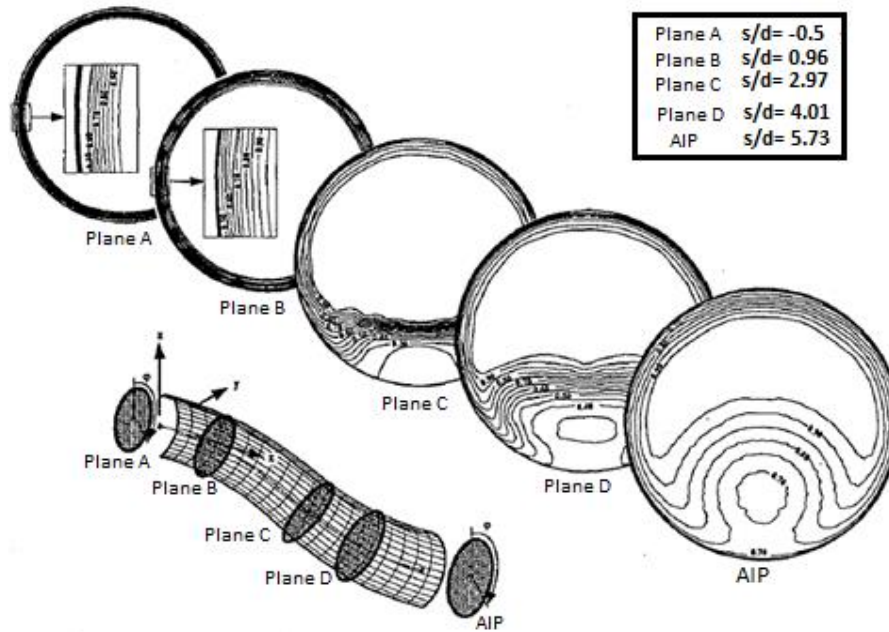


Figure 2-9 Total pressure distribution at different planes in the Wellborn experiment [21].

In this study both RANS and DES methods were applied to characterize the unsteadiness at the AIP of a shaped duct used by an UAV. As shown in Figure 2-10, by means only of a time-dependent simulation the goal of characterizing the unsteadiness of the flow field is achieved. Close agreement between CFD and experimental data can be observed. However, the use of both RANS and DES meant that the topology of the flow at the AIP with two vortices at the bottom and a separated region in the first part of the duct could be described. A CFD simulation based on the Wellborn diffusing S-duct (Figure 2-7) is presented by P. A. Watson et al. [6], who not only further analysed the flow field inside an S-duct but also investigated the relationship between experimental data and CFD analysis better [6]. In particular, they showed the inability of RANS methods to properly describe the flow field. Linear eddy viscosity models miss important features of the flow [6] compared for example to Zonal Large Eddy Simulation (ZLES), where LES is applied to the core and RANS to the boundary layer [6]. This second method seems to be able to capture the salient aspects of the unsteadiness in the flow and, in the regions where RANS performed well, ZLES performed perfectly [6] (Figure 2-11). Despite pure LES's

better reliability and greater ability to describe separated flows at relatively high Reynolds numbers, it still cannot be routinely applied during the design process due to the high computing costs.

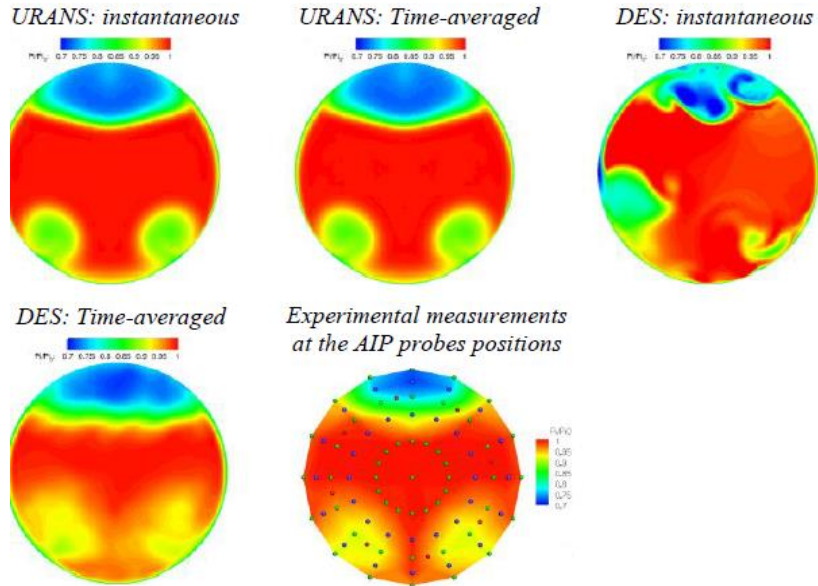


Figure 2-10 Total pressure distribution at the AIP using both transient and steady methods, compared with experimental data [14].

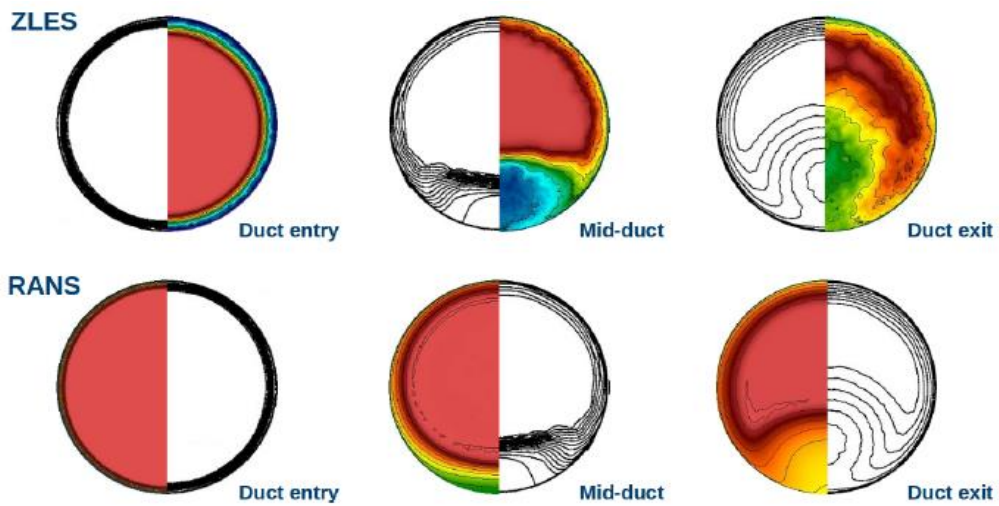


Figure 2-11 Comparison between RANS and ZLES with the experimental data of Wellborn et al. [6].

2.1.3 Flow Distortion

The preceding section introduced different concepts related to flow distortion. This section presents a more detailed description of the phenomena involved in which the differences between types of distortion will be highlighted. As already stated, swirl and total pressure distortions are the two most relevant types in the case of an S-duct. In particular, total pressure distortion is commonly produced by flow separation and wakes. In shaped ducts, it is generated by the separation that occurs between first and second bend [15].

In a convoluted intake, such as Figure 2-12 and Figure 2-13, it is possible to observe three different regions of low pressure at the AIP surface. Two of them are located at the bottom of the duct and they derive from the first bend, whereas the third region of low pressure is located in the upper part of the section and is caused by the second bend of the duct [11]. The reason is that the second bend is closer to the AIP section and consequently vortices originating after the second change diffuse less than those from the first bend, leading to the flows shown. The system of reference used in Figure 2-12 will be adopted throughout this project: Z represents the stream-wise direction, Y the vertical direction and X the lateral direction. Therefore, velocity, for example, can be divided into three components called respectively: stream-wise velocity w , vertical velocity v and lateral velocity u .

At the same time, total pressure distortion is also accompanied by swirl distortion, which means that in regions with low values of total pressure there will be areas of recirculation and vortices. This can be observed in Figure 2-14, where velocity vectors are superimposed on total pressure distribution at the AIP. The phenomenon shown in Figure 2-14, namely the formation of a twin swirl at the AIP section, is common in S-ducts and a more detailed description is needed.

Considering an ideal fluid that moves across a bended duct and looking at the movement in the axial direction, the centrifugal force due to the curvature is controlled by the increase in static pressure by increasing the radius as well as the decrease in velocity approaching the wall [11]. On the other hand, the value

of static pressure tends to decrease moving perpendicularly from the outer to the inner wall, with a resulting increase in velocity [11].

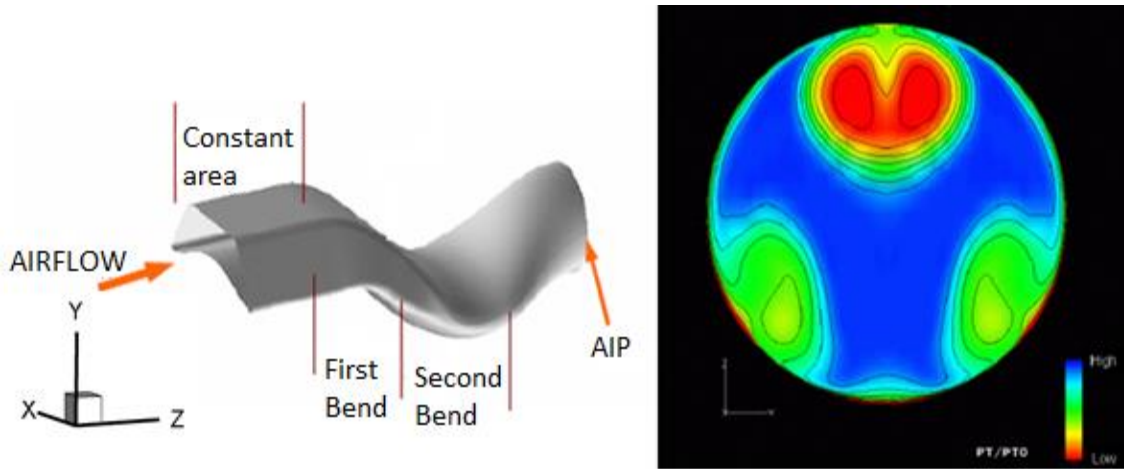


Figure 2-12 Shape of double bend S-duct and total pressure distribution at the AIP from a CFD calculation [11].

As a consequence, it starts to move around the wall towards the low static pressure region in the inner part of the bend. The combination of these two phenomena, namely the deflection of the high energy core flow and the movement of the low momentum flow towards the inside, lead to the formation of two areas of recirculation [11]. This behaviour is presented schematically in Figure 2-15.

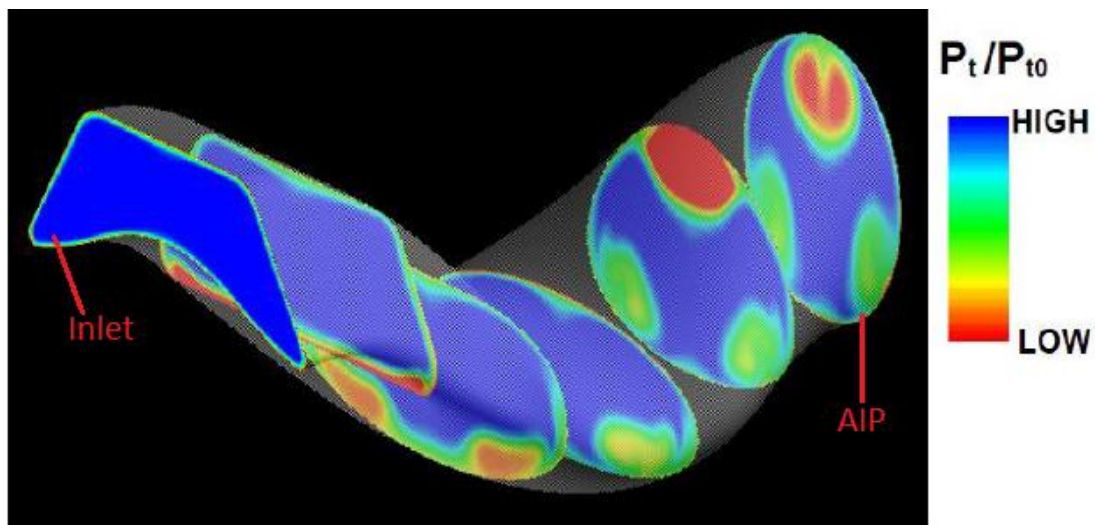


Figure 2-13 Flow evolution inside a double bend S-duct [11].

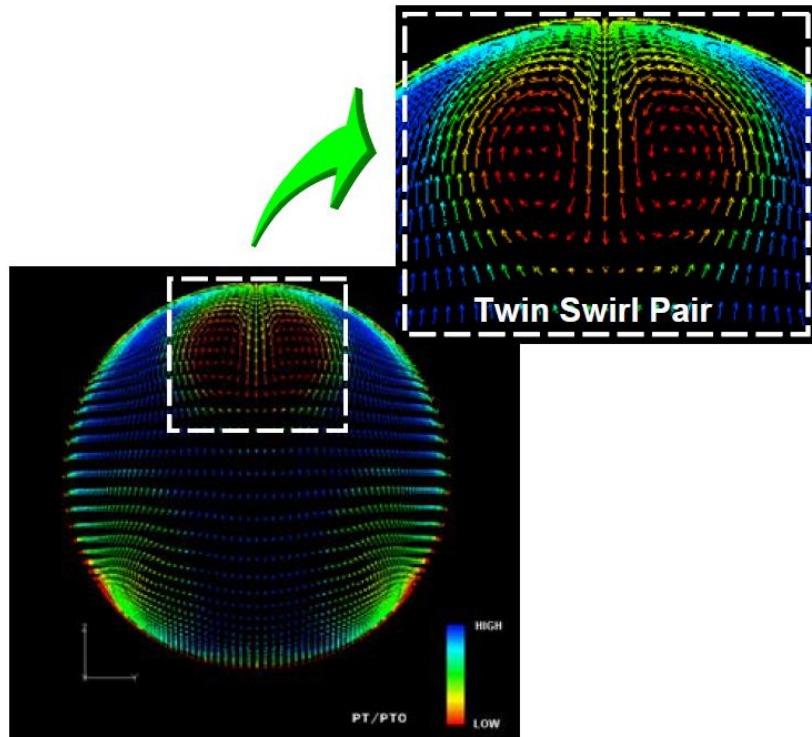


Figure 2-14 Twin swirl pair at the AIP of an S-Duct [11].

In the description applied so far, the two vortices were believed to have the same magnitude and an opposing sense of rotation. This condition is called “twin swirl”. However, there are often asymmetric boundary layers present along the wall which produce two swirls with differences in magnitude. This results in what is called an “offset swirl pair” or more commonly a “paired swirl” where the flow presents a unique rotation around one axis, generating a single vortex. Basically, the whole flow field rotates in the same direction. This type of flow is not uncommon in S-ducts and is produced by the combination of two important phenomena. The first one is the presence of an asymmetric total pressure gradient perpendicular to the turning plane and secondly the presence of a static pressure gradient due to the bend in the duct (Figure 2-16) [11].

To conclude this section we can categorize thus:

1. Bulk Swirl [11].
2. Paired Swirl, with the particular case of twin swirl when the two region of recirculation have the same magnitude [11].
3. Cross-flow Swirl [11].

4. Tightly-wound vortex [11].

The tightly-wound vortex and cross-flow swirl are not of interest here because they appear in short straight inlet ducts in lift fan configurations or during ground operations [11].

2.1.4 Action of distortion on the engine

The aim of this section is to analyse how the distortion levels in the flow affect the engine and in particular its operability. Both total pressure and swirl distortion and their combination will be considered. It will also include a brief analysis of the principal descriptors used to assess and quantify distortion levels in the duct.

2.1.4.1 Effect produced by total pressure distortion on engine operation

The largest effect of the total pressure distortions can be observed on the fan or low pressure compressor facing the S-duct, close to the AIP position [11].

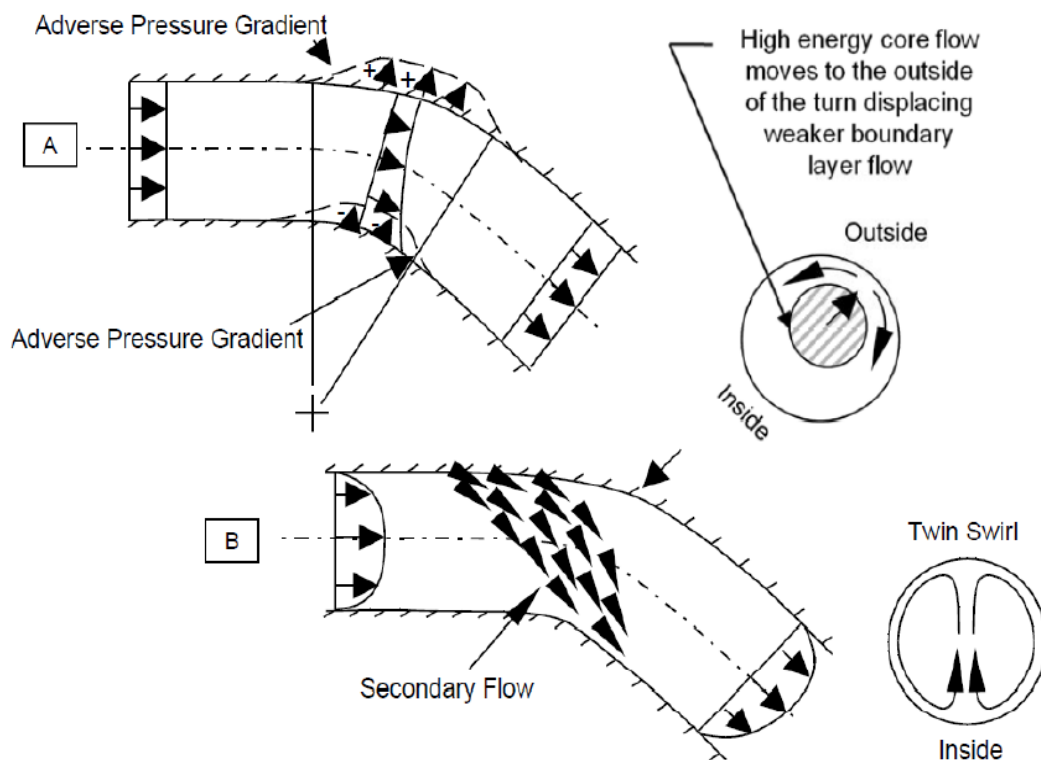


Figure 2-15 Twin swirl formation in a S-duct [11].

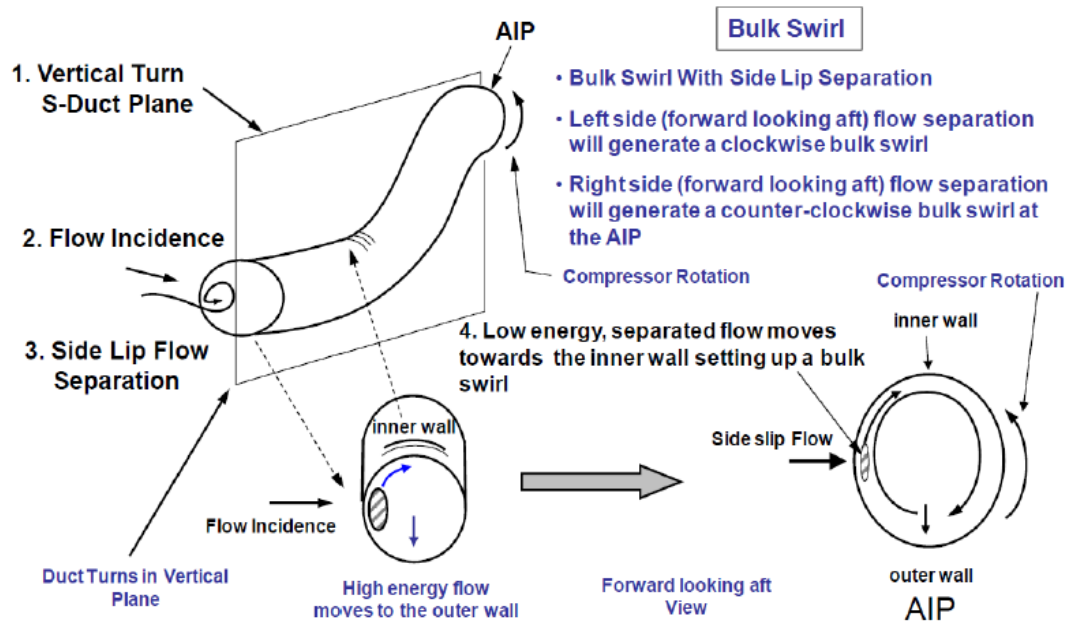


Figure 2-16 Bulk Swirl formation in an S-duct [11].

As already mentioned, a combination of radial and circumferential distortion have two main effects on the engine. The first is a decrease in the mass flow capacity of the engine which reduces efficiency at a given rotational speed [19]. The second is that the surge margin of the engine tends to decrease if the distortion level increases (Figure 2-17) [19]. In order to understand the process involved better, we need to divide the engine into two different parts. The first is the region in which distortion is affecting the system and consequently the mass flow is lower. In this case, looking at the compressor map, the operating point moves upwards, leading to an increase in the pressure ratio [19]. The second region instead, applying the continuity principle, have an higher value of mass flow, namely the pressure ratio in this area decreases [19].

As a consequence, the compressor responds to this flow behaviour, by reducing pressure upstream of the distorted region. This produces non-uniform static pressure distribution, leading to circumferential swirl distortion. In this way, surging events are more probable due to changes in incidence angle of the flow on the blades and changes in loading [19]. Even if a circumferential distortion always has a negative effect on the systems, radial distortion can improve the operation of the fan or compressor. This is particularly true in the

case of a tip-radial profile with a small amount of radial distortion [19]. In this situation we observe an increase in the surge margin in the compressor map, compared to the case of an AIP without distortion [19].

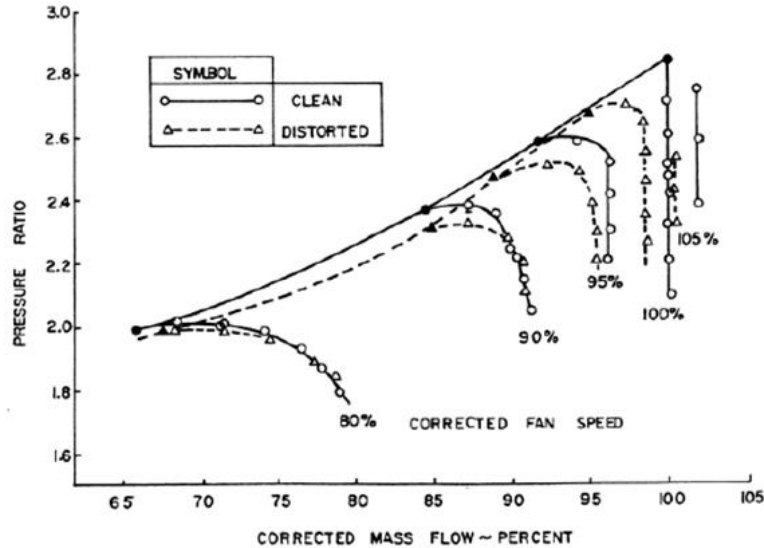


Figure 2-17 Three staged fan map change due to distortion [19].

Although the major effects of distorted flow can be found in the area close to the AIP, i.e. the first stages of an LPC or a fan, they clearly do not suddenly disappear because it also has an impact downstream. The downstream effects will, however, be of a different type, namely what was referred to in section 2.1 as total temperature distortion. The nature of this distortion is associated with a decrease in the work done by the compressor, which in turn modifies the total temperature distribution in the system [11]. Moreover, there is a big difference between total pressure and total temperature distortion. Even if the total pressure distortion can be considered to have dissipated at the exit of the High Pressure Compressor (HPC), as far as total temperature distortion is concerned, it can also propagate to the hot section of the engine, thereby decreasing not only the overall performance of the system but also its life [16]. Figure 2-18, shows where the different types of distortion can be found inside a turbofan engine and how they propagate and affect the system.

Another negative impact of distortion on the engine involves the control system. Basically, it uses local values of total pressure and total temperature, or local

flow properties, in order to control the engine during operation. If flow is distorted, the measurements taken will mean that the engine is wrongly controlled during operation, with a resulting decrease in the performance of the system [11].

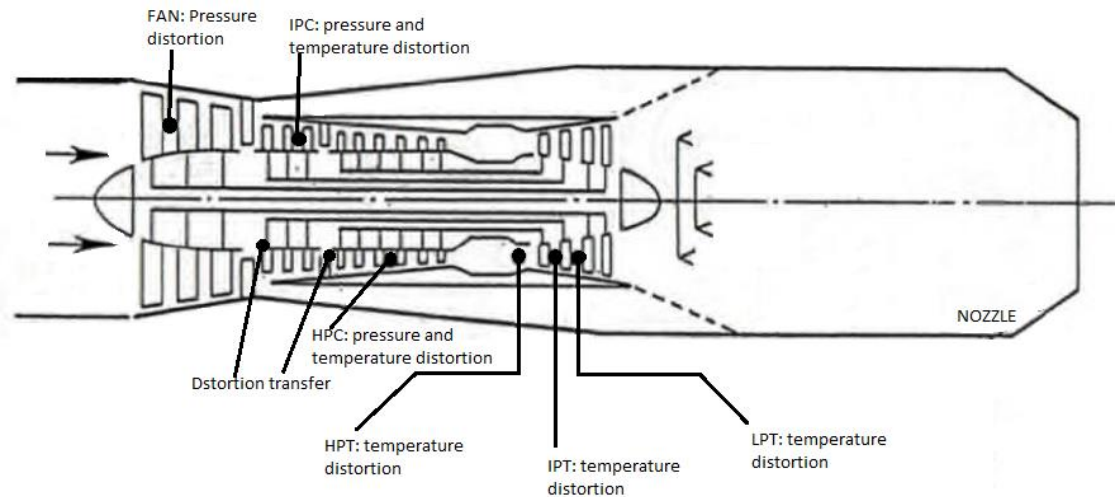


Figure 2-18 Position and types of distortion in a turbofan engine [16].

2.1.4.2 Effect produced by swirl distortion on engine operation

A recent detailed description of the action of swirl distortion highlighted the impact of swirl downstream of the AIP on the fan or the first stages of the compressor [11]. Due to the presence of such distortion the main effect on the engine is a change in the incidence of the flow approaching the rotor stage, leading to the aerodynamically inefficient operation of the fan/compressor. A first solution to the problem was to introduce IGVs after the AIP. This was mainly used for military purposes and the limited application derived from the strict engine requirements [11]. As a matter of fact, if we look at the overall system, the need for a certain amount of available space between the AIP and the engine face together with the increase in weight, in some cases offset the benefits [18].

There follows an analysis of bulk swirls for constant rotational speed, which can be classified into two different types [11]. The first is called co-rotating bulk swirl and appears if the inlet swirl is rotating in the same sense as the rotor blades [11]. Similarly, counter-rotating bulk swirl occurs if the rotation of the swirl and

the rotor are in opposition [11]. Obviously, in a real situation it is also possible to observe different types of swirl and a variable rotational speed, but in order to properly understand the problem, the previous assumptions are initially considered. Looking at a co-rotating bulk swirl with a constant axial velocity, an increase in the stability margin can be observed due to a decrease in the value of the incidence angle and, namely, of the loading on the rotor blades [11]. As a consequence, by looking at a compressor map, this can be translated into a change in the non-dimensional rotational speed to lower values of pressure ratio and non-dimensional mass flow (also referred to as flow capacity) [23]. The second type of bulk swirl leads to a decrease in the stability margin as a consequence of the increase in incidence and loading. Similarly, this moves a speed line to a higher value of both pressure ratio and flow capacity [23].

In the case of a twin swirl, both regions of counter-rotating and co-rotating bulk swirl are acting on the rotor blades. The net effect, namely the change in stability of the compressor, depends on the intensity and proportion of the two regions [11].

It is important to note that Figure 2-19 represents the worst case scenario in which a control system is not included. In reality the action of the swirl will be less important since the control system tends to adjust the axial velocity controlling the position of the blades [11].

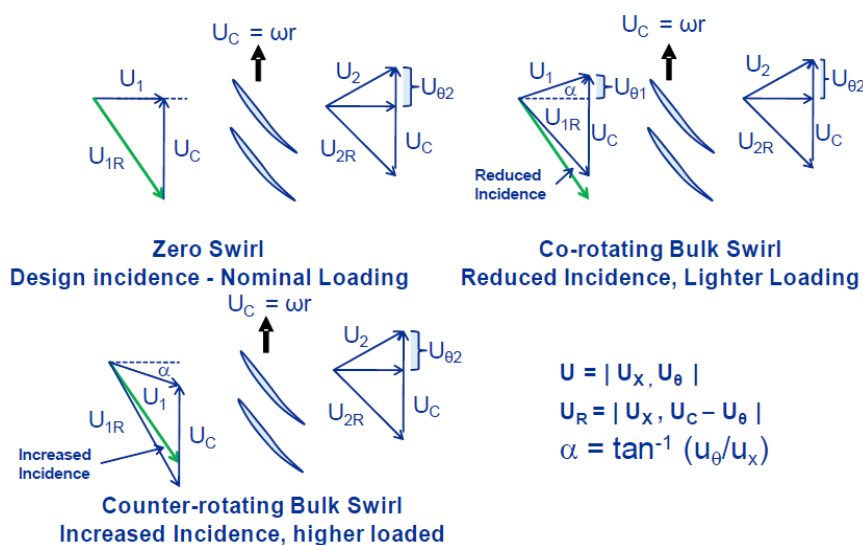


Figure 2-19 Action of the bulk swirl on the rotor blades [11].

2.1.4.3 Coupling of total pressure and swirl distortion: correlation approach

The combination of both total pressure and swirl distortion, beside the increase in complexity in order to model the overall phenomena, lead to a much worse impact on stability compared to what has been described in previous sections [11].

In particular, the Figure 2-20 shows the interaction between the two flow phenomena. Basically, the fundamental conclusion that can be drawn from the diagram is that the presence of a swirl can lead to stability problems in the compressor when, for instance, total pressure distortion on its own would not account for it since it lies below the limit [11].

A first reduction in stability margin can be observed due to the presence of a co-rotating swirl with total pressure distortion. However, the worst case scenario happens when a counter-rotating bulk swirl appears together with total pressure distortion, which in turns leads to a huge decrease in the margin [11].

An analytical study cannot be conducted to combine the effect of different types of distortion and for this reason SAE S-16 started to use correlations based on experimental data obtained from the numerous investigations conducted. In the SAE literature it is possible to find different correlations and different values for the coefficients [18]-[19].

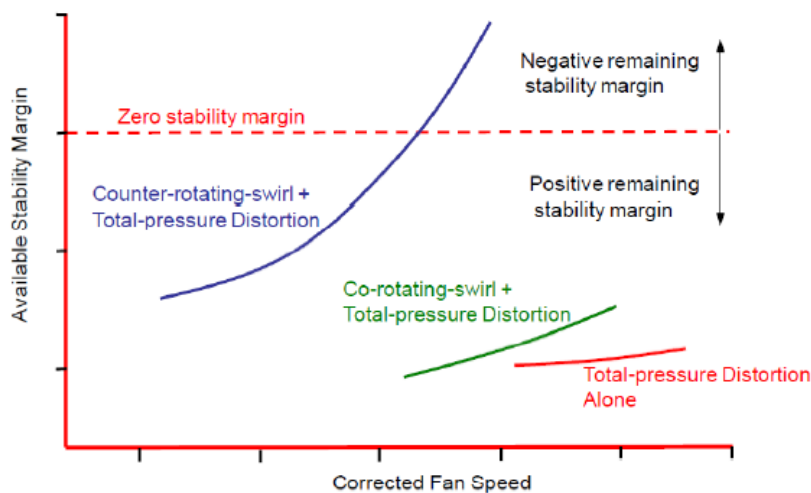


Figure 2-20 Coupling of total pressure and swirl [11].

The loss in surge margin ΔPRS , previously also called stability margin, is defined by eq. (2-4) as [11]:

$$\Delta PRS = \left(\frac{PR1 - PRDS}{PR1} \right) \times 100 \quad (2-4)$$

where in particular $PR1$ represents the undistorted value of surge pressure ratio while $PRDS$ is the distorted value. In a more representative way, these parameters are described in Figure 2-21.

First of all, the definition given in eq. (2-4) can be used to determine the effect due only to the action of a swirl distortion (eq. (2-5)):

$$SM_{available} = \left(\frac{PR1 - PR0}{PR0} \right) \quad (2-5)$$

where SM is the stability margin and $PR0$ is the operating pressure ratio [11].

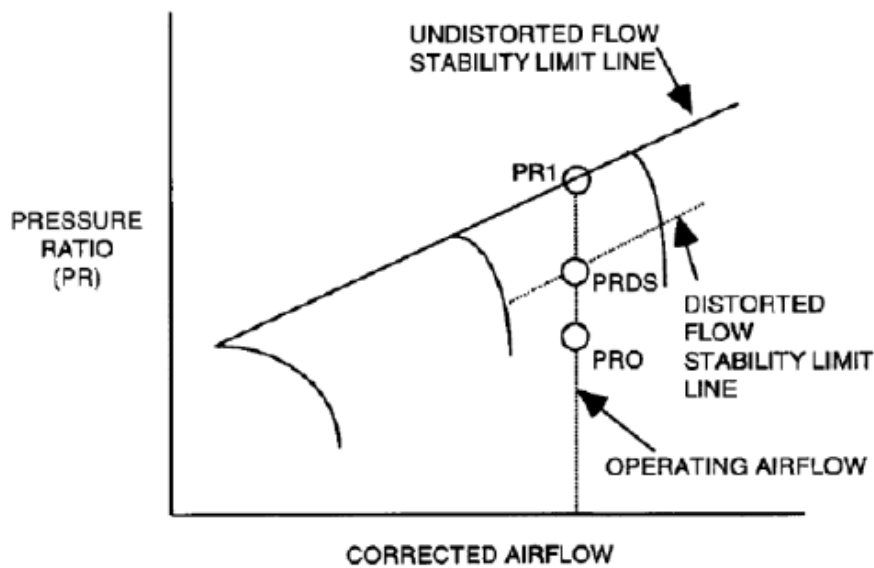


Figure 2-21 Definition of the parameters by SAE committee [11].

The loss in stability margin due to the presence of a swirl is called ΔSM and, similarly to what happened for the pressure distortion, it is normalized by $PR0$ at a constant airflow [19]; this is expressed by eq. (2-6):

$$\Delta SM = \left(\frac{PR1 - PRDS}{PR0} \right) \times 100 = \Delta PRS \times \frac{PR1}{PR0} \quad (2-6)$$

Since the combined effect can be more intense than the superimposition of the independent distortions, as reported by SAE in ARP 1419 [19], the correlation that describes the loss in surge margin in this case can be written as the sum of three contributes as shown by eq. (2-7) [18]. The first (ΔPRS_s) is the loss in surge margin due to the total pressure distortion, the second (ΔPRS_p) due to swirl distortion and finally the last (ΔPRS_{ps}) is the combined effect on the surge margin of total pressure and swirl [19].

$$\Delta PRS = \Delta PRS_s + \Delta PRS_p + B \times \Delta PRS_{ps} \quad (2-7)$$

It is important to note that correlation coefficients can be found in SAE literature ([18]-[19]) for the first two terms, while for the last one no correlation has been developed yet.

2.1.5 Distortion Descriptors

The most important descriptors of the distortion will be presented in this section in order to understand which parameters are used and why.

2.1.5.1 Total pressure descriptors

Following the definition given by SAE, the most important parameters to consider are DC60, CDI and RDI if we want to have a good description of total pressure distortion inside the flow. The following definitions come mainly from the ARP 1419 [19] and 1420 [18] reports by the SAE.

2.1.5.1.1 DC60

First used during the development of the RB199 engine and then also with the more recent EJ200 engine [11], in more general terms it is called DC θ . The symbol θ represents the dimensions of the spoiled section and the mathematical definition shown in eq. (2-7) is [3]:

$$DC\theta = \left(\frac{\overline{p_{t,AIP}} - \overline{p_{t,\theta}}}{q^2} \right) \quad (2-8)$$

In the previous equation, $\overline{p_{t,AIP}}$ refers to the mean value of total pressure in the AIP section, $\overline{p_{t,\theta}}$ is the lowest value of total pressure in all the section of extent θ

and finally q^2 is the mean dynamic pressure at the AIP [3]. As a matter of fact, the compressor face is subdivided into different rings or sectors where averaged values of flow variables are taken [15]. In particular, as has already been mentioned, after a huge number of experiments, an increase in the spoiled region negatively affected the surge margin [16]. As the angle of the spoiled sector (θ) increases, the surge margin decreases, but when a value of $\theta = 60^\circ$ is reached, then no further decrease in surge margin can be observed. For this reason the specific DC60 parameter was introduced and accounted for the minimum mean area total pressure in any 60 sector of the compressor (Figure 2-22) [16].

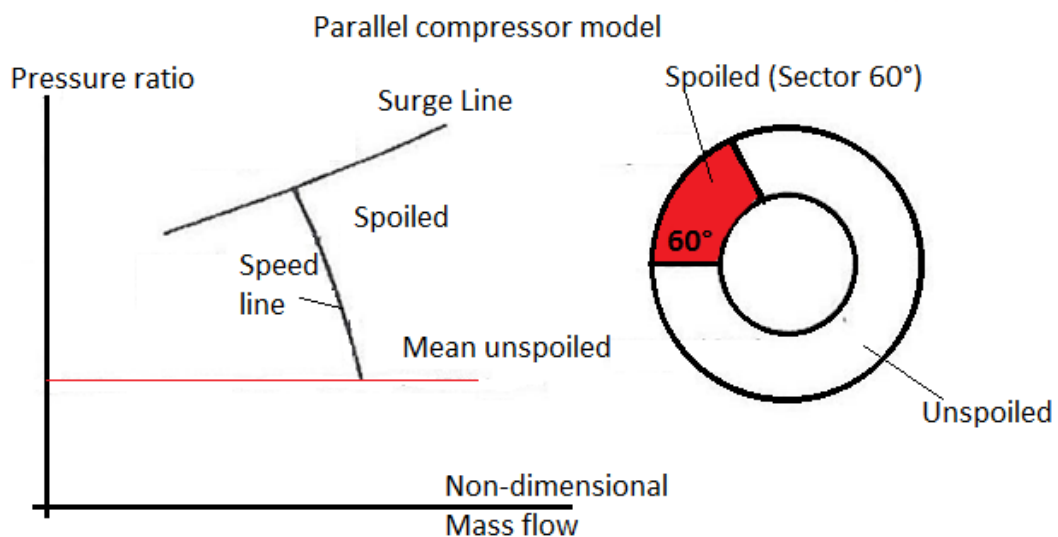


Figure 2-22 example of θ section of the spoiled region at the compressor face [16].

2.1.5.1.2 CDI and RDI

Circumferential and radial distortion indices (CDI and RDI) are based on the division of the AIP surface into a certain number of sections in both a radial and circumferential direction as shown in Figure 2-23 [15]. Also a possible arrangement of pressure sensors can be seen in Figure 2-23. In particular, CDI assesses the uniformity of the circumferential total pressure distribution at a specific radial position [2]. Non uniformities in the radial direction are described by RDI [2].

To determine the overall CDI, a local parameter CDI_i is defined as follows in eq. (2-9) [2]:

$$CDI_i = \left(\frac{\overline{p_{t,i}} - p_{tmin,i}}{\overline{p_{t,AIP}}} \right) F_{\theta i} \quad (2-9)$$

where $F_{\theta i}$ is an empirical weighting factor dependent on the circumferential dimension of the sector with the lowest value of total pressure in the ring, $\overline{p_{t,i}}$ is the mean total pressure on a ring and $p_{tmin,i}$ is the minimum value of total pressure on the ring [2].

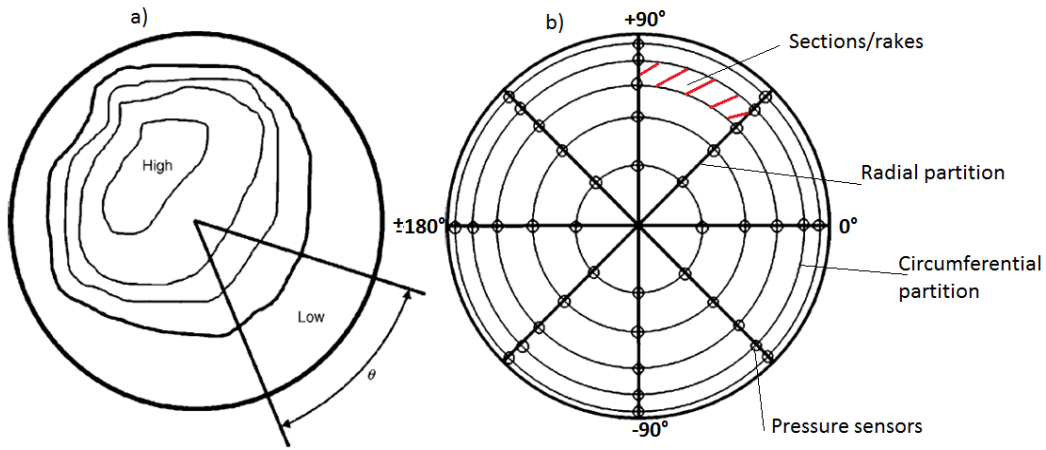


Figure 2-23 a) critical sector angle; b) division of the AIP surface in rakes [15].

Consequently, the circumferential distortion index is defined as the largest mean value of CDI_i between two consecutive rings and is expressed in eq. (2-10):

$$CDI = \max[0.5 \times (CDI_i + CDI_{i+1})] \quad (2-10)$$

The radial distortion index (RDI) has a very similar definition to CDI , based on the following local parameter RDI_i (eq. (2-11)) [2]:

$$RDI_i = \left(\frac{\overline{p_{t,AIP}} - \overline{p_{t,i}}}{\overline{p_{t,AIP}}} \right) \quad (2-11)$$

In particular RDI is the maximum value of eq. (2-12) calculated for both inner and outer rings. In particular the subscript i represents the inner or the outer ring. Therefore, the equation for RDI can be written as follows in eq. 2-12:

$$RDI = \max[RDI_{in}, RDI_{out}] \quad (2-12)$$

It is important to underline in Figure 2-23 how the position of a point is described in a perpendicular section in the X-Y plane of the S-duct. A polar coordinate system is adopted and angles (i.e. $\pm 90^\circ$) are used to identify a specific position. This is important in order to understand the data in section 4.3.1.

2.1.5.1.3 Further definitions by SAE

In order to relate the various descriptors of the distortion to the surge margin, the SAE introduced some other relations that will be briefly presented in this paragraph. In ARP 1419 [19], we find a detailed description of the following parameters for both one and multiple revolutions. However, due to the high complexity of the formulas and for the purposes of this study, only one-per-revolution distortion definitions will be analysed.

1. *Extent*: defined (eq. (2-13)) as the extension in degrees where the value of pressure is lower than PAV_i [19], where PAV_i is the ring average pressure value.

$$\theta_i^- = \theta_{2i} - \theta_{1i} \quad (2-13)$$

2. *Circumferential distortion intensity*: refers to the magnitude of pressure lack inside a ring [19] and it is presented in eq. (2-14).

$$\left(\frac{\Delta PC}{P}\right)_i = \frac{PAV_i - PAVLOW_i}{PAV_i} \quad (2-14)$$

where in particular, calling $p_t(\theta)_i$ the total pressure in the ring it is possible to write (eq. (2-15)):

$$PAV_i = \int_0^{360} p_t(\theta)_i d\theta \quad (2-15)$$

and defining $PAVLOW_i$ as the averaged total pressure in the spoiled section (eq. (2-16)):

$$PAVLOW_i = \int_{\theta_{1i}}^{\theta_{2i}} p_t(\theta)_i d\theta \quad (2-16)$$

3. *Radial distortion intensity*: refers to the average total pressure in the AIP ($PFAV$) to PAV_i as follow (eq. (2-17)) [19]:

$$\left(\frac{\Delta PR}{P}\right)_i = \frac{PFAV - PAV_i}{PFAV} \quad (2-17)$$

2.1.5.2 Swirl descriptors

In this section the most common swirl descriptors based on the study conducted and reported mainly by SAE committee in AIR 5686 [11], will be described.

2.1.5.2.1 SC60

One of the first descriptors used to quantify distortion levels is called SC60 and defined in eq. (2-18). It is the ratio between the highest value of velocity that can be found in a sector of 60° ($U_{\theta 60}$) and the mean axial velocity at the AIP surface ($U_{z,AIP}$) [2]-[24].

$$SC60 = \frac{U_{\theta 60}}{U_{z,AIP}} \quad (2-18)$$

2.1.5.2.2 Swirl distortion descriptors defined by the SAE S-16 committee

In order to correlate the operability of the compressor and swirl distortion, four different types of major descriptors are analysed. In particular swirl descriptors are similar to the circumferential pressure distortion descriptors presented in the previous section and fully described in ARP 1419 [19] -1420 [18]. In this case the descriptors are defined using the values of swirl angle coming from experiments or simulations relative to engine rotation [11]. Furthermore, the data used to define the four descriptors that will be presented in this section are associated with co-rotating and counter-rotating swirls. It is important to note that in the following analysis, one per revolution equations will be presented [11].

Figure 2-24 shows a common diagram of a paired swirl at a specific ring i in a complete single revolution at the AIP surface. θ_i^+ and θ_i^- represents the

previously defined extent of the positive (co-rotating) and negative (counter-rotating) swirl region.

The swirl descriptors are: Sector Swirl (SS), Swirl Intensity (SI), Swirl Directivity (SD) and Swirl Pairs (SP).

- *Sector Swirl (SS)* is defined at a specific radial sector and it gives the value of the average positive swirl content, namely the co-rotating swirl SS_i^+ (eq. (2-19)) and the average of the counter-rotating swirl SS_i^- (eq. (2-20)) of the distortion [11]. From a mathematical perspective it is defined as the integrated swirl angle over the extent θ_i^\pm . This means that, in order to determine the integral, the extents at a i-ring has to be known [11].

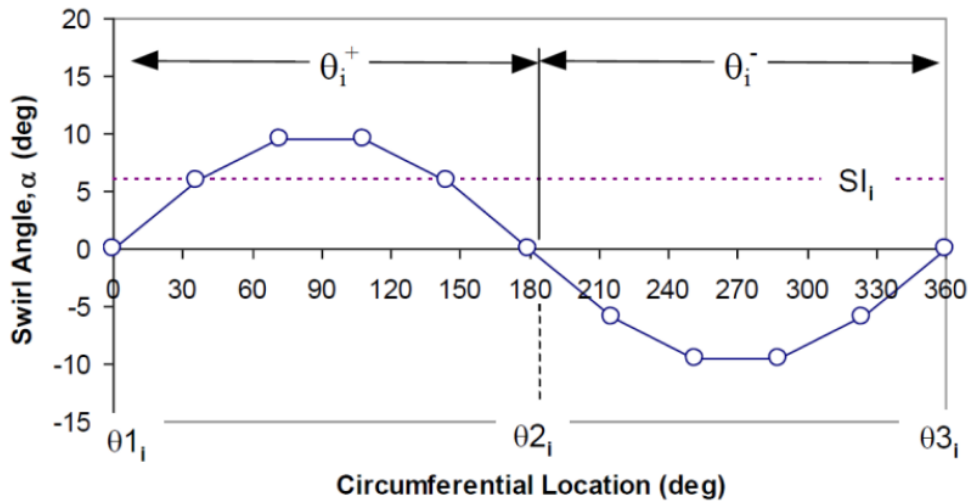


Figure 2-24 Swirl angle for one-per-revolution symmetric paired swirl [11].

$$SS_i^+ = \frac{1}{\theta_i^+} \int_{\theta_i^+} \alpha(\theta)_i d\theta \quad (2-19)$$

$$SS_i^- = \frac{1}{\theta_i^-} \int_{\theta_i^-} \alpha(\theta)_i d\theta \quad (2-20)$$

where $\alpha(\theta)_i$ is the swirl angle of the specific ring, dependent on the circumferential position.

- *Swirl Intensity (SI)* corresponds to the averaged circumferential swirl angle for each of the rings at the AIP. The value is expressed in degrees

in order to be consistent with the units of the swirl angle α [11]. Mathematically it is defined as follows in eq. (2-21):

$$SI_i = \frac{SS_i^+ \theta_i^+ + |SS_i^-| \theta_i^-}{360} \quad (2-21)$$

- *Swirl Directivity (SD)* shows the direction of rotation of the swirl distortion compared to the sense of rotation of the compressor, and is expressed for each ring sector and described by eq. (2-22).

$$SD_i = \frac{SS_i^+ \theta_i^+ + SS_i^- \theta_i^-}{SS_i^+ \theta_i^+ + |SS_i^-| \theta_i^-} \quad (2-22)$$

The range of SD_i is [-1;+1]; for a co-rotating bulk swirl a value of -1 is observed while for a pure counter-rotating bulk swirl the value is +1 [11]. Figure 2-25 shows the change in rotation direction described by SD parameter.

- *Swirl Pairs (SP)* is a value that indicates the number of alternating swirl pairs at a specific ring (eq. (2-23)).

$$SP_i = \frac{SS_i^+ \theta_i^+ + |SS_i^-| \theta_i^-}{2 \max(SS_i^+ \theta_i^+, |SS_i^-| \theta_i^-)} \quad (2-23)$$

Swirl Pair has a value of 1 if a twin swirl is present in the flow, while the value is 0.5 for both a co-rotating and counter-rotating swirl [11].

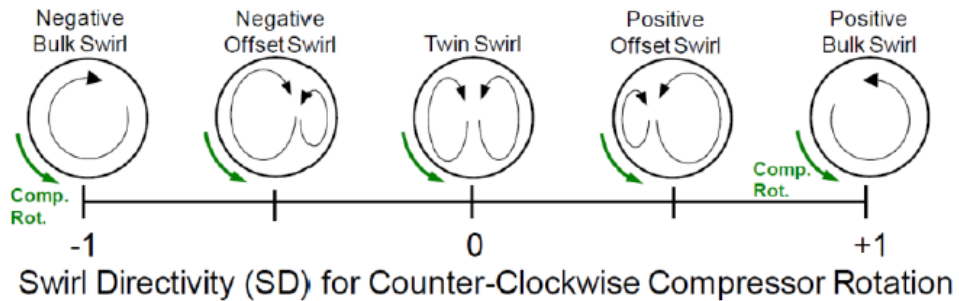


Figure 2-25 Swirl directivity in one revolution for different swirl patterns [11].

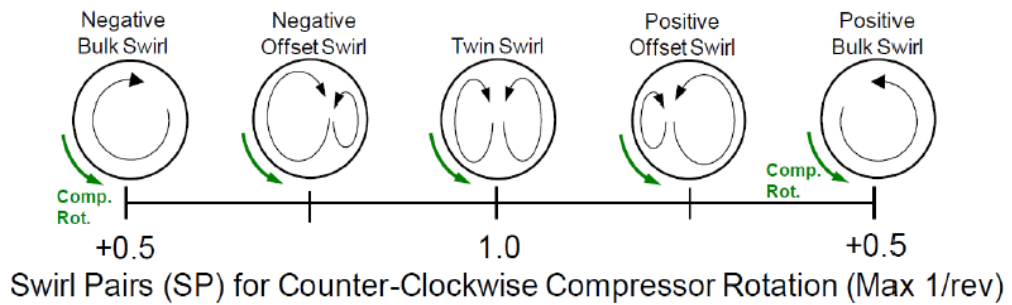


Figure 2-26 Swirl pairs in one revolution for different swirl patterns [11].

2.1.6 Impact of the engine on flow unsteadiness

Over the years a huge number of experiments have been done in order to determine how the presence of the engine downstream may affect the flow inside a S-shaped intake.

In the preceding sections the impact of the flow on the performance of the engine was presented, without looking at the change in flow characteristics due to the presence of an obstacle downstream. This is of paramount importance for this work since the main objective is to determine the flow field by means of a CFD simulation with the presence of a static fan simulator at the AIP position and compare the results obtained with a pure S-duct, without any system at the exit.

The main conclusion drawn from the work of Hodder [25] is that the effect of the engine at the exit of the intake is to decrease the level of flow distortion due to a redistribution of the flow after the position at which the flow separates [25]. The evidence presented above would suggest that the decrease in distortion levels will produce an increase in the performance of the intake. The understanding of the meaning of the redistribution of the flow inside the duct due to the engine face is the aim of this paragraph.

Firstly, in order to understand the mechanism an assumption is made: it is considered a rotor without any production of work with a uniform distributed flow with axial velocity V_a , i.e. a free-wheeling rotor [25] (Figure 2-27). In this case, due to the assumption made, no thrust or torque is produced at the blades. This

can be translated to a velocity triangle with the axial velocity V_a and the rotor tangential velocity V_t with an angle of attack that gives a zero lift. The effect of a steady state disturbance is to reduce the local value of total pressure which modifies the axial velocity [25]. In particular a reduction in total pressure leads to a lower value of axial velocity V'_a . The new triangle produced from this change will result in non-zero lift inducing the formation of torque or thrust on the blades, where the total pressure distortion is present. Since the system considered does not produce any work or thrust when in a steady state, the change in velocity is a transient condition and, after a certain amount of time, a new operating condition of no work or thrust is obtained [25]. In order to do so, however, the rotor has to adjust the velocity vector inside the duct in both magnitude and direction to obtain the desired net thrust or torque equal to zero [25].

In this context the regions with the highest energy will exchange energy with the regions with lowest energy. In the clean case, in other words without a windmilling fan at the exit, the high and low total pressure regions do not change down the length of the duct (under the assumption considered) but maintain the same orientation of the velocity vector field determined by the total pressure and uniform static pressure distribution [25].

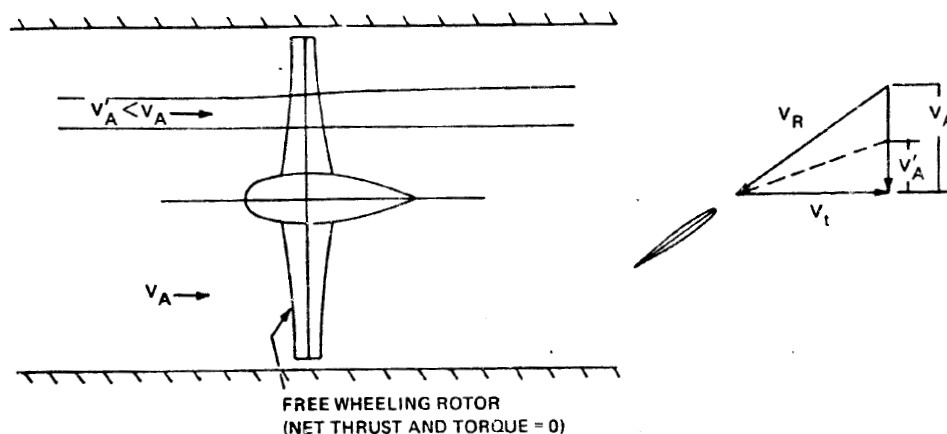


Figure 2-27 Inlet engine flow field in the wind milling rotor [25].

The windmilling case described is similar to a thrust producing rotor, namely the most general case. Placing a real engine downstream, in order to meet the

requirement in constant operating conditions and constant discharge static pressure, the rotor redistributes the flow approaching the engine, similarly to what happened in the windmilling fan [25]. However, it is important to note that, this flow redistribution is possible only if the non-uniformity is high enough to keep the blades stalled [25]. In the work done by Motycka [26] for Pratt & Whitney some interesting conclusions were drawn concerning a coupling between an advanced intake and the engine [26]. First of all, experiments showed that engines without the fan were more prone to flow separation than the ones with the fan [26]. The conclusion they reached was similar to the one discussed by Hodder [25], where the fan helped to redistribute the flow inside the intake, thus preventing flow separation and flow reversal (Figure 2-28).

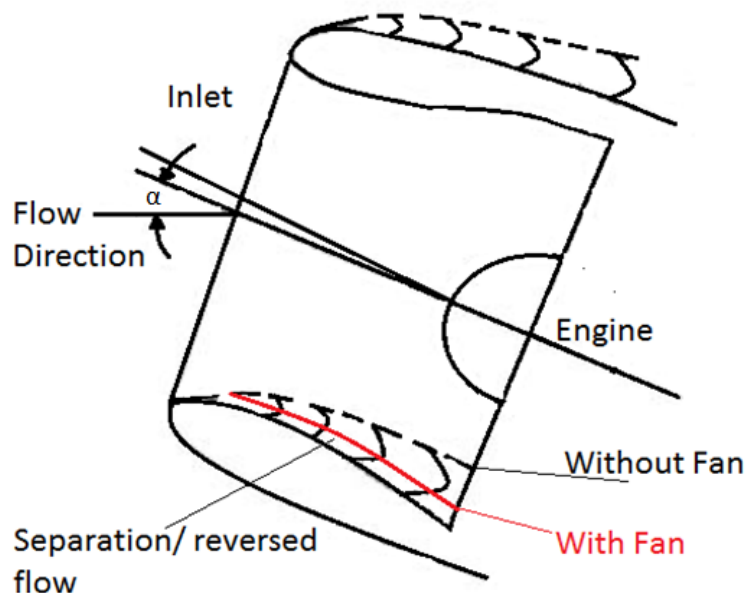


Figure 2-28 Effect of the engine on the flow inside the intake [26].

Motycka [26] also tested the intake and the fan in a different configuration by decoupling the intake from the downstream system, which choked the flow at the throat of the fan blades, thereby achieving sonic conditions at this section. The result of this last flow condition was again a decrease in the distortion levels inside the duct compared to the preceding cases [26], as described by Figure 2-29. The use of blockage rods were needed in order to maintain choked the flow also in coupled case.

If the compressor has a sufficient number of stages the radial velocity components are reduced by the radial pressure gradient, which is present for a sufficient distance [27]. Consequently, due to the uniform static pressure no further redistribution of the flow will appear downstream. In short compressors, since the radial component of velocity observed at the inlet of the system is somehow still present at the exit, a non-uniform static pressure distribution is observed. Therefore, flow redistribution appear both upstream and downstream the compressor [27]. This situation is described in Figure 2-30, which shows the axial velocity change both upstream and downstream for a short and a long compressor. The upstream attenuation is similar in the two cases apart from the magnitude, while the downstream redistribution for the case of a short compressor shows a mirrored shape. As already stated, there is no further change for the long compressor in the downstream flow [27].

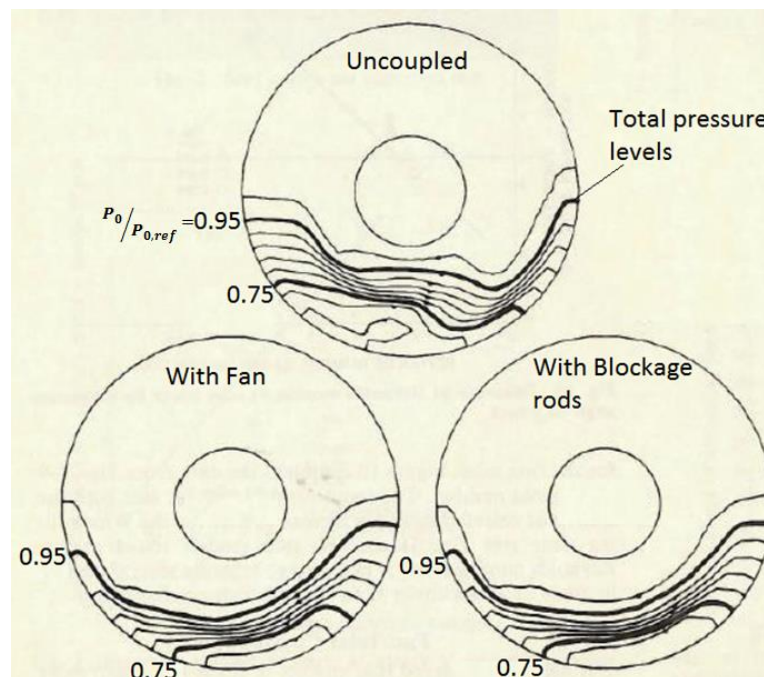


Figure 2-29 Inlet total pressure distortion levels in: (a) uncoupled case, (b) fan and intake coupled system, (c) choked coupled system [26].

In the experiments conducted, two different types of compressor design were considered. The first design presented a constant pressure rise while the second a variable pressure rise. Figure 2-30 shows the different curves in each compressor. If we look at the upstream regions for the long and short

compressors, even if there is a change in terms of pressure rise, the total attenuation stay the same. Looking instead at the tip and the hub, the rate of attenuations are different [27].

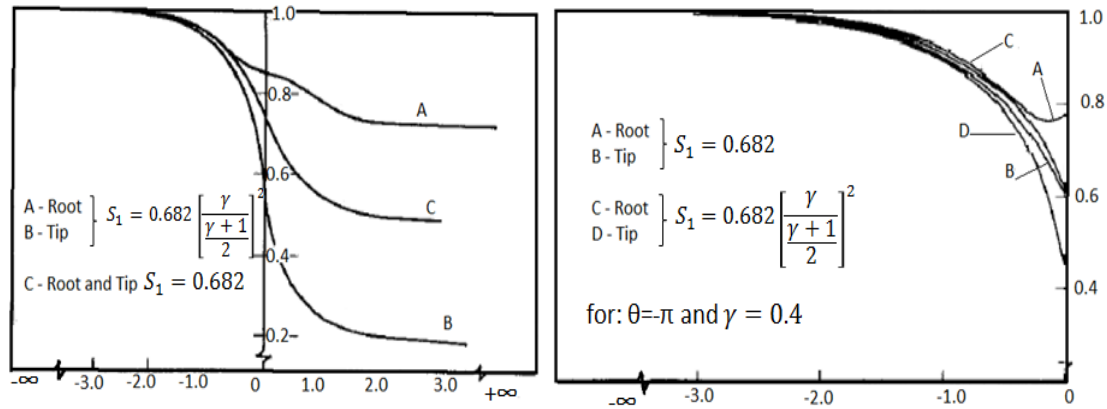


Figure 2-30 a) Short compressor flow redistribution b) Long compressor flow redistribution [27].

2.2 Topology of the flow

In this section, a description of the flow and a characterization of a 3D separated flow will be presented, bearing in mind the purposes of this project. More details concerning the basic definition of critical points, skin friction lines, are found in Appendix A.

In this approach some important considerations need to be made before starting the analysis. First of all, the separation will be studied in the most general way as a 3D phenomenon, but the flow properties (especially velocity field), will be considered independent of time, looking at a steady flow. Most commonly flows present unsteadiness and in this work, too, unsteadiness is studied using a transient approach in CFD simulation, but for simplicity of the following description an averaged flow field will be supposed [28]. Nevertheless, the following considerations can be applied in the same way to an unsteady flow looking at an instantaneous picture of the flow, like for example the one obtained from particle image velocimetry (PIV) [28]. Moreover, the theory described cannot be used as a predictive method but only a support to a proper

description of the field; it is based on the vector field which may come from experiments or CFD [28].

2.2.1 Separation and reattachment

In the description of the separation of the flow great importance is given to the saddle points and in particular to the two lines crossing the critical point, also called separation lines. Referring to Figure 2-31, there are two types of motion in the skin friction lines coming from upstream and located on each side of the separation line S_2 : the first group “turn right” and the second “turn left” [28]. Then, the lines start following S_1 , converging at it asymptotically. This behaviour, described in Figure 2-31 (a), is associated with the separation of the flow. Similarly it can be seen in Figure 2-31 (b), where the skin friction lines first moves along S_1 and then diverge from it. This is the reattachment of the flow [28].

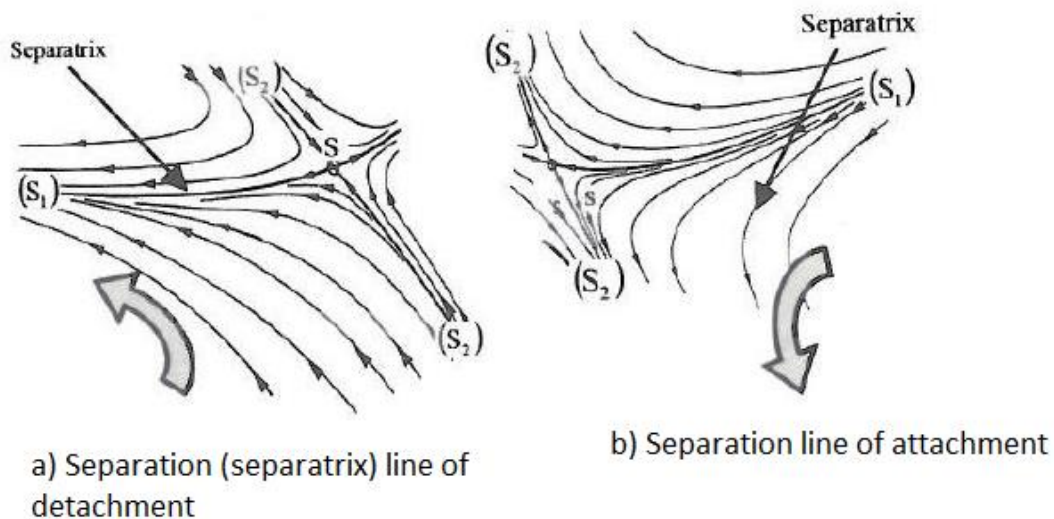


Figure 2-31 Skin friction lines; separation and attachment [28].

If we look at the behaviour above the wall and consider a streamtube limited by two skin friction lines f_1 and f_2 and two streamlines l_1 and l_2 , the width n , the height h and the mean density and velocity in the streamtube $\bar{\rho}$ and \bar{V} can be defined. If the case (a) of the preceding picture is considered, namely when skin friction lines are converging, then the distance n between f_1 and f_2 is reducing.

Therefore, since a steady flow is considered, the mass flow is constant and from continuity it is possible to observe an increase in height (eq. (2-24)):

$$h = \frac{\dot{m}}{\rho n \bar{V}} \quad (2-24)$$

Consequently, approaching the separation line S_1 , streamlines move away from the wall and again separation can be observed [28]. In the case of divergence from S_1 , described before in case (b), the opposite phenomena happen to the streamlines away from the wall and reattachment is observed. These aspects are summarized in Figure 2-32.

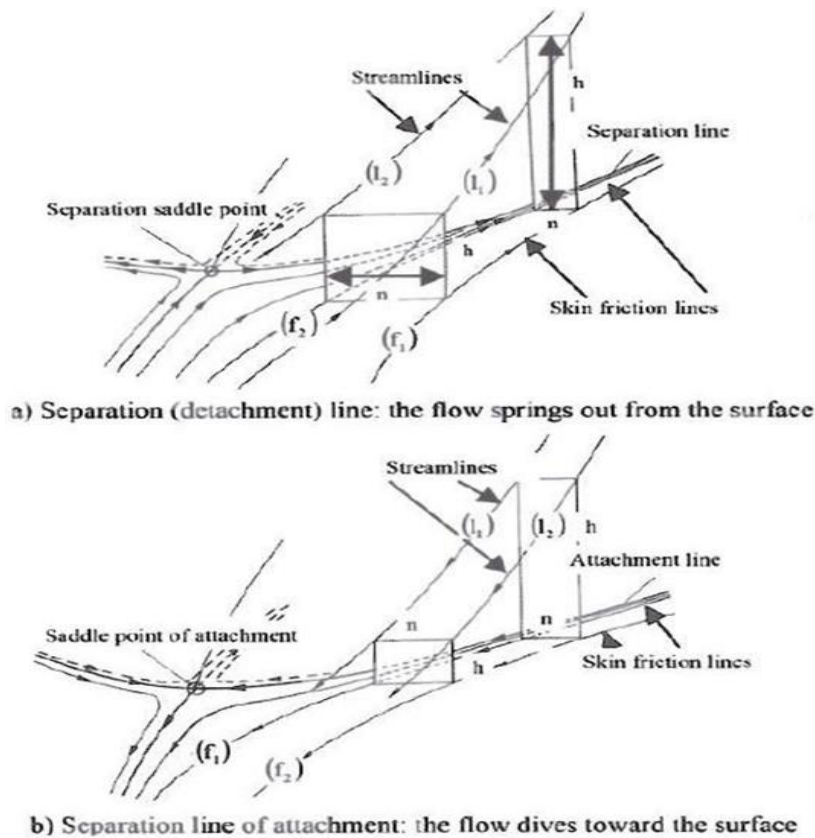
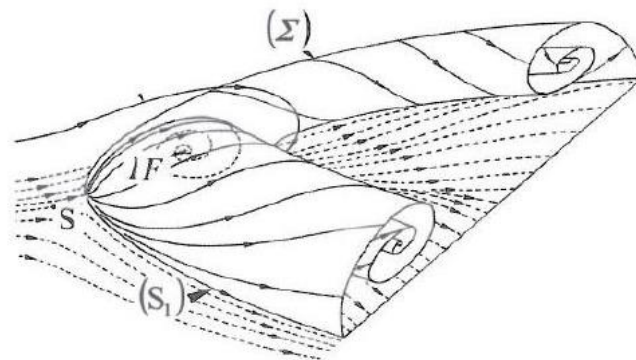


Figure 2-32 Separation and reattachment; away from the wall [28].

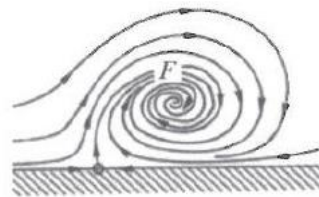
To conclude, as was evidenced in [28] we should emphasize that a flow can be considered as separated only if at least one saddle point is present on its surface. This a very important principle that can be used to rapidly understand the state of the flow.

three dimensional focus point, having a dissipative core around its own axis F [28]. This second type of vortex structure is described in Figure 2-34.

Although the description given is very general and a far more detailed insight can be needed for a deep understanding, the concepts presented are the ones needed in the following chapter to highlight the separation regions in the S-Duct, basing the study on skin friction lines and saddle points, from data coming from DDES and RANS simulation.



a) Wrapping of the separation surface



b) Section of the structure by a downstream plane

Figure 2-34 Horseshoe vortex structure; (a) 3D representation, (b) plane section [28].

2.3 Computational Fluid Dynamics: fundamentals

In this section the most important methods currently used in CFD are briefly described, with particular attention given to the ones specifically employed in this project, highlighting not only the general background theory but also the choices that led to their use.

On increasing the Reynolds number, the levels of unsteadiness in the flow field tends to increase which means that larger fluctuations in velocity, pressure and other variables that describe the state of the flow are observed [29]. In other

terms, an increase in the Reynolds number leads to turbulent eddies which are on a smaller scale but with a finer structure. From a computational point of view, it starts to be much harder to properly describe it, compared to a low Reynolds number flow because all the eddies have to be described, from the largest to the smallest. The complete solution of the flow can be achieved only by directly integrating the Navier-Stokes equation, i.e. by adopting the Direct Numerical Simulation (DNS). However, this method comes with very high computational costs and in normal engineering situations cannot be implemented [29].

Consequently, if we accept certain compromises, different methods can be used in practice that, depending on the applications in question, may be considered to be a good description of the flow field. In this project, RANS and DDES method are used and, after an introduction on Large Eddy Simulation method, they will be presented in the following paragraphs.

Figure 2-35, gives a summary of the different types of method, their limitations and how they can be used to analyse a flow. In Figure 2-35, the meaning of “resolved” is computed by code exactly, while “modelled” is used where an approximation of the solution is made.

2.3.1 RANS

Reynolds-Averaged Navier-Stokes (RANS), is the first method developed for numerical simulations but, due to the low computational costs, it is still widely used to simulate flow behaviour.

The flow field can be described by considering the variables as being composed of two terms: a mean value and a fluctuating part. The velocity flow field u , for example, can be written in the following way (eq. (2-25)):

$$\vec{u}(x, t) = \langle \vec{u} \rangle(x, t) + \vec{u}'(x, t) \quad (2-25)$$

where $\langle \vec{u} \rangle(x, t)$ represents the mean velocity field while $\vec{u}'(x, t)$ is the fluctuating component. The RANS method uses this definition of the flow variables to rewrite the Navier-Stokes system and so obtain the Reynolds-averaged

equations for the mean field [30]. In the case of an incompressible flow the following expression in conservation form is shown in eq. (2-26):

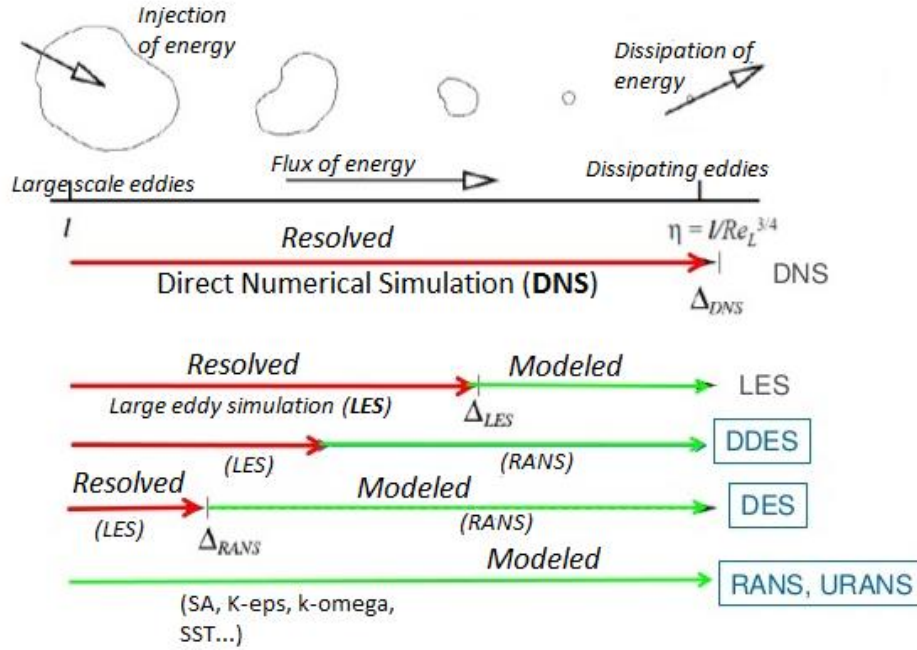


Figure 2-35 Characterization and field of application of different CFD models [29].

$$\rho \frac{\partial \langle u_i \rangle}{\partial t} + \rho \frac{\partial}{\partial x_j} (\langle u_i \rangle \langle u_j \rangle) = - \frac{\partial \langle p \rangle}{\partial x_j} + \mu \nabla^2 \langle u_i \rangle - \frac{\partial \tau_{ij}}{\partial x_j}, \quad \frac{\partial \langle u_i \rangle}{\partial x_j} = 0 \quad (2-26)$$

where in particular, u is the velocity field, p is the static pressure distribution and τ is called Reynolds stress tensor and it can be expressed as follows (eq. (2-27)):

$$\tau_{ij} = \rho \langle u_i' u_j' \rangle = \rho \langle u_i u_j \rangle - \rho \langle u_i \rangle \langle u_j \rangle \quad (2-27)$$

In the case of compressible flows the energy equation and the change in density should also be added to the system. In any case, the system will not be closed due to the presence of the unknown stress tensor that cannot be expressed as a function of $\langle u \rangle$ or $\langle p \rangle$. For this reason, using some approximations, many different closure models have been developed to evaluate τ_{ij} and obtain a numerical solution for the Reynolds-averaged equations [30]. The most widely used assumption is the Eddy Viscosity Hypothesis where it is assumed that the turbulent transport τ_{ij} depends on the

mean velocity gradients in the same way as molecular transport depends on the velocity [30]. It should be noted that there is not a theoretical explanation for this similarity between the motion of molecules and the eddies. Therefore, mathematically the hypothesis can be formalized in the following way (eq. (2-28)):

$$\tau_{ij} = \rho \langle u_i' u_j' \rangle = -2\mu_t \langle S_{ij} \rangle + \frac{2}{3} \rho \delta_{ij} k \quad (2-28)$$

where $\mu_t(x, t)$ is the eddy viscosity, δ_{ij} is the Kronecker delta function. S_{ij} and k are respectively the rate of strain tensor of the mean flow and the turbulent kinetic energy and they can be written seen in eq. (2-29) and eq. (2-30):

$$\langle S_{ij} \rangle = 0.5 \left(\frac{\partial \langle u_i \rangle}{\partial x_j} + \frac{\partial \langle u_j \rangle}{\partial x_i} \right) \quad (2-29)$$

$$k = 0.5 \langle u_i' u_i' \rangle \quad (2-30)$$

Depending on the characterization of the preceding parameters and the equations used to determine k and μ_t , different types of models (Algebraic models, two-equation models, etc.) are used but all of them are based on the Eddy Viscosity Hypothesis. Inside the two equation models, the Shear Stress Transport k - ω model (SST k - ω) can be found. It gives good results in regions where separation is present. This model tries to overcome the limits imposed by Standard k - ϵ , maintaining at the same time a good resolution without excessive computational effort. This is a very efficient and solid method; the only negative aspect is related to the higher sensitivity to inlet freestream turbulence [31].

2.3.2 LES and DES

The drawback of the RANS method is that, because it is only looking at mean flow, it cannot describe unsteadiness. A way to improve this, without using a DNS method, is to solve a portion of the turbulence in a region of the domain. One of the most widely used approaches is the Large Eddy Simulation (LES), where the mean flow and the unsteady large-scale and intermediate-scale eddies are directly calculated [30] while the small eddies are modelled. For this reason LES, which is a transient method, is regarded as being half way

between RANS and DNS. Obviously, since it does not include all the eddies, it generates an error in the solution compared to DNS, but that is smaller than the error in RANS. However, the application of LES in engineering is still limited due to the high computational costs involved. It is generally used where a detailed definition and resolution of the boundary layer is required [30].

Although the LES is very reliable, in many practical situations a less detailed description of the flow is acceptable during the CFD simulation because it takes much less time. For this reason, different hybrid models have been developed in which a combination of RANS and LES is used. The one described in the following paragraph and used in this project is called Detached Eddy Simulation (DES) which is again a time-dependent approach.

The target of the DES are flows with a high Reynolds number and with regions of large separation, and for this reason it is well suited for aerospace applications [32]. Basically, using DES it is possible to switch between RANS and LES depending on the position on the grid: the area close to the boundary layer is described using a RANS model while away from the surface, i.e. in the core of the flow, the LES approach is applied [32]. One of the most critical aspects of the model that can negatively affect the outcome, is to correctly determine the position on the grid where the switch should be made. In the regions where the grid spacing is smaller than the turbulent length scale LES is used, whereas the RANS method describes grid regions where the mesh is not fine enough to solve the eddies. The method used to describe and detect the boundary layer, namely RANS method applied, depends on the context. However, the study of different highly separated flows and in particular the work of Menter and Kuntz [33] suggested that the SST $k-\omega$ model is the best compromise. This is fully described in a DES on a separated flow on an Ahmed body [33]. The choice and the separation of the two regions is not always so clear and it may happen that the grid refinement is close to both RANS and LES resolutions, commonly called grey regions [34]. This of course appears close to the boundary layer, where the transition between RANS and LES is present. As a consequence, instabilities and errors in the description of the flow are

introduced. The most common phenomena caused by the preceding problem is called “Grid-induced separation” [32], where the solution shows an artificial separation of the flow that does not in fact exist.

In recent years, in order to overcome this basic limitation of DES, new improved versions of the model have been developed mainly by Spalart [35]. In the so called Delayed Detached Eddy Simulation (DDES), after the boundary layer has been detected, RANS is prolonged even though the grid spacing would normally cause a switch to the LES method [35]. Now the detection of the position at which the move from RANS to LES is made is dependent on eddy viscosity and therefore on the solution [32]. As with DES, the DDES method can also be used with the SST k - ω model for the RANS regions and this is the configuration adopted in this project.

2.4 Summary

2.4.1 Most recent developments

Numerous experimental and computational studies carried out mainly in the last 2 years at Cranfield University have investigated the unsteadiness of S-ducts at different Mach number, for different geometries and flow conditions.

Firstly, the analysis of Gil-Prieto et al. [9] is of interest for the purposes of this project. They used an S-duct geometry with an offset of $H/L=0.50$, area ratio of $AR=1.52$ and a Reynolds number $Re_D = 7.1 \times 10^5$ for a Mach number of 0.27 in a DDES [9]. The same geometry is adopted in this project. A comparison between the CFD results and the stereo particle image velocimetry (SPIV) measurements taken at the AIP, was made. The main conclusion was the close agreement between the CFD results and the experimental data for the mean flow field of the three velocity components u , v , w [9], where w is the stream-wise velocity, v vertical velocity and u the lateral velocity, as showed in Figure 2-12. The DDES allows the maximum unsteadiness in the flow to be determined and predicted even if, compared with the experimental results, the fluctuating levels are slightly overpredicted (Figure 2-36) [9].

Furthermore, the work of Gil-Prieto et al. [9] not only demonstrates the feasibility of DDES to describe the unsteady characteristics of the flow in S-ducts but also how it can be used to determine the most energetic structures at the AIP. This is important because the highest dynamic distortion delivered to the engine, and which affects its operation and performance, is determined by them [9].

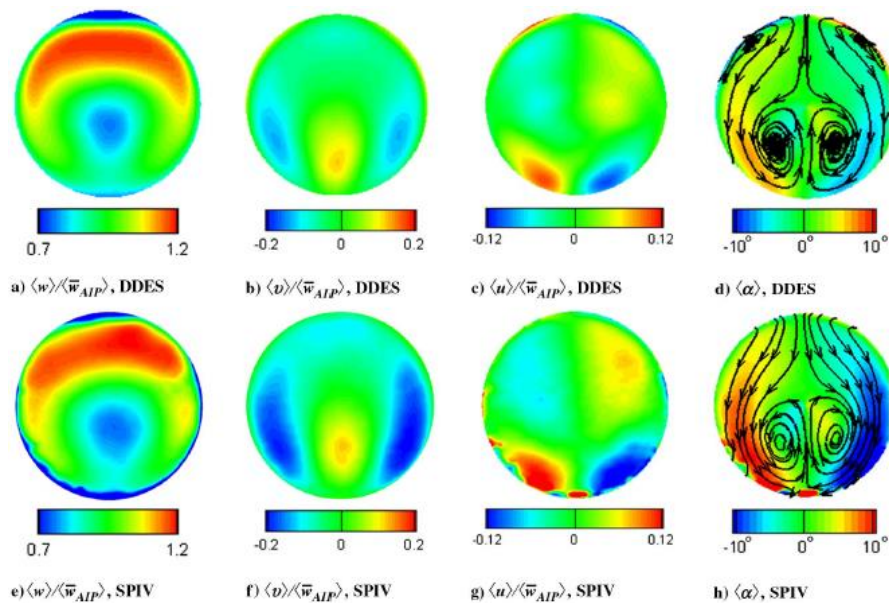


Figure 2-36 Comparison of the normalised velocity in the three directions and swirl angle at the AIP between DDES (time-averaged flow field) and SPIV [9].

Secondly, Macmanus et al. [2], using a DDES method for different geometries (with different offsets), Mach number and Reynolds number, underlined and quantified the impact on the unsteadiness of these configurations [2]. The results highlight the dynamic nature of the flow inside the S-duct for total pressure and swirl distortion which were, in the case of swirl distortion, twice as large in the unsteady flow field as the averaged one [2]. From a statistical analysis point of view, increasing the offset of the S-duct, reduces the DC60 parameter while the RDI metric increases substantially [2]. Furthermore, moving from the low-offset to a high-offset geometry, the distinctions between the mechanisms that drive the unsteadiness are less clear. If in the low-offset case, secondary flows and stream-wise flow separation determine the nature of the flow, the unsteadiness is more broadband in the high-offset [2]. In Figure 2-37, by increasing the off-set of the S-duct H/L (Figure 2-7) from 0.268 (case 1) to

0.493 (case 3), the previous statements can be observed, with the peak value of the swirl angle increasing from 12 to 20 deg and the main loss in total pressure moving to a central position [2]. In the experimental facility of Cranfield University the unsteady three-component velocity field for two S-ducts was determined experimentally. The geometry is presented in Table 1 where the values are taken from Gil-Prieto et al. [4]. Gil-Prieto et al. [4] used DDES to quantify the unsteadiness for the geometry in question at a Mach number of 0.27, the same used in this project.

Table 1 S-duct parameters [4].

Parameter	High off-set	Low off-set
AR	1.52	1.52
H/L	0.50	0.27
D_{in}	121.6 mm	121.6 mm
L/D_{in}	4.95	5.00

The flow unsteadiness leads to larger peak values of swirl distortion (difference of one order of magnitude) compared to the ones evaluated from the mean flow [4]. The swirl pattern in the two cases is also different. While we may find a twin swirl in the mean flow, in the unsteady flow even bulk-swirl patterns are present [4]. The most important conclusion drawn by Gil-Prieto et al. [4] can be summarized by looking at the joint PDF maps (Figure 2-38) that highlight the range and trend between the descriptors (Swirl Pair and Swirl Directivity) and also show the probability of the event. This is possible using the probability distribution function (PDF) [4].

In Chapter 4 we will have a closer look at these diagrams, but suffice it to say that, as stated in section 2.1.5.2 values of SD close to 0 indicate the formation of a twin swirl while values of -1 or +1 point to the formation of a negative/positive bulk swirl. The maps show that in the low offset case the swirl distortion pattern is in a range of values where a twin-swirl is more probable (which is also observed in the mean flow), while in the high offset negative or

positive bulk swirl and twin-swirl are equally likely to appear. This second situation is partially in contrast with the mean flow study [4].

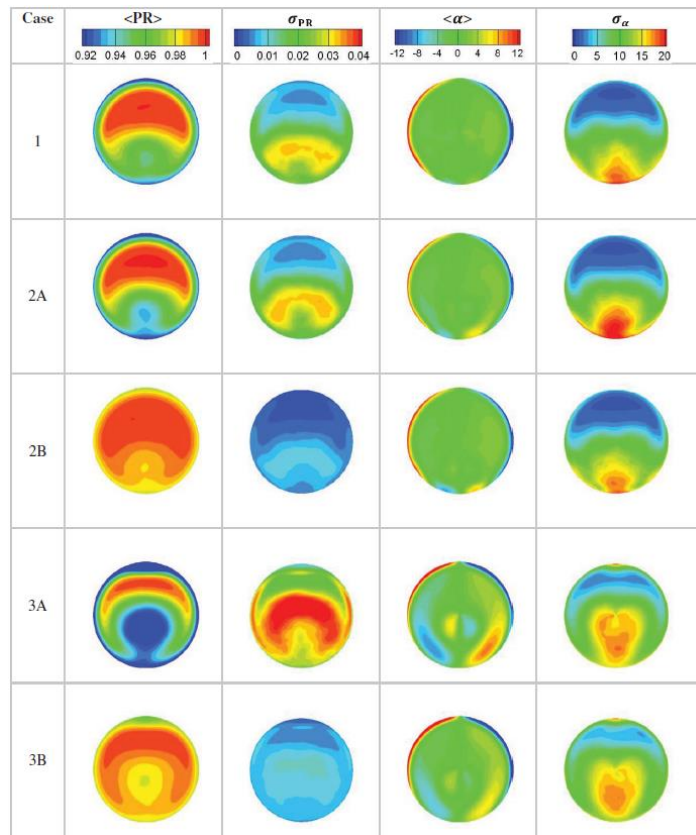


Figure 2-37 Pressure recovery coefficient and Swirl (with standard deviations) for different offsets H/L [2].

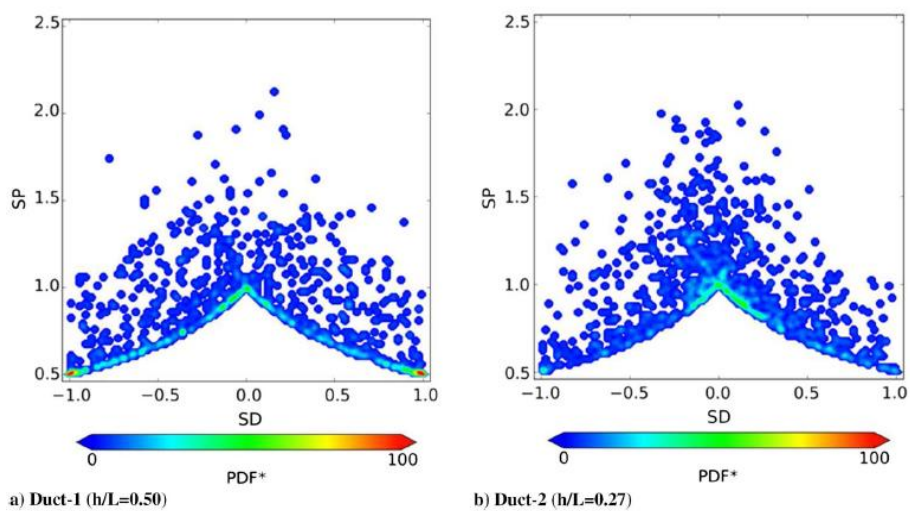


Figure 2-38 joint PDF maps: SD-SP swirl descriptors; a) High Offset, b) Low offset [4].

2.4.2 State of the art and project roadmap

During recent years at Cranfield University a lot of effort has been put into the study of complex installations. The present project can be considered to be a final step in a series of investigations of the mutual interaction between a static fan at the exit and the flow inside the S-duct. The work presented here is built upon a previous study presented by A. Giacomobello [36] in 2016 in his own master's thesis. It is mainly the position of the fan simulator that characterizes this work and leads to an improved description and understanding of this complex aerodynamic interaction. The next chapter explores the geometrical characteristics in greater detail. It is important to note that in this work the spinner region finishes exactly on the AIP plane, i.e. it is inside the duct while in the preceding investigation the spinner was outside the AIP ($0.458D_{AIP}$ downstream, where $D_{AIP} = 150$ mm).

Consequently, not only is the geometry more representative of a possible configuration for highly integrated aero engine systems but also in this study the highest impact of the fan on the flow field can be highlighted. Furthermore, thanks to the results obtained by A. Soli [12] during his master's thesis, a comparison with the same S-duct without the fan is possible. As a consequence, a real understanding of the impact of the static fan on the flow is possible.

Another important improvement over previous works is represented by the change in post-processing analysis. In the past POD, spectral analysis and other well-established methods were employed, using codes developed by Cranfield University in Python™. This project takes a first step towards using the DMD model. The reliability and potential advantages of this new method are well-known and convinced the team to start to analyze and study it.

The project was divided into three different phases, as described in Figure 2-39. The first step was to modify the geometry and create a high quality mesh in order to accurately describe the flow during simulation. The software used is ANSYS ICEM v17.1. During the second stage, the settings of the simulation were chosen and a first analysis of the results was carried out using ANSYS

Fluent v17.1 and Tecplot 360. The final phase saw the implementation of post-processing to assess the impact of distortion on engine performance, using both Tecplot and codes written in Python. The literature review continued throughout the lifetime of the project.

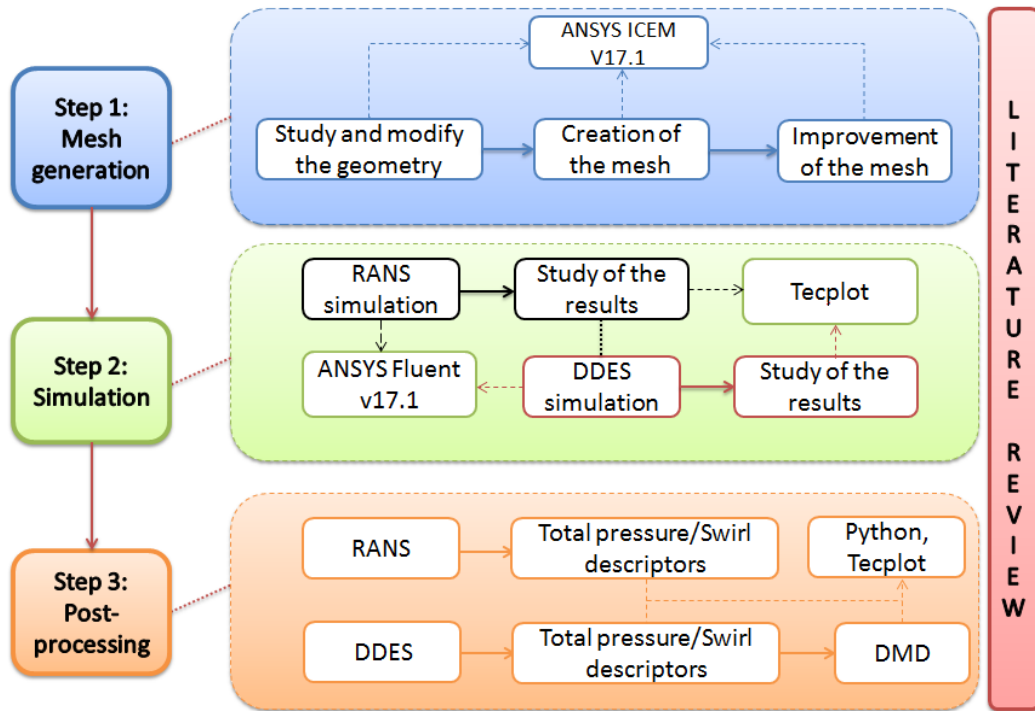


Figure 2-39 Road map of the thesis project.

3 METHODOLOGY

The aim of this chapter is to present the fundamentals in terms of settings and geometry and the procedure followed to obtain the results. The chapter is divided into three sections. The first concerns the geometry, the second the mesh and in the third part the settings.

3.1 Geometry

The geometry of the duct used in this work is the same used by A. Soli [12] while the fan is the same of A. Giacomobello [36], for the studies conducted during their master thesis in Cranfield University. The main difference is related to the new position of the fan with respect to the AIP plane. In particular, the geometry comes from an experimental work (Figure 3-1) carried out in Cranfield University and described in section 2.5.1 in the work of Macmanus et al. [2] and Gil-Prieto et al. [5] for the experimental assessment of unsteadiness in complex intakes. However, the S-duct used is a scaled version of the one tested by Garnier [40] in the ONERA facility. In this project all the dimensions are the same as those used in Gil-Prieto's work ([10]-[5]) for the high offset, with the addition of a static fan at the exit of the AIP. Only the high-offset S-Duct is studied in this project. Moreover, the S-Duct modelled in ICEM, imported from a CAD file, presents a circular cross section with a centreline created by intersection of two consecutive arcs of 52° ; this angle is called θ_{max} in Figure 3-2. Figure 3-2 shows the most important parameters for the geometry of the duct, considering an inlet diameter D_{in} of 121.6 mm. Since a constant area is adopted after the AIP, the diameter at the AIP section (D_{AIP}) as well as at the outlet diameter (D_{out}) are equal. Consequently $D_{AIP} = D_{out} = 150\text{mm}$.

A schematic picture of the nomenclature adopted is shown in Figure 3-2. It is worth to note the position of the Cartesian system of reference, where the z-axis is in the axial direction and consequently with "z" is indicated the position of a point with respect to the origin, along the axial extension of the duct. Y is the vertical position and X is the lateral position, entering the paper. This was already described in section 2.1.3 on page 26.

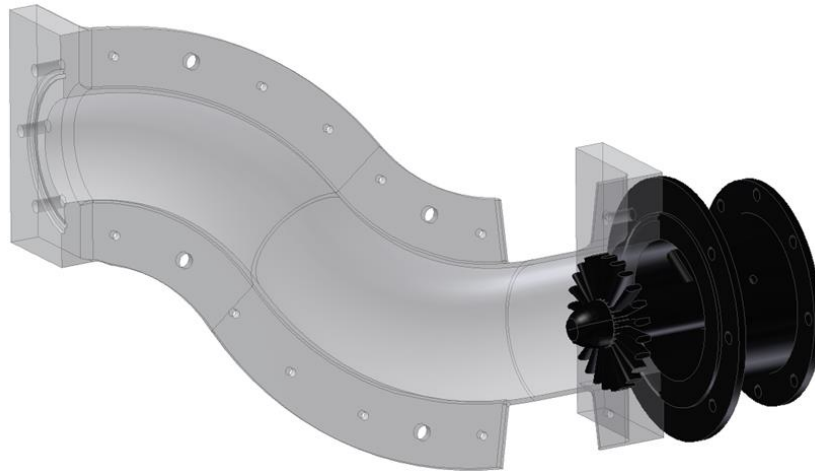


Figure 3-1 3D representation of the system.

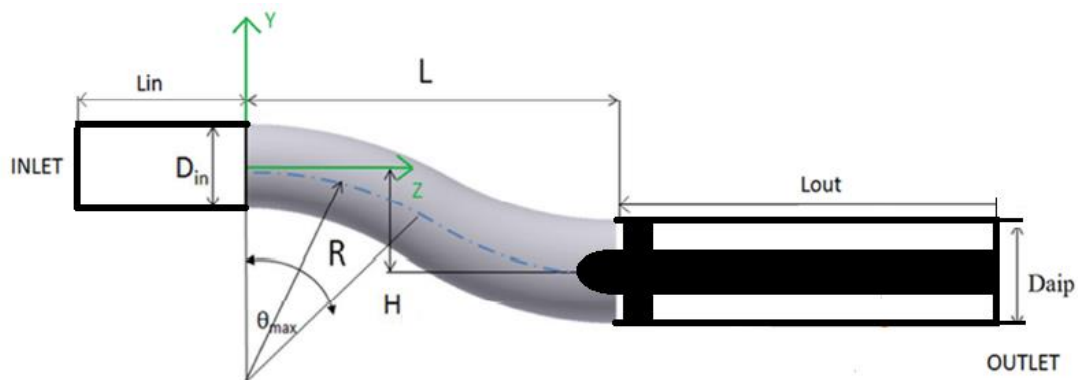


Figure 3-2 Schematic of the S-duct and representation of the nomenclature used.

The fan simulator consists of three different parts (Figure 3-4):

1. central cylinder
2. spinner
3. blades

The cylinder has a diameter of 28.5 mm and 24 blades are attached to it. In particular the aerofoil is a NACA symmetrical profile with a chord c of 30 mm and a maximum thickness reached at 30% of the chord itself. This position corresponds to the throat of the channel and the blade geometry has been created in order to choke the flow for an operating inlet Mach number of 0.27 [8]. No tip clearance is considered in this model. The third part to mention is the spinner, which corresponds to the frontal nose of the fan simulator. These main

regions of the fan simulator can be observed in greater detail in Figure 3-3, which is the real system adopted in the experiments conducted in Cranfield University.



Figure 3-3 Fan simulator used by Cranfield University in the experiments [8].

As has already been mentioned, the fan simulator is positioned at the AIP plane and the spinner will fall inside the S-duct in order to assess the impact on the flow field upstream. The leading edge of the blades, which are 7.3 mm from the end of the spinner section, are also 7.3 mm away from the AIP. Consequently, the AIP position is at the end of the spinner and the start of the cylinder. Obviously, the greatest effect of the fan on the flow is observed by positioning the AIP plane exactly at the leading edge of the blades, thus avoiding the gap of 7.3 mm, but this compromise was the best way of guaranteeing an acceptable quality of the mesh and consequently of the solution, because the coupling between the curvature of the S-duct and the spinner region of the fan was less complex. As will be explained in the next section, such an arrangement ensures that a very good quality of mesh is achieved. Figure 3-4 “q” is the spacing between the end of the spinner and the leading edge of the blades and “b” is length of the spinner. “d”, which will be described in greater detail in the

following section, corresponds to the length of mesh in the spinner region, which is made up of the last part of the S-Duct and the spinner itself.

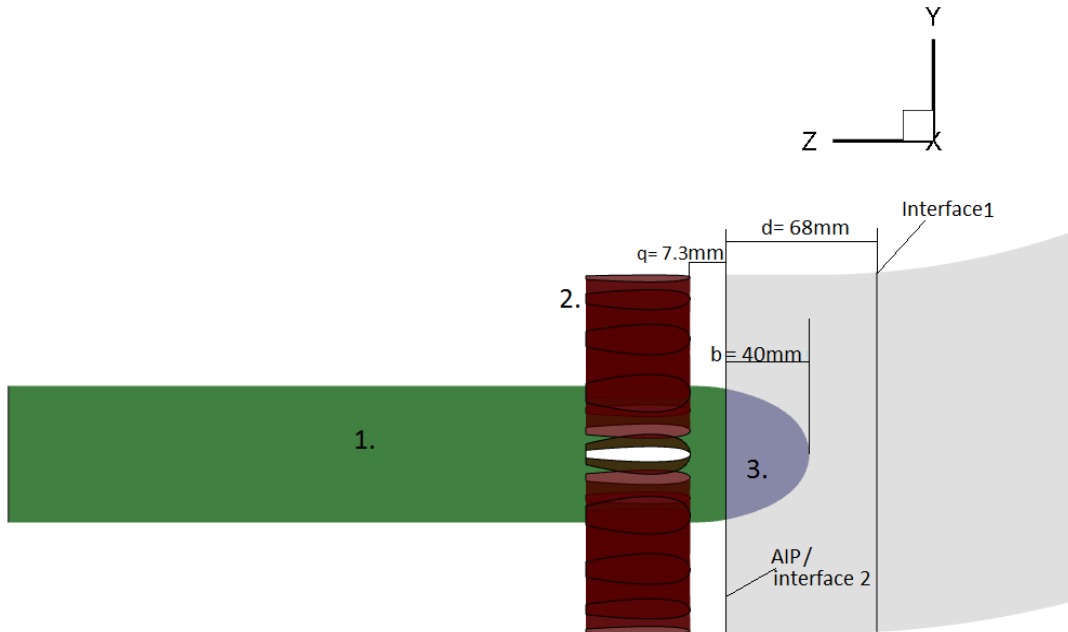


Figure 3-4 Regions of the Fan simulator and position of the spinner; 1. Cylinder, 2. Blades, 3. Spinner.

Table 2 Summary of the leading dimensions.

$AR = \left(D_{out}/D_{in}\right)^2$	1.52
L/D_{in}	4.95
H/L (offset)	5.0
$\gamma = R_{in}/R_C$	0.16
b/D_{out}	0.26
q/D_{out}	0.049
q/c	0.243

Finally, the position of a certain number of planes is considered. These sections, normal to the duct and for this reason always circular, are of paramount importance for the analysis of the results and the comprehension of the flow field. All the values are non-dimensional, where:

$$A_1 = \frac{z_{LE} - z_{plane,i}}{D_{out}}$$

$$A_2 = \frac{z_{spinner\ nose} - z_{plane,i}}{D_{out}}$$

$$A_3 = \frac{z_{outlet} - z_{plane,i}}{D_{out}}$$

and $z_{plane,i}$ corresponds to the axial position of the plane considered, $z_{spinner\ nose}$ is the axial position of the tip of the spinner and z_{LE} is the axial position of the leading edge of the blades. As far as the outcome is concerned, the most important section is the AIP.

Table 3 Summary of the position of each plane of interest.

	Plane M	Plane N	Plane O	Plane 1	Plane 2	Plane 3	Plane 4	Plane 5	AIP
z/D_{out}	2.851	3.257	3.688	3.837	3.963	4.046	4.162	4.226	4.266
A_1	1.506	1.1	0.669	0.52	0.394	0.311	0.195	0.131	0.049
A_2	1.18	0.775	0.344	0.194	0.069	-0.01	-0.13	-0.19	-0.23
A_3	3.43	3.023	2.592	2.443	2.318	2.234	2.119	2.055	2.015

In order to decrease the action of the inlet and outlet boundary conditions on the results of the simulation two extensions are added to the system:

1. *Inlet cylinder*, with constant diameter equal to D_{in} and of length L_{in} (Figure 3-2); more precisely $L_{in} = 2D_{in}$.
2. *Outlet cylinder*, positioned after the blades and characterized by a total length of $L_{out} = 2D_{out}$ (Figure 3-2).

3.2 Mesh

3.2.1 Approach and quality of the mesh

Once the geometry created with CAD software in previous works made in Cranfield University was imported into ANSYS ICEM CFD v17.1, the following method of creating a new mesh for the new position of the fan was implemented.

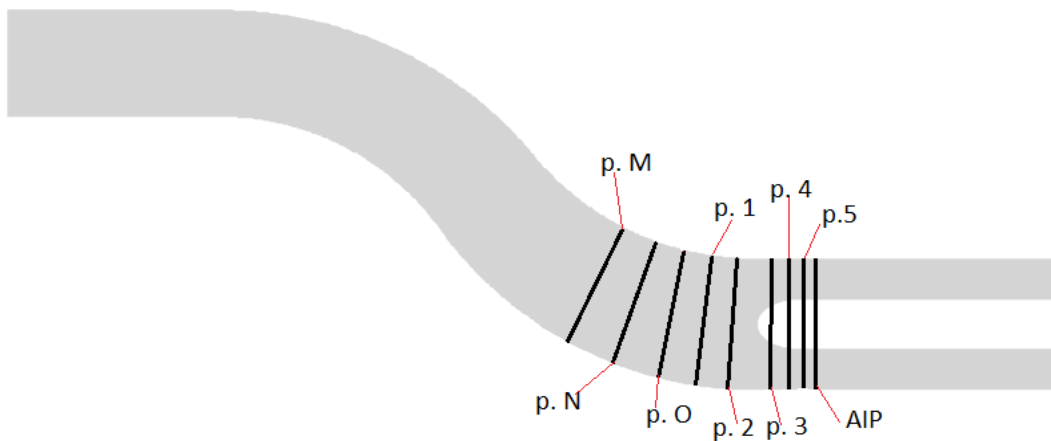


Figure 3-5 Qualitative schematic of the position of each plane (p. abbreviation for plane).

First of all the geometry, composed by the S-duct and the fan simulator, was divided into three parts cutting the system on ICEM. The first section goes from the inlet (as shown in Figure 3-2) to the interface 1 plane (Figure 3-4). The second region extends from interface 1 to the end of the spinner, namely the AIP plane (interface 2). Consequently, the second mesh contains both the spinner and the final part of the S-duct, i.e. until the AIP. The last section corresponds to the fan simulator with the exception of the spinner and goes from the AIP to the outlet. Interface and AIP planes are the two positions where the cut was applied to the geometry. As highlighted, these three parts were meshed separately and then merged again in ICEM and finally exported in Fluent for the study. The simulation was launched by adopting a particular command in Fluent which applies grid interfaces as a boundary condition for the solver to these specific intersecting regions. In this situation the solver applies a non-conformal mesh, which means that the flow at the interface is studied on nodes that have different locations on the interior and exterior planes (Figure 3-6).

It should be emphasized that the creation of the mesh in terms of the number of nodes, for the purposes of this project, satisfied certain important requirements.

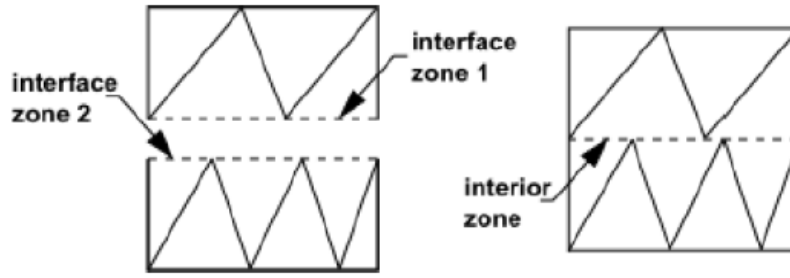


Figure 3-6 Non-conformal mesh and different location of the nodes.

Table 4 Position of the interfaces.

	Interface 1	AIP (Interface 2)
z/D_{out}	3.842	4.266
A_1	0.515	0.049
A_2	0.189	-0.234
A_3	2.438	2.015

First of all, the results should not depend on the number of nodes used and consequently three meshes (medium, fine and coarse) were produced in order to do a grid independence study. Moreover, since a comparison with the results of the clean case is one of the aims of this work, a similar number of nodes is required. However, due to the presence of the fan simulator, it is impossible to have exactly the same values. A more detailed discussion of this topic will be presented in Section 3.2.2. Furthermore, the computational time needed for the simulation to converge is an important factor when designing the mesh. Finally, the mesh should be fine enough to fully describe the unsteadiness and the characteristics of the flow. A trade-off between these aspects led to a total number of nodes of about 6×10^6 . In the following three sections each mesh is presented and described in terms of structure and quality.

3.2.1.1 Mesh: S-Duct

The first mesh of the S-duct is composed of a central H-grid connected to an O-grid which furnishes a better description of the regions close to the walls and consequently it properly studies the boundary layer. Furthermore, in order to solve the boundary layer the distance of the first cell from the wall was

calculated to obtain a $y^+=1$. The online open source and widely used NASA tool called “Viscous Grid Spacing Calculator”, was used for this purpose. Taking into consideration the free stream condition of the flow, the height of the first cell determined with the tool is $1.233\mu\text{m}$. Figure 3-7 shows the mesh for the S-duct, where b) represents the structure of the mesh for every perpendicular section of the duct, from the inlet to the interface plane.

As already explained, three different meshes (medium, fine, coarse) were used in order to conduct the grid independency study. In the end the mesh used for the calculation was the medium one with about 3.6×10^6 nodes.

Table 5 shows the number of nodes in each of the three cases and in particular the lowest values of angle and quality in order to consider the worst cells in the mesh.

As the table shows, very high quality was achieved across the whole system. From the literature a value of angles greater than 20° is desirable, while a determinant as close as possible to 1 is needed [37].

3.2.1.2 Mesh: Spinner

The second region consists of the last part of the duct (from the interface 1 to the AIP or interface 2) and the spinner. In this part a greater complexity of mesh is observed due to the interaction of the spinner with the curvature of the duct. Even if the quality decreases slightly, a reliable mesh is obtained (Table 6). The block strategy followed is similar to the preceding one. An H-grid and an O-grid were created but then the O-grid was divided into two parts in order to delete the central block around the spinner. Using the same NASA tool, the height of the first cell was determined and was the same as the value previously set ($1.233\mu\text{m}$) for the main duct. In this way a y^+ equal to one is reached.

Table 5 Nodes and quality; first region of the mesh.

	Nodes	Angle	Determinant 3x3x3
Coarse Mesh	3.3×10^6	45.34	0.8
Medium Mesh	3.5×10^6	45.53	0.8
Fine Mesh	5.0×10^6	45.21	0.8

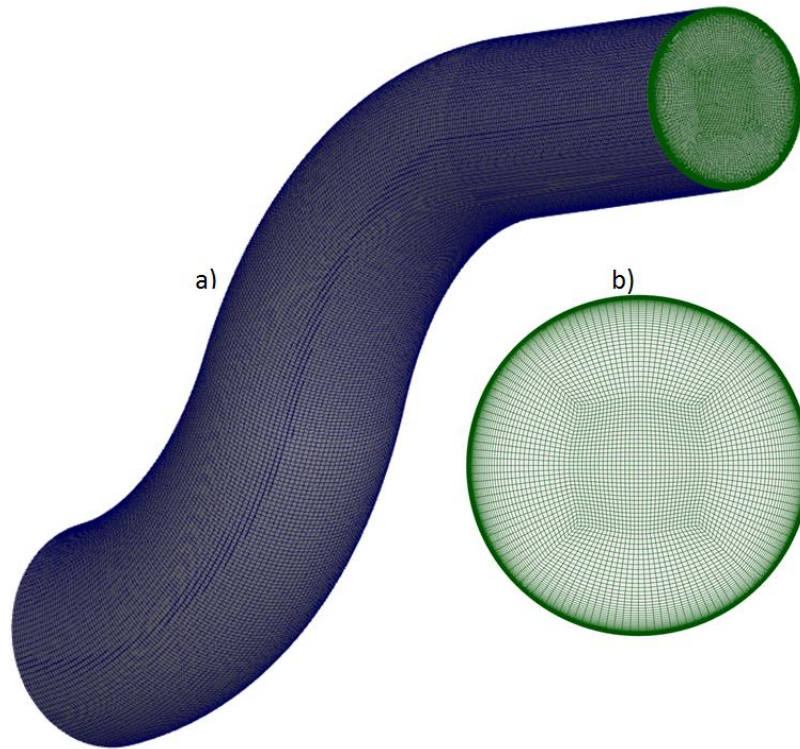


Figure 3-7 a) Mesh structure of the S-duct from inlet (right) to the interface (left), b) perpendicular section of the mesh of the duct.

Table 6 Nodes and quality; second region of the mesh.

	Nodes	Angle	Determinant 3x3x3
Coarse Mesh	2.1×10^5	25.12	0.6
Medium Mesh	2.5×10^5	27.43	0.6
Coarse Mesh	4.0×10^5	23.76	0.6

3.2.1.3 Mesh: Fan simulator

The last mesh, namely the fan simulator, was created following the same approach described by A. Giacomobello [36]. Firstly, the geometry of only one strut was imported into ICEM and the mesh for that single passage was implemented. The geometry was divided into three parts and an O-grid was created around the aerofoil. Finally, due to the symmetry of the problem, a rotation of 360° of the single passage was performed in order to obtain the desired final shape of the system with 24 struts (Figure 3-9). In this case the initial height of the first cell was set at $1.233\mu\text{m}$, in order to meet the requirements for the y^+ . A total number of nodes of about 2.3×10^6 was used in

the mesh adopted in the simulation. In Table 7 a summary of the grid is presented, and again good overall quality was ensured.

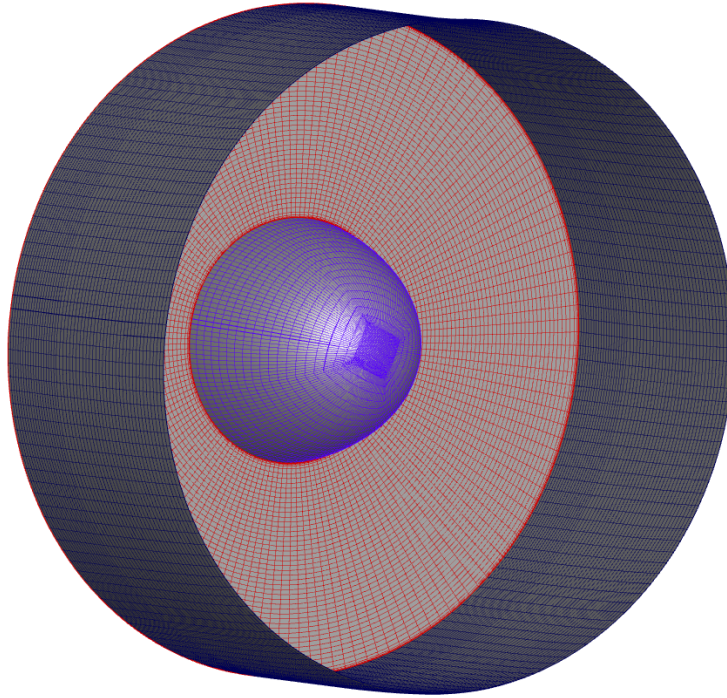


Figure 3-8 Mesh of the spinner and final part of the S-Duct.

3.2.2 Mesh similarity and mesh requirements

As previously mentioned, in order to compare the results obtained in this project with the work done by A. Soli [12] (Figure 3-10), it was important to guarantee not only the same operating conditions in the set-up of the simulation, but also a similar mesh.

Table 7 Nodes and quality; third region of the mesh.

	Nodes	Angle	Determinant 3x3x3
Coarse Mesh	2.0×10^6	36.11	0.7
Medium Mesh	2.3×10^6	37.39	0.7
Fine Mesh	3.8×10^6	35.71	0.6

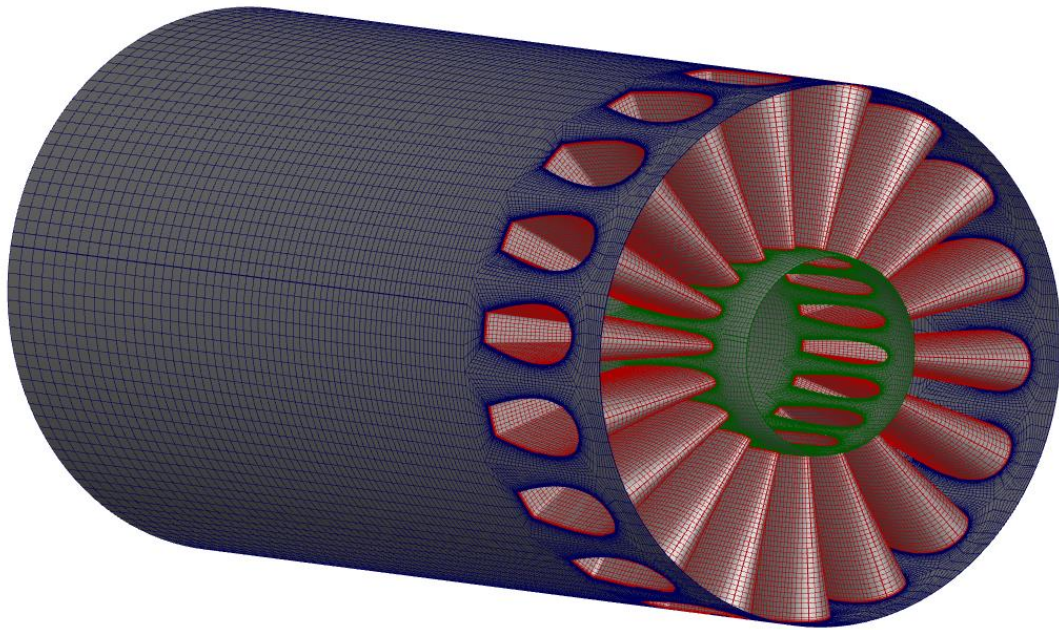


Figure 3-9 Mesh of the fan simulator.

Obviously, because the meshes used in A.Soli's clean case and the case analysed in this work present different complexities, two identical meshes cannot be obtained. but at least the following parameters should be as close as possible :

1. Number of nodes
2. Cell dimensions

It is important to note that in this context, the medium mesh was chosen because, as has already been explained, it is the one that best meets the requirements. The fine and coarse meshes, after a similar study to the one that will be presented in this section, were excluded. For this reason, the total number of nodes will be about 5.94×10^6 , considering all three regions. In Table 8 the comparison between the two meshes is summarized in terms of both nodes and cell dimensions. As part of the analysis, the worst case is considered. This means that cells with maximum dimension are studied since in these circumstances the largest negative impact on the flow description is seen. In the table presented, Δx , Δy , Δz are the dimensions in the system of reference (Figure 3-2) of the single cell, i.e. the cell with the maximum size.

Table 8 comparison between the mesh used in this project and A. Soli's mesh.

	Total Nodes	Δx [μm]	Δy [μm]	Δz [μm]
S-duct with Fan simulator	5.9×10^6	3.723	4.656	4.627
Clean S-duct	5×10^6	3.695	4.466	4.434
$\% \text{ change} = \frac{\Delta x_1 - \Delta x_2}{\Delta x_1} \times 100$	—	0.75%	4.2%	4.1%

Consequently, if we look at Table 8, the two meshes can be considered similar in terms of size and nodes and a comparison between the two sets of results is possible.

Another important aspect to consider during the creation of the mesh is related to the requirements for the mesh driven by the models adopted in the simulation. In this project, RANS and DDES methods are used and, as far as they are concerned, the following requirements need to be met. Starting with RANS, there are two important things to ensure:

1. The y^+ at the walls has to be lower than one; this is analysed later, when the results of the simulation are obtained [34]. It will be presented in the next chapter.
2. The Spacing ratio SR along y -axis at the walls must be less than 1.2, where $SR_y = \Delta y_{i+1} / \Delta y_i$ [34].

Both requirements are met in the medium mesh. An averaged value of $\overline{SR}_y = 1.1$ and a maximum value of $SR_y = 1.18$ are observed. The y^+ will be presented in the next chapter.

Turning to DDES, the two most important requirements are as follows:

1. $\Delta x, \Delta y, \Delta z < 5\% \times L$, where L is the longest length scale in the radial direction, namely $D_{out} = 150 \text{ mm}$ [34].
2. Aspect Ratio AR has to be less than 5 and ideally equal to 1 [34].

Again, both requirements are met, in particular with a value for the aspect ratio of 1.2. It is important to note that, as previously explained in section 2.3.2, these requirements are critical for DDES if we are able to correctly interpret the

unsteadiness and ensure a smooth transition from RANS to LES in the grid of the mesh.

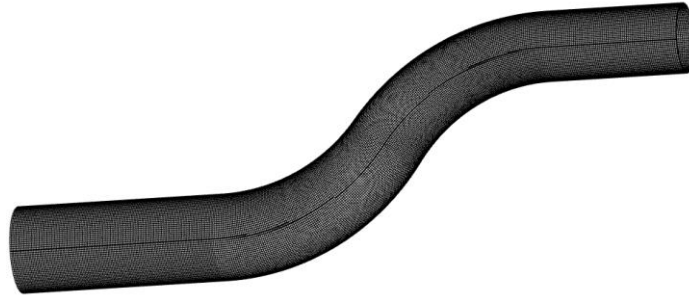


Figure 3-10 Mesh of the clean case (no fan simulator) made by A. Soli [12].

3.3 Simulations

After the presentation of the geometry and the structure of the mesh, in this section the most important aspects of the simulations are highlighted. Both RANS and DDES will be described in a similar manner, starting from the solver settings, moving to the boundary conditions and finally considering the convergence history.

3.3.1 RANS

3.3.1.1 Settings in RANS simulation

Starting from the medium mesh, the software used for the RANS simulation was ANSYS Fluent v17.1, which applies an Eulerian approach to the equations governing the flow field [38]. First of all, as already mentioned in section 2.3, for the RANS simulation, the SST $k-\omega$ method is used to solve the flow, together with the energy equation. The main reason is that it also resolves shear stresses because it is more reliable and accurate than other models such as Standard $k-\omega$ or $k-\epsilon$ [30]. Furthermore, it has a better description of the separated regions as evidenced in the literature but also in the extensive work done at Cranfield University in previous investigations of complex intakes. In order to produce a better description of the flow, low-Re correction, production limiter, viscous heating, curvature correction and compressibility effect are added to SST $k-\omega$. The first option allows better control of viscous damping, the

second decreases turbulence levels at stagnation points. Curvature correction makes the model insensitive to curvature of the streamlines inside the duct [37]. Finally, the flow inside the duct is considered as air and described using the ideal gas law together with the Sutherland law for viscosity. The solver used was pressure-based since it leads to a significant reduction in computational costs. Although a pressure-based solver is used for low-speed incompressible flow and a density-based solver for high-speed compressible flows, previous investigations and mentioned by Giacomobello [36], showed no appreciable changes in the results between the two solvers. Consequently, even if a choked flow is employed here in order to ensure faster convergence, the pressure-based method was used. Moreover, the most interesting results for the purposes of this project can be found before the throat at the blades region, where lower speeds can be observed.

A second important aspect of the settings is the solution method. A PISO velocity-pressure scheme is used because it offers higher precision than SIMPLE or SIMPLER, where no coupling between pressure and velocity is present [30]. Furthermore, the study of the gradients adopted a Green-Gauss Node Based method. Second order upwind was applied to all variables (Pressure, density, momentum, Turbulent Kinetic Energy, Energy and Specific Dissipation Rate) for spatial discretization in the simulation. Finally, a standard initialization from the inlet was chosen in order to start RANS.

It is important to stress that the settings used for this project were the same as those used by A. Soli [12] in his work. This is fundamental to ensure a reliable and accurate comparison. Due to the critical importance of the RANS simulation for the DDES (the transient simulation is started from the converged RANS data), A. Soli's simulation was launched again, starting from the settings of this work.

3.3.1.2 Boundary conditions

The structure of the boundary conditions is presented in Figure 3-11. In particular, as previously described in section 3.2.1, two interfaces are set where

the meshes are merged together. Moreover, a total pressure inlet profile and an outlet static pressure value are used for the extremities of the system.

Finally, the spinner, surface of the duct, blades and cylinder of the fan simulator are considered as walls. The inlet total pressure profile comes from experimental investigations carried out at Cranfield University using an S-duct without the fan simulator at the exit; it is the same profile used by A. Soli [12].

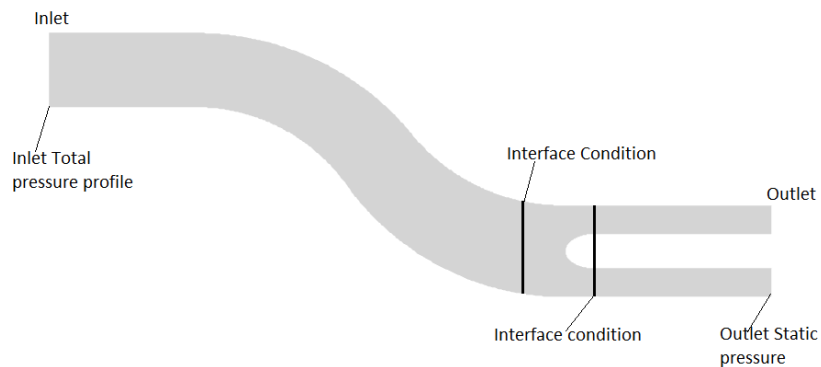


Figure 3-11 Boundary conditions for the control volume of the system.

The total pressure distribution at the inlet plane as a function of the radial position is described in Figure 3-12. The total temperature value adopted (290.46K) also came from experimental investigations. The value of static pressure used at the exit is imposed in order to choke the flow in the S-Duct exactly at the throat of the blade channel using the quasi-unidimensional theory for convergent-divergent ducts [36]. For this reason a value of 10500Pa is set. In reality this value is not used by the solver during calculations since in supersonic flows it is extrapolated from interior zones [38], i.e. it does not affect the solution.

In terms of turbulence, it was defined in both the inlet and outlet sections, with turbulence intensity and hydraulic diameter parameters. Turbulence intensity was set at 2% at the inlet as well as the outlet section. The value of hydraulic diameter at the inlet is equal to the inlet diameter (121.6 mm) and similarly for the outlet where the diameter is 150 mm.

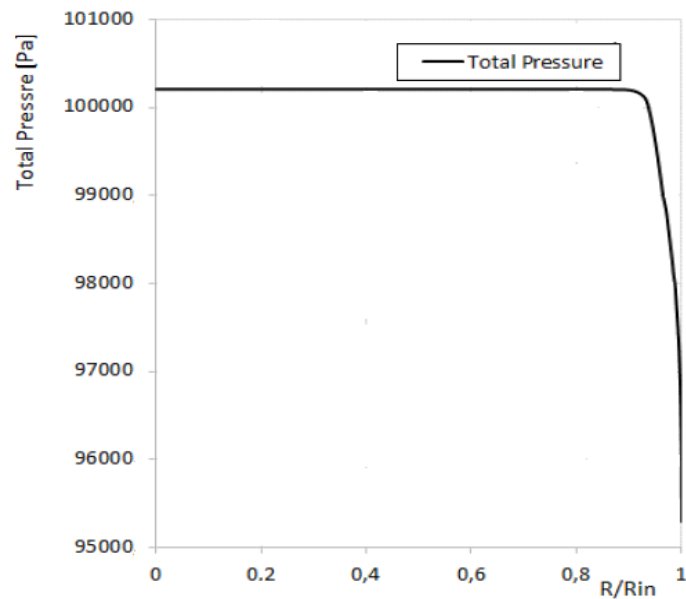


Figure 3-12 Inlet total pressure profile.

3.3.1.3 Convergence of RANS simulation

In order to check whether the results are consistent a convergence study is necessary. In particular, in Fluent it is possible not only to check the scaled residuals, but some of the most important variables inside the flow at different positions.

Figure 3-13, show that they became stable after around 20000 iterations. A total number of 40000 iterations was computed. All the residuals, with exception of continuity, reach a value of approximately 10^{-6} . Continuity has a higher value (about 10^{-4}), but very good stability is observable as well.

Even if residuals give a very good description of the behaviour of the solution, on their own they cannot be considered sufficient for the convergence analysis. For this reason, some checks on variables of the flow field are set. Throughout the simulation, mass flow, total pressure and Mach number at different positions are exported. Again, what the user is looking for in the checks set is high stability which means low oscillation. When this is reached, then convergence of the solution is obtained. It is important to note that convergence of the solution does not necessarily mean the solution is correct.

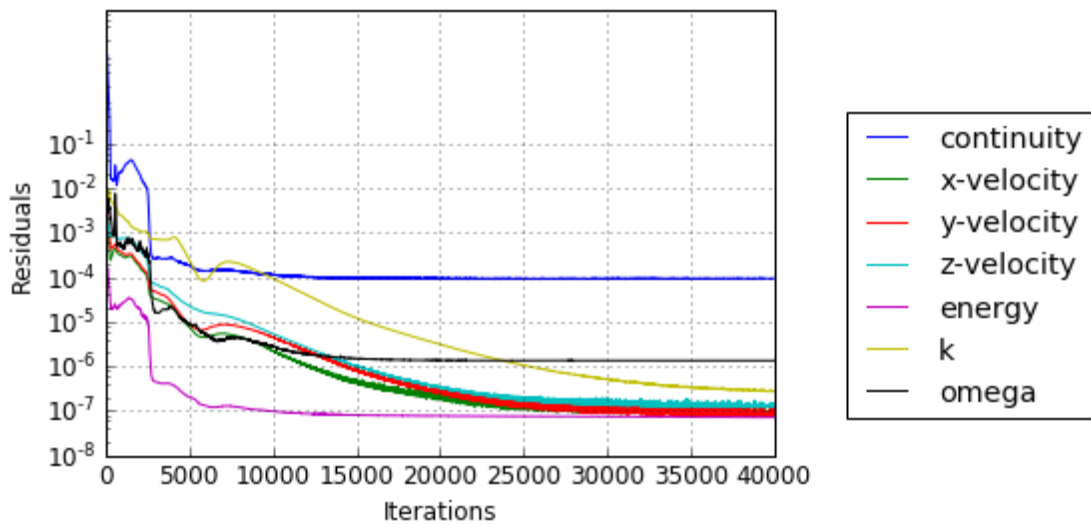


Figure 3-13 Residuals of RANS simulation

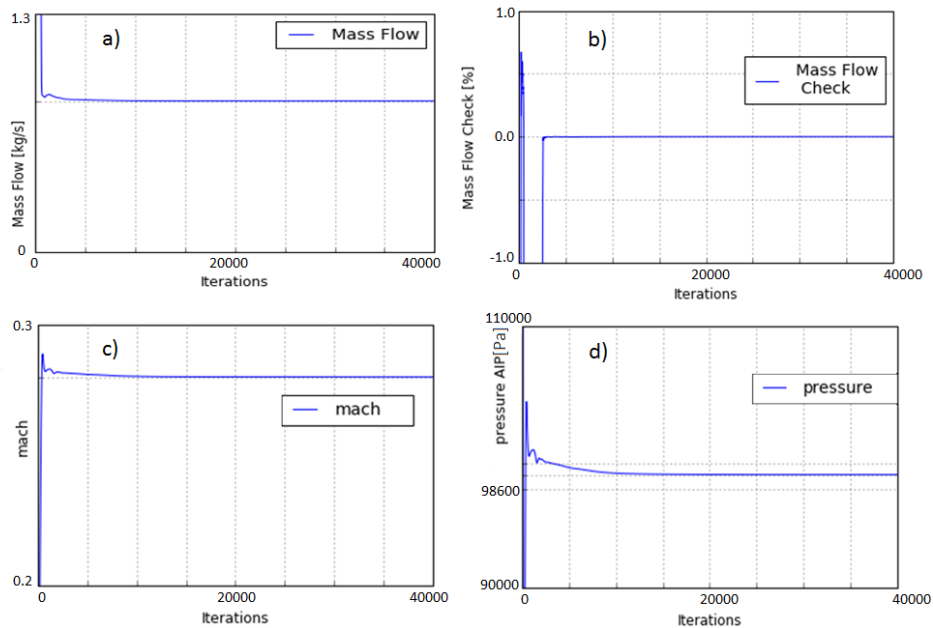


Figure 3-14 a) Mass flow at the inlet; b) Mass flow check; c) Inlet Mach number; d) Total pressure at the AIP plane; RANS simulation

Only experience and a detailed analysis of the results, perhaps including a comparison with experimental behaviour, can prove that the solution is also the correct one. Achieving convergence is, however, of paramount importance and this analysis is needed. Total pressure and Mach number are calculated with the area-weighted average approach, respectively at the inlet plane and at the AIP plane. Furthermore, mass flow, because of its dependence on different flow

properties, allows us to control convergence on the other variables and was chosen for this reason. It is calculated at the inlet plane. Similarly, mass flow check, namely the difference in mass flow between inlet and outlet as a percentage, is added. The checks on the variables are shown in Figure 3-14.

3.3.2 DDES

3.3.2.1 Settings and convergence

The settings and boundary conditions used for the transient simulation are the same as those adopted for the RANS. In particular, solver type, discretization scheme, gas model, turbulence model and all the other commands did not change. The most important difference during the set-up of a transient simulation is the introduction of a time step and of a convective time. A time step (Δt) is the incremental change in time where the equations are computed. A small time step leads to improved characterisation of the fluctuations in the flow field.

On the other hand, convective time (t_c) is defined as the ratio between the length of the S-Duct centreline without inlet and outlet sections (L_S) and the inlet axial velocity at the centre of the inlet plane (w_{ref}), namely $t_c = L_S/w_{ref}$ [30]. In practical terms, it is the time taken for the flow to go from the inlet to the outlet of the S-Duct. In this project $t_c = 7.843 \text{ ms}$ while $\Delta t = 1.2 \times 10^{-5} \text{ s}$, and so the non-dimensional time step is $\Delta t/t_c = 1.53 \times 10^{-3}$. The number of iterations for each time step was set at 15 in order to reach convergence within the available time without affecting the quality of the results. The transient simulation was initialized starting from the data of the converged RANS. The residuals can be observed in Figure 3-15, where the highest residual is continuity and it converges to a value of 10^{-3} .

The overall simulation was divided into three different batches where the new batch was started from the data of the previous simulation. The global time of the simulation was 55 convective times and the first 15 convective times were excluded, so only 40 were considered in the analysis. The reason is to ensure a smooth transition from RANS to DDES and so have the developed flow. The

general guidelines needed to recognize the change from “not developed” (RANS dominated region) to “developed” flow in a DDES simulation can be found in the work of D. Macmanus et al. [2] who suggested a more conservative approach in which 15 convective times were excluded, compared to the work of Berens et al. [39] where 10 were not considered. The more conservative approach is adopted in this project. The mass flow, Mach number and total pressure checks are presented in Figure 3-16.

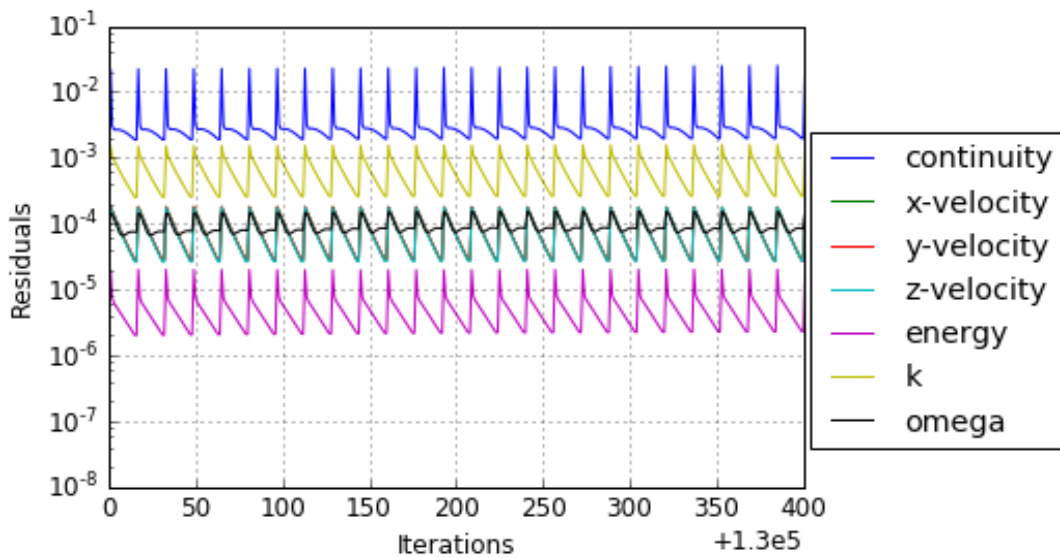


Figure 3-15 Residuals of the last 15 convective times simulation; zoomed section in order to see the behaviour of the scaled residuals.

Obviously, from a transient simulation some sort of oscillation is expected even at convergence. The behaviour is different from that observed in a steady simulation. However, some appreciations on assessments of the magnitude of the oscillations are presented in order to understand if they can be considered acceptable. Basically, fluctuation % represents a non-dimensional description of the magnitude of the oscillation in order to understand if it is a large or small value, compared to the averaged one.

Table 9 summarizes the studies conducted. The comparison was made with an averaged value of the DDES simulation for total pressure, mass flow and Mach number in the last 15 convective times.

Table 9 Oscillation levels compared to RANS converged value.

	Oscillation Magnitude	Fluctuation %
Total pressure [Pa]	± 225 Pa	0.23%
Mach number	± 0.0025	0.91%
Mass flow [kg/s]	± 0.0045 kg/s	0.36%

Looking, for example, at mass flow, the % fluctuation is calculated as follows:

$$\text{Mass flow fluctuation \%} = \dot{m}_{oscillation} / \dot{m}_{average}$$

where $\dot{m}_{oscillation}$ in the case considered is ± 0.0045 kg/s. Consequently, it can be seen that small oscillations are reached after 55 convective times.

3.4 Post-processing

3.4.1 RANS

The analysis of the results from the RANS simulation was carried out mainly with two tools. First, the data were exported from Fluent to Tecplot360 for the visualization of the streamlines and contours of the different variables. In order to fully understand the development of the flow, and thanks to the lower computational costs and size of the data from a steady rather than a transient simulation, different planes were analysed. As already mentioned, the most important is the AIP, but at the same time Plane O, Plane 1, plane 3 and plane 4 are also presented. The non-dimensional positions are summarized in Table 3. A larger number of planes was considered in the RANS in order to allow the reader to more completely understand the flow distribution in terms of averaged field inside the S-duct and in particular in proximity to the AIP.

Fewer contours will be presented for the DDES focusing the attention on the most important one, the AIP. Furthermore, the results along the symmetry plane, i.e. a perpendicular section in the Y-Z plane, were also studied.

Finally, the evaluation of pressure recovery, distortion descriptors and swirl descriptors as defined by SAE report ARP 1419 [19] -1420 [18] and AIR 5686

[11], was accomplished using a code developed by Cranfield University in Python™, called CUDatapro 3.6.

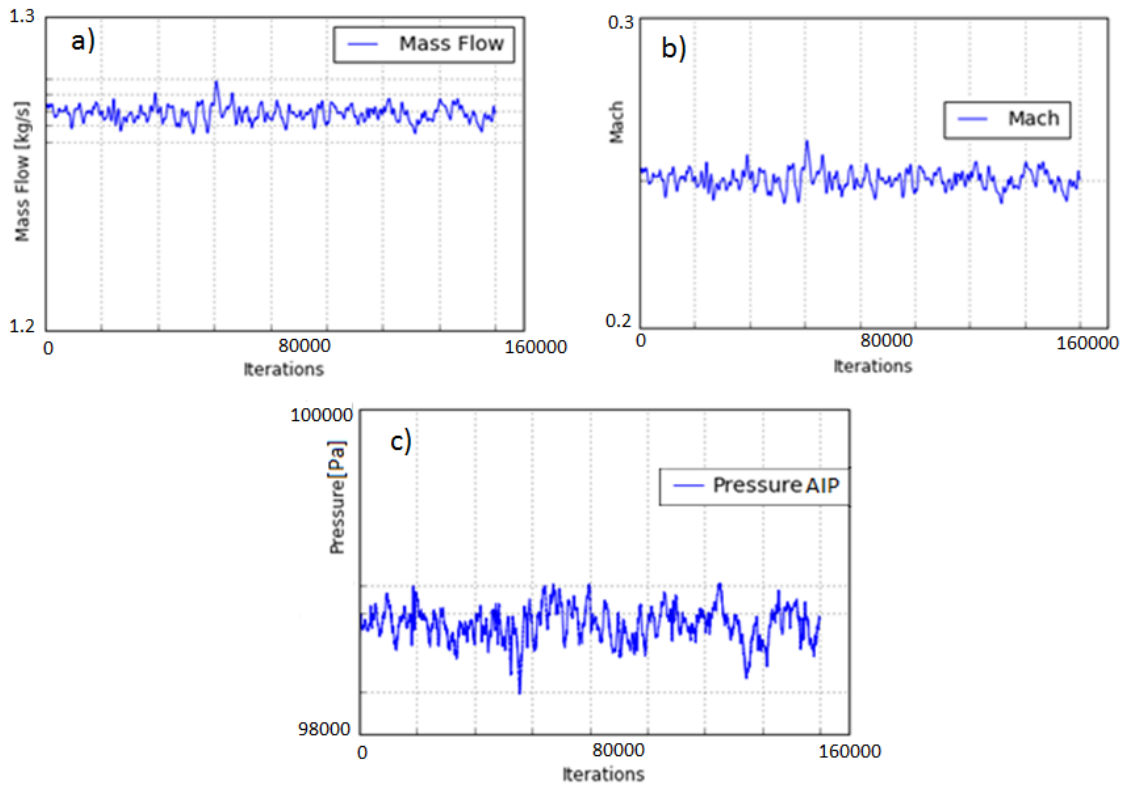


Figure 3-16 a) Mass flow at the inlet; b) Inlet Mach number; c) Total pressure at the AIP plane

3.4.2 DDES

The first study of the DDES was similar to the RANS case but on account of the transient behaviour, a more complex analysis and study of the results was needed. Firstly, during the simulation the data along specific planes were exported into Tecplot360. At the end of the simulation, using a code developed in Python™, the data for the last 40 convective times saved every 3 time-steps (the first 15 convective times are excluded) were averaged. Contours of the flow variables at AIP and symmetry plane are shown in the next chapter. Following a similar approach to the RANS case, using CUDatapro 3.6, swirl descriptors and total pressure descriptors are calculated by processing all the exported data at each plane. Finally, a comparison with both RANS and A. Soli's clean case [12] was accomplished.

Using data from the walls, the separation position and the size of the separated region were calculated using a code written in Python™. Skin friction lines and static pressure distribution were used to quantify the separation, following the approach described in section 2.2. A comparison of the result obtained with the case without the fan simulator and RANS simulation was applied.

The DDES data at the AIP plane will be introduced in the MATLAB code developed by Jovanović et al. [49], that is implementing the Dynamic Mode Decomposition, and partially modified for the purposes of this work, in order to test it. It will better presented in Chapter 5.

4 RESULTS

4.1 Sensitivity analysis

A very important step in a CFD simulation is to analyse the influence of the number of nodes, i.e. the grid refinement, on the results obtained so as to ensure that the chosen total number of nodes provide a reliable result [51]. In particular, this analysis aims to highlight how far the solution is from the asymptotical value. For this reason, the three meshes described above were used to conduct this study in the RANS simulation. Before describing the process adopted, some definitions are presented.

The first definition (eq. (4-1)) is the ratio of the grid refinement for the coarse medium and fine meshes [40]:

$$r = \frac{N_{g2}}{N_{g1}} \quad (4-1)$$

where N defines the number of nodes of the mesh and the subscript “g1” or “g2” indicates the grid in question. Furthermore, for a specific variable used for the assessment of the independence C , the order of convergence p presented in eq. (4-2), is [40]:

$$p = \frac{\ln\left(\frac{C_{g3} - C_{g2}}{C_{g2} - C_{g1}}\right)}{\ln(r)} \quad (4-2)$$

Starting from eq. (4-1) and eq. (4-2) it is possible now to define the Grid Convergence Index (GCI) in the two following forms (eq. (4-3) and eq. (4-4)) [40]:

$$GCI_{12} = \frac{FS \left| \frac{C_{g1} - C_{g2}}{C_{g1}} \right|}{r^p - 1} \quad (4-3)$$

$$GCI_{23} = \frac{FS \left| \frac{C_{g2} - C_{g3}}{C_{g2}} \right|}{r^p - 1} \quad (4-4)$$

where FS is a safety factor, usually equal to 1.25 when three or more grids are used [40]. The CGI is a measure of the percentage the computed value is away from the asymptotic numerical value. Basically, it shows an error band on how far the solution is from the asymptotic value [41]. A small value of GCI is required since it indicates the solution is in the asymptotic range. In order to understand if it is small enough to fall within the asymptotic region of the residuals, a new parameter AR is introduced [40]:

$$AR = \frac{C_{g23}}{C_{g12}r^p} = 1 \quad (4-5)$$

As presented in section 3.2, the three meshes (coarse, medium and fine) have the following total number of nodes respectively: 5.51×10^6 , 6×10^6 and 9.45×10^6 . In the sensitivity analysis applied the parameters considered are three: Pressure recovery, CDI and DC60 which are reported in Table 10.

Table 10 Parameters of the sensitivity analysis

	Coarse	Medium	Fine	GCI_{12}	GCI_{23}	AR
PR	0.9902	0.9912	0.9913	-0.00090	-2.01×10^{-5}	0.9981
CDI	0.01342	0.01309	0.01305	-0.05111	-0.003918	1.0012
DC60	0.1980	0.1977	0.1971	0.01891	0.02890	1.0005

As we can see from Table 10 the differences between the GCI of the medium and fine meshes are very small if compared to the changes between the medium and the coarse grid. There is one order of difference between GCI_{23} (medium-fine GCI) and GCI_{12} (coarse-medium GCI). Furthermore, the difference between the values of the parameters chosen (PR, CDI, DC60) is much smaller between medium and fine mesh than it is between the coarse and medium grid. Consequently, if we increase the number of nodes, the asymptotical region is reached and there is little difference in the results between the medium and the fine mesh.

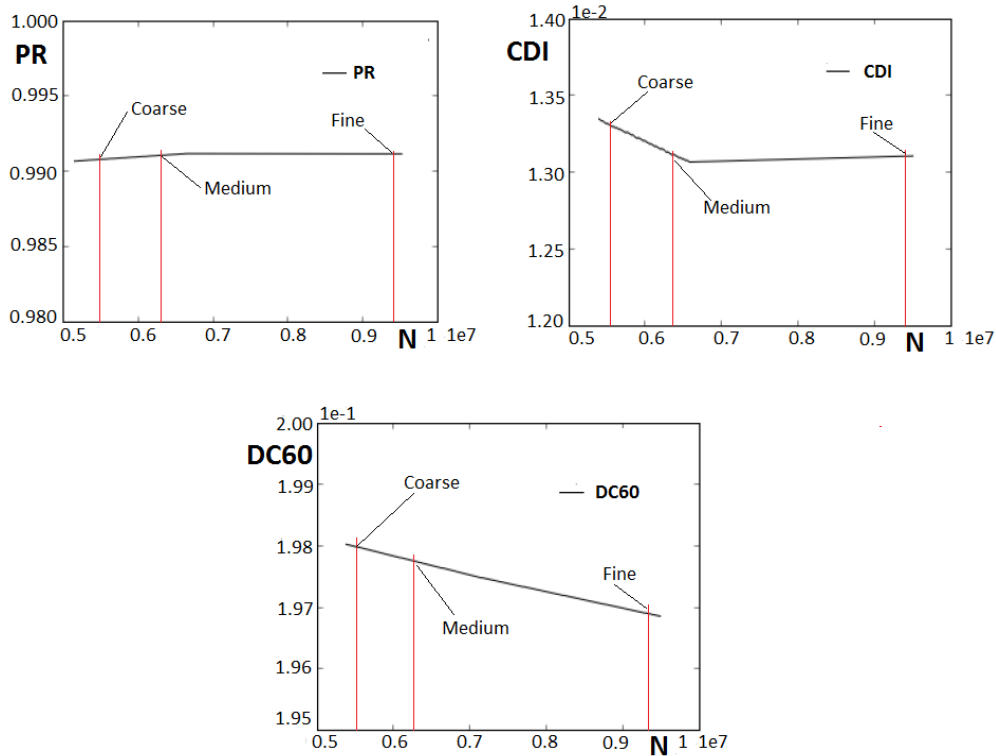


Figure 4-1 Graphical representation of the change in the descriptors on increasing the number of nodes (N).

The same concept is presented in Figure 4-1. In the end, the medium mesh was chosen. Although it did not fall exactly in the constant region of the diagram (looking in particular at PR and CDI), this choice was made because of the shorter computational time, especially for the DDES simulation. A small decrease in the number of nodes can lead to a large decrease in computational time. Moreover, it should also be borne in mind that one of the objectives of this work is to compare the data with data for the case without fan simulator and consequently, as previously described in section 3.2.2, two similar meshes are required. Looking at Table 10, the medium mesh is considered to be a good compromise between computational cost and quality of the solution. What's more, this mesh is similar to the one used in A. Soli's work [12].

4.2 Resolution of the Boundary Layer: Y^+

In this section we take a final look at mesh quality, continuing the description started in section 3.2.2. In particular, one important requirement for both RANS

and DDES has to be met: a value of y^+ smaller than 1 at the walls in order to correctly describe the boundary layer [34]. The only way to check the y^+ is to run the simulation first and then check the distribution along the wall. If the requirement is not met, then an improvement in the mesh itself is required. As a consequence, the height of the first cell at the wall will be changed accordingly until a value of 1 is reached. This is the normal procedure in these cases and has therefore also been followed in this project. Furthermore, the resolution of the boundary layer is of paramount importance because it determines the equations for k and ω used by the solver during the simulation to describe small scale turbulent events [30].

Figure 4-2 and Figure 4-4 show that a value of $y^+ < 1$ is achieved in all the regions except for small portions on the blades and the struts. However, a maximum value of 1.2 is observed, which is still within the limits of the k - ω equations used by the solver [38]. Moreover, the most important region for the calculations, in other words the whole area before the leading edge of the blades, is perfectly described by the mesh and very good values of y^+ can be seen in Figure 4-3.

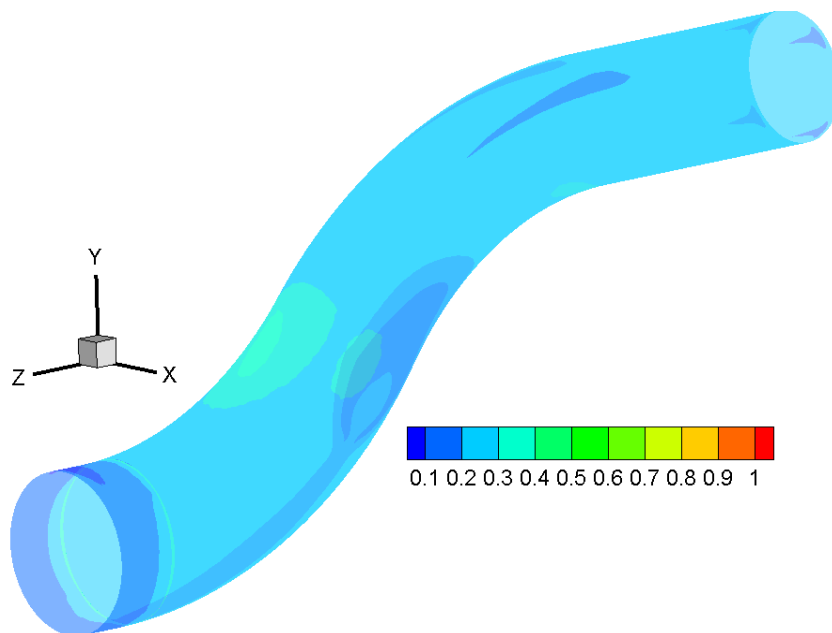


Figure 4-2 y^+ along the walls of the S-duct; from inlet to the AIP.

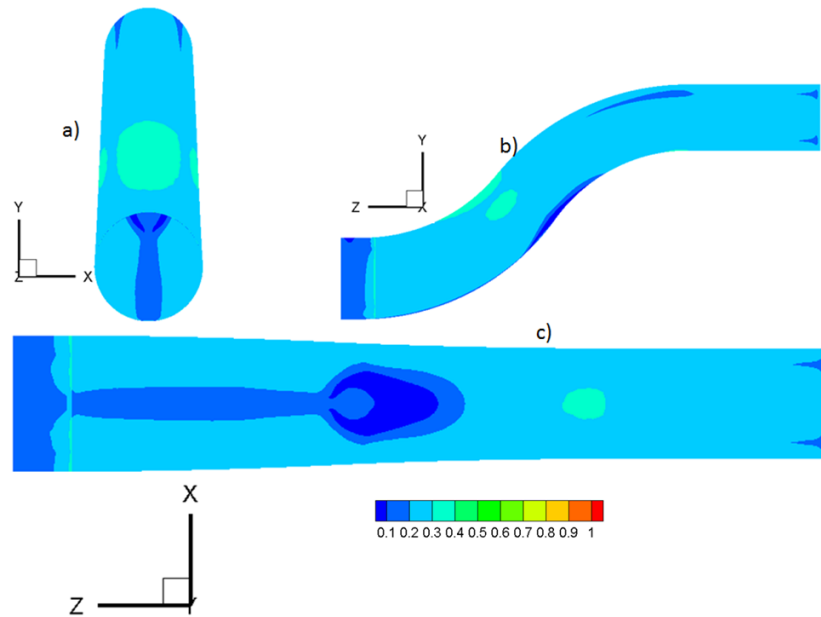


Figure 4-3 2D view on three sides of the S-duct; from inlet to AIP.

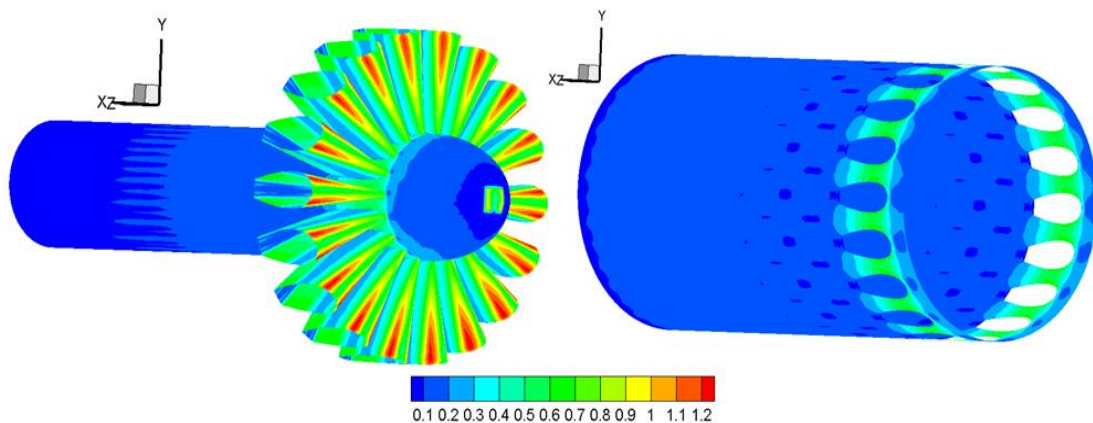


Figure 4-4 Y^+ in the fan simulator.

4.3 Flow field Characteristic

In this chapter the contours of the main variables will be presented for both the RANS and time-averaged DDES simulation. Finally a comparison between the two and the results of the case without fan simulator will be made. Different planes will be described for the RANS method in order to understand the flow field. As far as DDES is concerned, the study will be localized at the AIP.

4.3.1 RANS

In this section the flow development is presented from the contours of the RANS simulation. A first description of the flow field will be made at different planes in order to understand how the averaged flow evolves as it approaches the AIP. Plane M, Plane 1, Plane 3, Plane 4 and AIP are the perpendicular sections considered. The plane positions are described in section 3.1. The presence of the fan simulator does not affect the flow in the upper part of the S-duct (at the first bend and also around the second bend) and the flow distribution is the same as in the case without static fan. Since many studies were applied at Cranfield University at these positions, in this work no contours in the up-stream region are shown. However, the symmetry plane (the section along the Y-Z plane) provides a good description of the overall flow in the duct. It is important to note that on getting nearer to the AIP, also the leading edge of the blades is approaching. In particular the non-dimensional relative distance between the AIP and the leading edge is $0.049D_{out}$ (remember that $D_{out} = D_{AIP}$). The presence of the blades start to be felt at the AIP position creating small oscillations and noise in the contours. The same was observed in the previous work on a similar geometry by A. Giacomobello [36].

In Figure 4-5 in terms of Mach number in the symmetry plane and in Figure 4-6 in terms of the w-component of velocity, some important features of the flow field can be observed. In particular, as already mentioned in Chapter 3, the geometry of the fan is designed in order to choke the flow at the throat. This can be seen in the increase in the Mach number at sonic conditions, precisely at the throat. Furthermore, the inlet Mach number of about 0.27 tends to increase at the inner wall region and decrease at the outer wall region on approaching the first bend. The first bend causes an increase in static pressure at the outer wall and a consequent decrease in velocity in order to counterbalance the centrifugal force. The opposite happens on the inner wall, where the pressure tends to decrease and the velocity increase. As will be better described in the next section, separation appears at the first bend. At the second bend, the larger curvature of the duct causes a considerable increase in static pressure at the inner region, with a correspondent decrease in velocity.

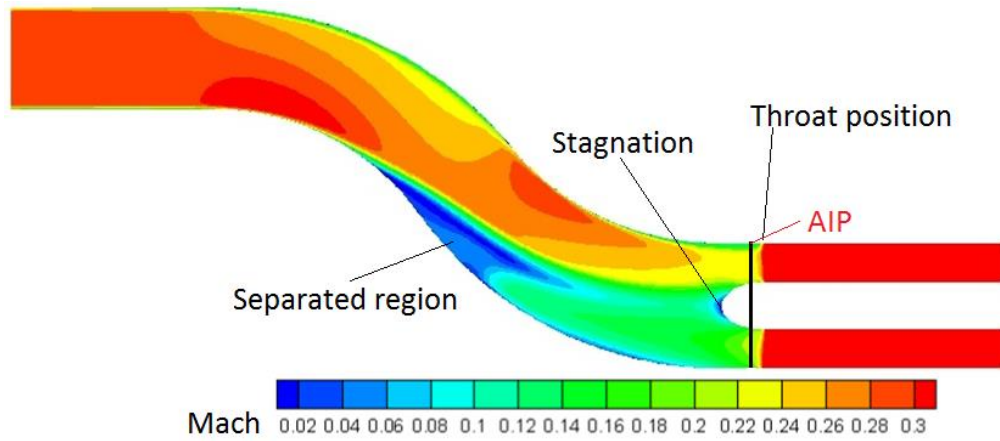


Figure 4-5 Mach distribution along the symmetry plane; RANS simulation.

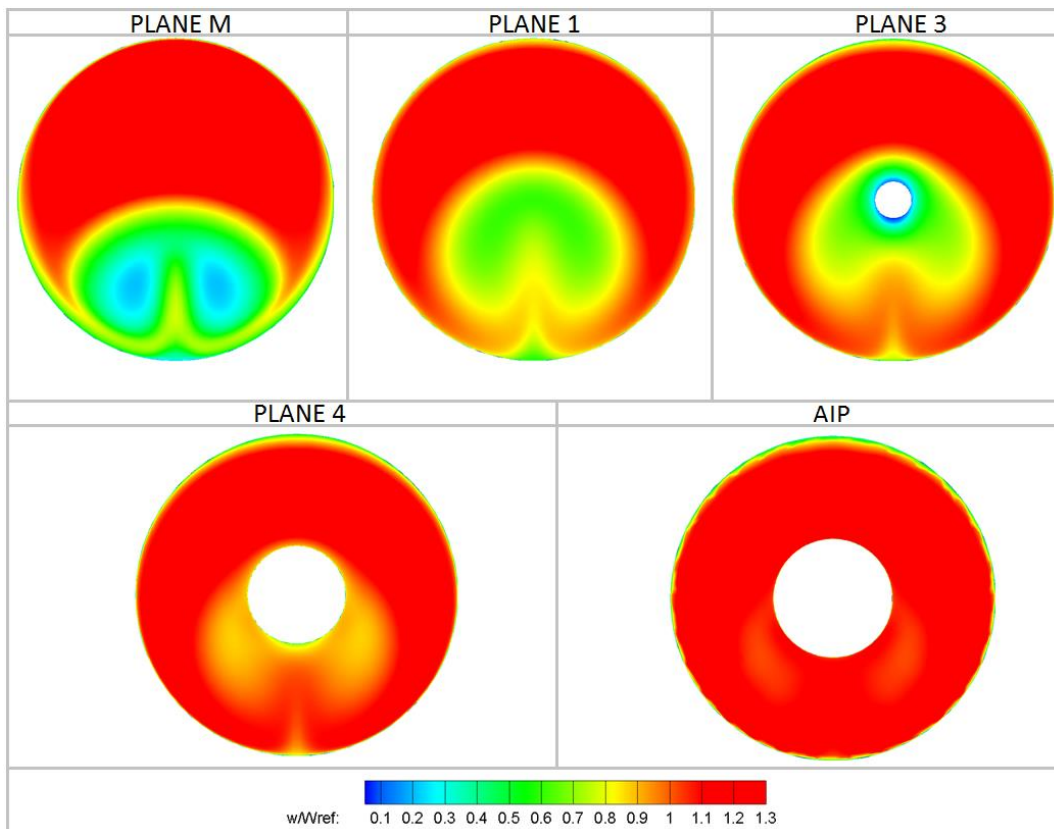


Figure 4-6 w-component of velocity at different planes; RANS simulation.

The separated flow is still present, but then reattaches downstream. At this position (second bend), the opposite happens at the outer region, where the velocity tends to increase again. Consequently, two vortices, which tend to move downstream, are formed. This can be seen in Figure 4-6 where two regions of lower axial velocity are transported downstream. However, the size of

the core regions with lower velocity, tends to increase as we move from plane M to the AIP. A mixing of the core with the main flow is present. In addition it is important to remember that the blades are choked and consequently the velocity will increase to a value of sonic Mach at the throat. The action of the spinner tends to modify the shape of the two vortices and redistribute the flow due to the decrease in area dictated by the presence of an obstacle.

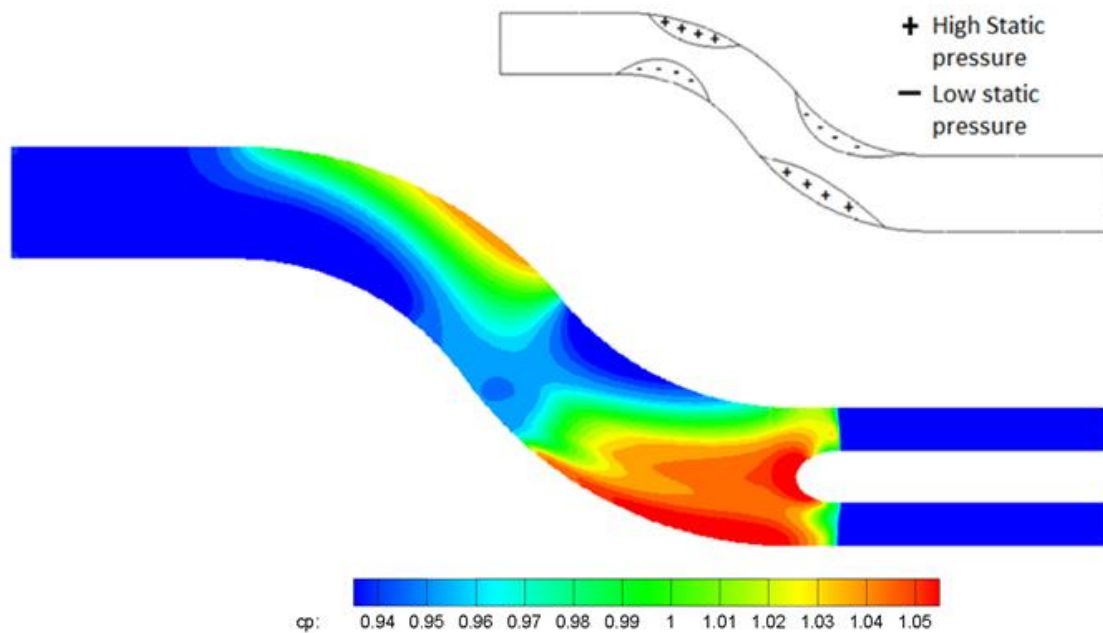


Figure 4-7 Static pressure coefficient distribution along the symmetry plane; RANS simulation.

A region of stagnation can be observed at the tip of the spinner. The pressure distribution analysed previously can be observed in Figure 4-7 where it is described with the non-dimensional parameter pressure coefficient. If we look at the velocity in greater detail, we can understand the behaviour of the flow better. Starting with the u-component in Figure 4-8, the mechanism of formation of the vortices is well described. The action of the first bend on u-velocity in the upstream planes, which are not considered in this work, is not relevant [12], but the action of the second bend, towing to the large static pressure increase in the lower region, forces the low momentum flow in the boundary layer to move towards a region with lower static pressure, thereby producing vortices [11]. Even if it starts even further upstream, this can be observed in Plane M (and all

the following planes) in Figure 4-8, where the lower part of the section (-90° , see Figure 2-23b for a better understanding of the polar nomenclature) present regions of maximum absolute magnitude of u-velocity. Moving from plane M towards the AIP the dimensions of these two regions tend to increase. As it approaches the AIP, the flow is affected by the presence of the spinner which tends to deflect it.

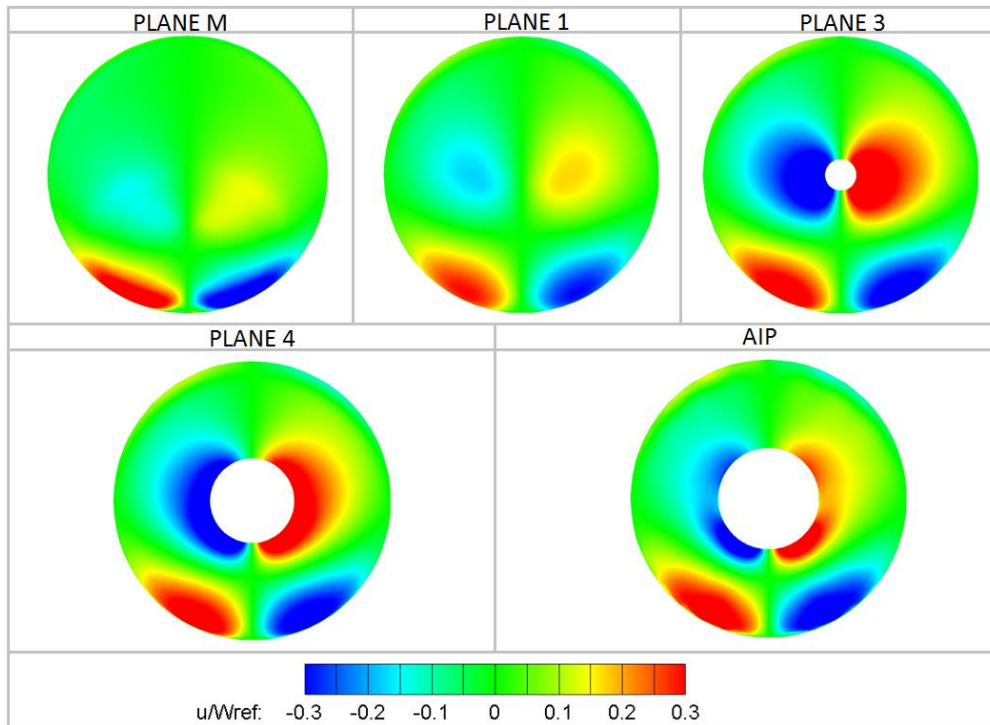


Figure 4-8 u-component of velocity at different planes; RANS simulation.

For this reason, another two regions with high values of u-velocity are observed around the spinner wall. They spread, due to diffusion, as they approach the AIP. In Figure 4-9 the v-velocity is presented. As described in previous works, in the upstream region where the spinner exerts no influence, the flow in the central region tends to move upwards due to the centrifugal force [12]. The separation, as observed, appears in the lower region (-90°) between the first and the second bend. Moving downstream the development of the two vortices continues and this process can also be observed in this work, from plane M to the AIP. The general decrease in the magnitude of the v-velocity results from the diffusing process occurring in the S-duct. However, the deflection of the velocity due to the presence of the spinner is clear as the flow approaches

Plane 3, and this is similar to what was observed for the u-component, namely a reshaping of the vortices.

Total pressure, described by the non-dimensional parameter pressure recovery defined in section 2.1.1, it is presented in Figure 4-10 again only in the downstream region (from plane M). In the upstream region, the drop in total pressure from the upper side (+90°) to the lower side (-90°) of the plane tends to increase in particular where the separation bubble is observed [12]. Consequently a region of lower total pressure at the inner side is present. However, moving to the downstream region of the duct, this change in total pressure from the outer (+90°) to the inner (-90°) wall is reduced [12]. This behaviour is also observed when moving from plane M to the AIP, where there is an observable increase in total pressure values as well as an expansion of the affected region because of the diffusing process occurring in the duct. The behaviour described in Figure 4-10 is very similar to the description provided for the axial velocity. The influence of the spinner is evident from plane 3 where in particular the deflection of the flow due to the presence of an obstacle, also reflects on the total pressure distribution. The regions at lower total pressure tend to turn around the wall, reshaping. Finally, if we look not only at Figure 4-10 but also at Figure 4-6 and Figure 4-5, there is evidence of a much smaller second separation at the outer wall (+90°). On the symmetry plane there is a region with a lower Mach number and as we move from Plane 1 to the AIP, on the outer wall (+90°) a smaller region with lower total pressure is spreading. The dimension of this separated flow is smaller due to the presence of the first larger separated region which constrains the static pressure gradient of the upper wall of the S-duct.

The figures presented in this section reveal a first limitation of the RANS method: the transition between different regions is represented in sudden steps rather than smoothly. This clearly does not describe the real physics of the flow field. As will be clearer later, time-averaged DDES partially overcomes this and shows a smoother transition from one region to the next.

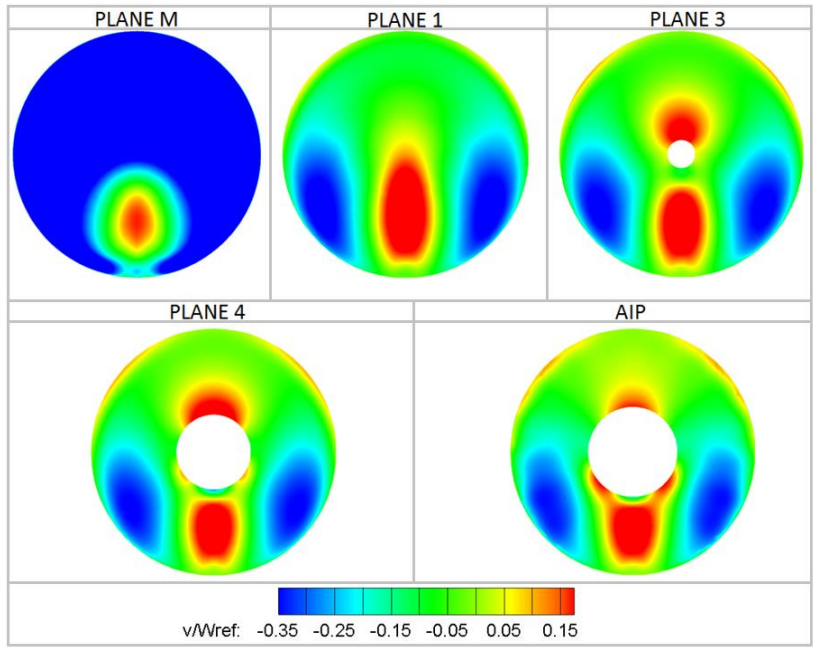


Figure 4-9 v-component of velocity at different planes; RANS simulation.

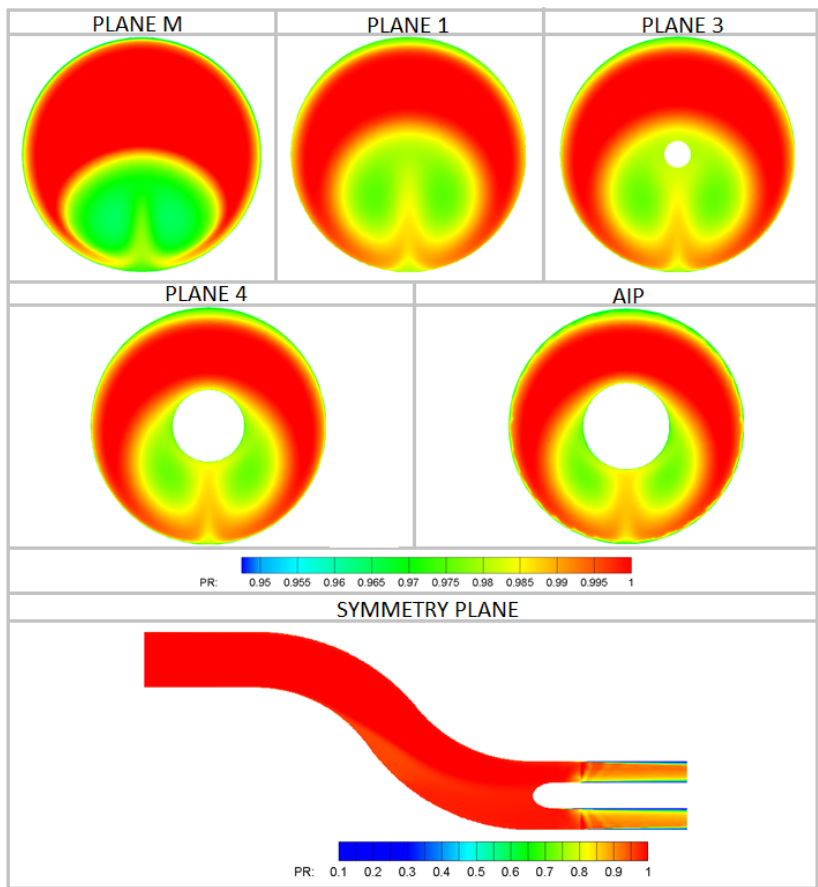


Figure 4-10 Pressure recovery coefficient at different planes and along the symmetry plane; RANS simulation.

4.3.2 DDES

Figure 4-11 where DDES data at the AIP section are present, reveals a similar flow structure compared to Figure 4-8. However, an important feature common to all the following figures is they all show a smoother transition from maximum to minimum value and a more realistic flow field. In particular, the contours presented are time-averaged DDES, where, starting from the transient data at each time-step, the time-averaged result is obtained using the code, called CUdatapro, written in Python by Cranfield University. The action of the spinner on the flow is clear from Figure 4-11.

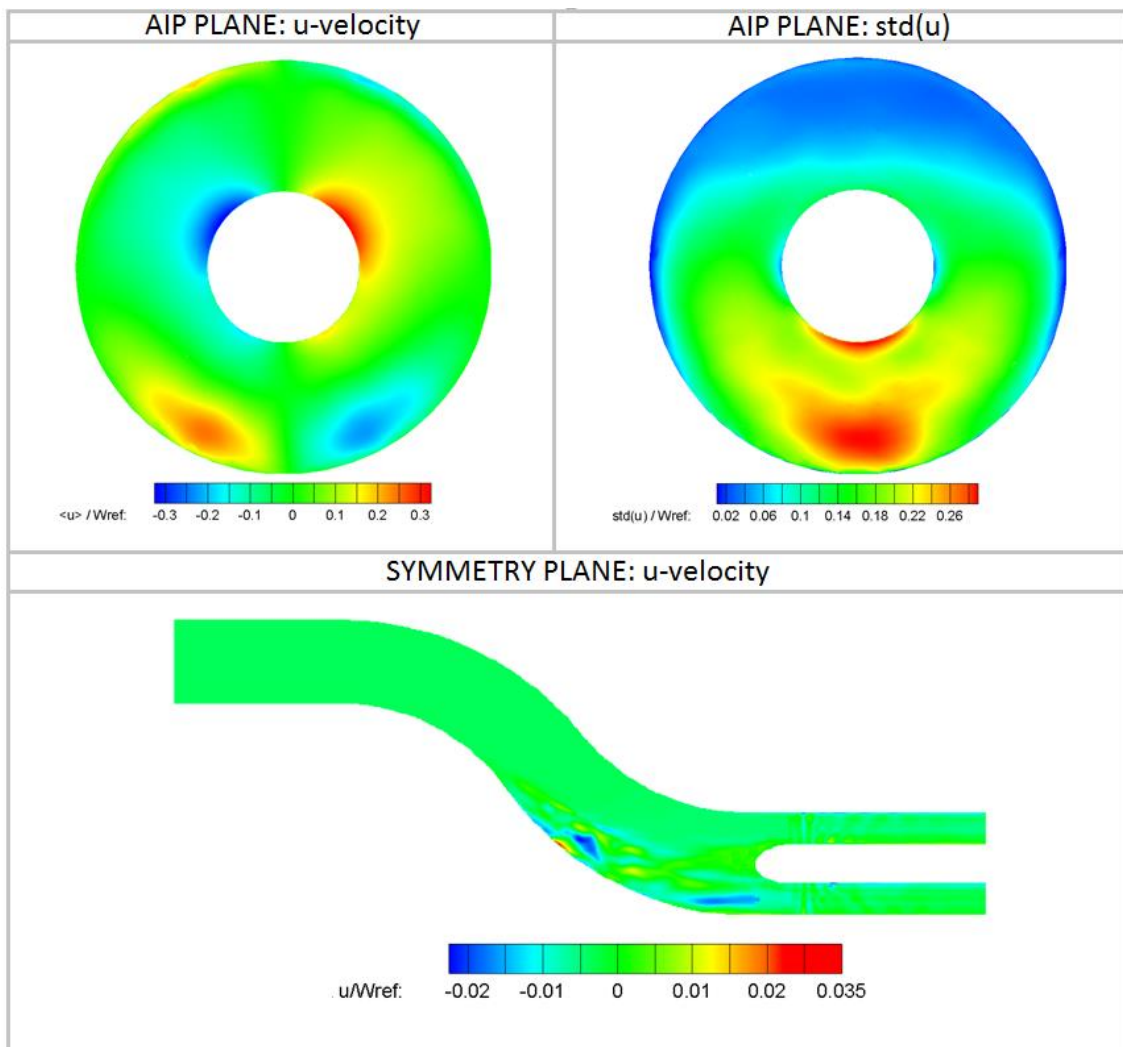


Figure 4-11 u-velocity at the AIP plane and along the symmetry plane; time-averaged DDES simulation.

On contact with the wall the flow is deflected by the obstacle. Moreover, the symmetry plane shows a u-velocity value close to zero. The reason is that the nature of the vortices generated in that section of the duct have an almost symmetrical structure and so a section along the Y-Z plane shows such behaviour. Figure 4-12 shows v-velocity from a time-averaged DDES revealing the typical structure described in section 4.3.1. Due to the diffusing process, lower values of v-velocity are observed at the AIP compared to the rest of the duct. The presence of the spinner causes the vortices to change shape.

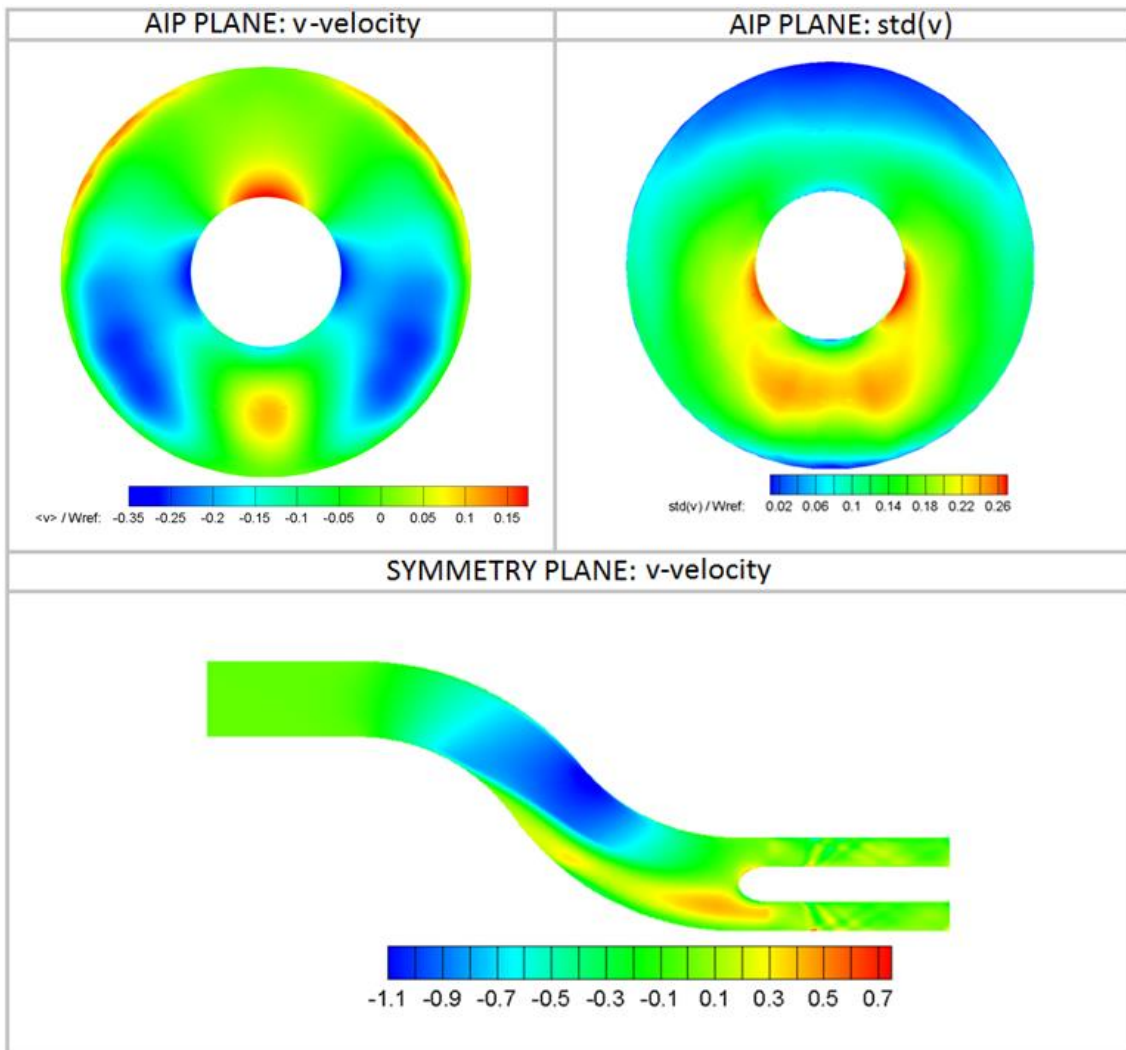


Figure 4-12 v-velocity at the AIP plane and along the symmetry plane; time-averaged DDES simulation.

Along the symmetry plane, negative values of velocity are observed in the upper part of the duct, at the first and second bend while positive values of v-

velocity are seen in the separated region, along the inner wall of the duct. Finally, Figure 4-13 describes the distribution of w -velocity along the AIP and symmetry plane. There is a second region of separation at the outer wall ($+90^\circ$). However, it is much smaller in extent than the core separated region.

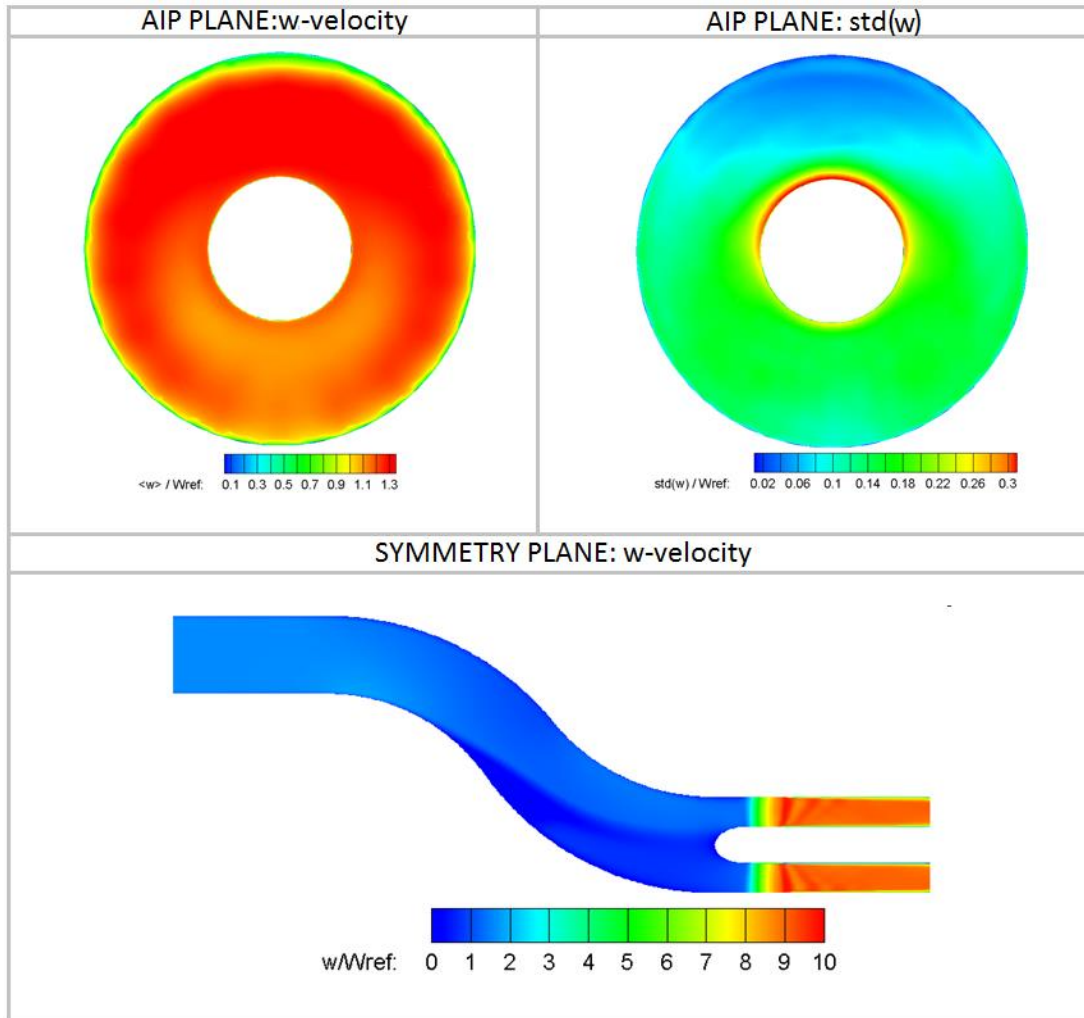


Figure 4-13 w -velocity at the AIP plane and along the symmetry plane; time-averaged DDES simulation.

The spinner causes the flow to change shape, and this is also reflected in the axial velocity. Although a more detailed comparison between RANS and DDES will be carried out in the next section, compared to the results of the RANS simulation, DDES reveals different distribution of the flow in both magnitude and shape below the spinner. Moreover, in the symmetry plane it can be seen that the flow is choked after the throat in the fan simulator region. There are lower

velocity values at the inner wall (separated region). Again at the outer wall a smaller region with a decrease in axial velocity is observed. As already mentioned, the first bend causes an increase in static pressure at the outer wall and a consequent decrease in velocity in order to counterbalance the centrifugal force. Finally, a decrease in velocity is also present downstream, close to the AIP section, where the second separation starts.

4.3.3 Comparison of RANS and DDES

During the analysis of the time averaged DDES and RANS results some differences in the contours were noticed. For this reason, in this paragraph a comparison in terms of PR at the AIP section is accomplished.

A common characteristic of RANS simulations, also observable in Figure 4-14, is the sudden transition from regions of high total pressure to regions of lower total pressure. This behaviour cannot be considered representative of the physics of the phenomenon. In the DDES instead, a smooth transition from minimum to maximum values is present. Furthermore, the core region under the spinner presents higher values of pressure recovery coefficient in the DDES compared to the RANS simulation. The shape of the core region is different in the two cases. In particular a symmetrical distribution of PR is observed in RANS while a more uniform characterizes the AIP in the DDES. In the transient simulation each time step contains the unsteadiness of the flow field and starting from that information, using the code in Python previously mentioned, the averaging of the flow field is accomplished. As a consequence the final shape is determined from all the previous time steps. This leads to a more generic shape that is not equal to the symmetric structure observed in the RANS. In addition, looking at the outer wall (+90°), it seems that DDES is capable to better capture the second region of separation at the AIP, while RANS simulation is underestimating its dimensions. Same range of values are observed.

This brief comparison underlines the limitations of a steady calculation to properly describe the flow. A better understanding of the differences will be provided in the next sections, during the analysis of the descriptors. However, in

many situations a steady calculation can be considered enough for the purposes of a work and this may happen also in the industry sector during design stage. Even if a transient calculation can provide better and more reliable results for design purposes, the time needed to complete the process is quite high and not always justifiable. For instance, the RANS calculation here presented took around 24 hours, while the DDES around 500 hours. The difference is evident.

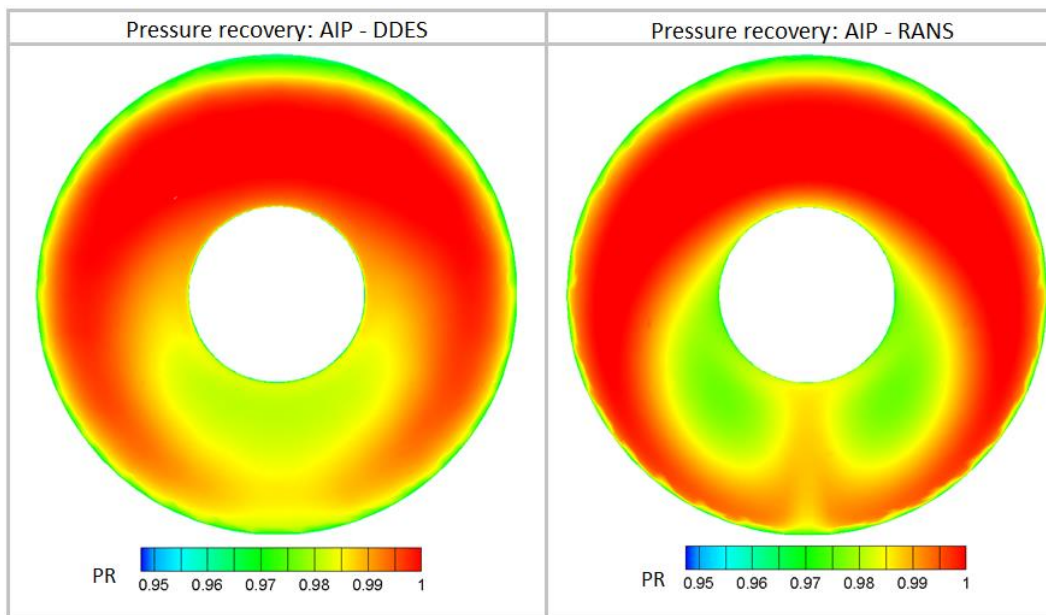


Figure 4-14 Comparison of PR between time averaged DDES and RANS at the AIP.

4.4 Separation

In this section the position and the behaviour of the separation is analysed. In particular in Figure 4-15, the static pressure along the top and bottom line along the duct from $z/L=0$ (after the initial cylinder) to the AIP, is presented.

Due to the presence of the first bend, along the first part of the upper wall, namely looking at the top line, the static pressure tends to increase. This is observed in Figure 4-15 from $z/L=0$ to $z/L=0.5$. Subsequently a sudden drop in static pressure is observed ($0.5 < z/L < 0.6$), probably a combined effect of both expansion and volumetric increase of the separated region. Consequently, at this position in the upper line a strong negative pressure gradient and higher

velocities are present. This is also observed in Figure 4-13 along the symmetry plane. However, approaching the AIP static pressure tends to increase again reaching a constant value. This highlights the presence of a second smaller region of separation at the upper part of the duct, approaching the AIP. This was previously discussed and showed in Figure 4-14. On the lower wall (bottom line), the pressure increases due to the diffusion happening in the duct. When separation is reached, the static pressure remains constant at $z/L=0.3$ and so a plateau is observed. After reattachment ($z/L=0.5$), static pressure increases again.

Finally, the standard deviation shows how the highest fluctuations in static pressure are distributed in the region of separation. An increase approaching the AIP is observed also on the top line, suggesting again the presence of a second smaller region of separation.

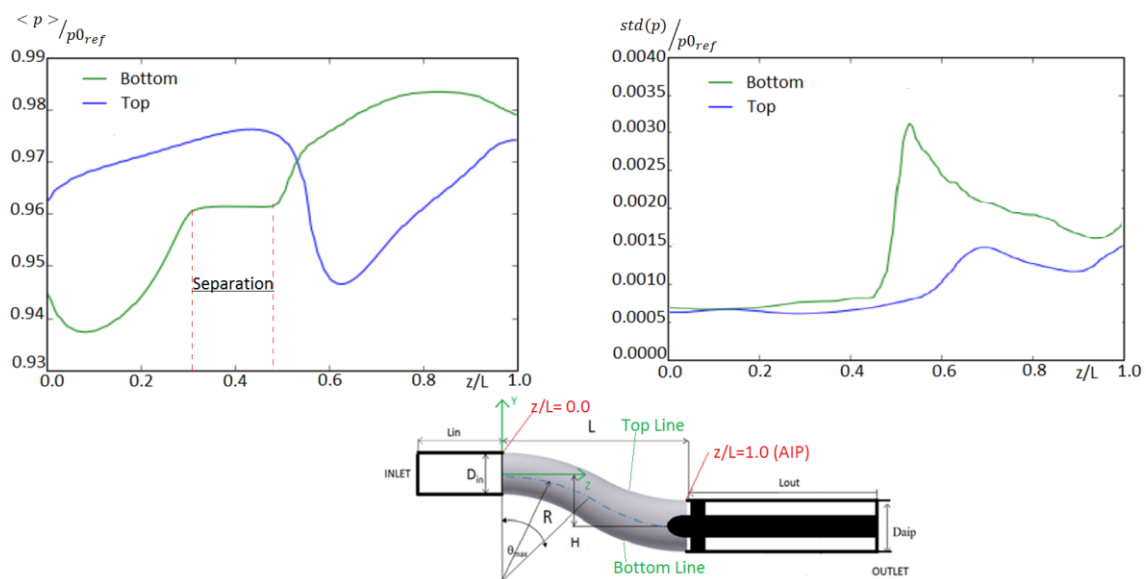


Figure 4-15 Static pressure distribution along the wall and standard deviation.

In Figure 4-16, time-averaged shear stress lines at the wall are presented. It is important to underline the presence of two regions with higher values of shear stress at the inner side of the first bend and the outer side of the second bend. Along the lower wall instead, a large drop in shear stress is observed. In this region separation takes place. This is also presented in a zoomed section of the inner wall in Figure 4-17 a). As described by J. Délerly [28] and presented in

Appendix A, from the values of shear stress it is possible to calculate skin friction lines. The structure and shape of the skin friction lines give an indication on the behaviour of the 3D separated boundary layer and from that the position of the separation and reattachment point can be derived [28].

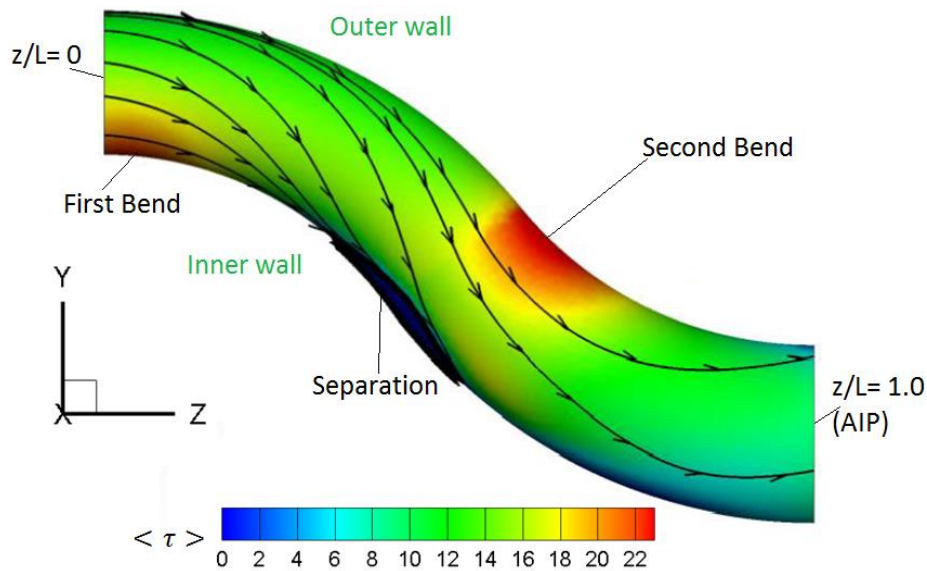


Figure 4-16 Time averaged shear stress; general distribution of the shear stress along the wall of the S-duct.

From Figure 4-17, it is possible to note the similarity between the pattern obtained in this work and the one documented by Wellborn [42]. At the first saddle point separation starts. At the second saddle point reattachment is observed and the bifurcating structure evolves downstream. In addition, in the “owl face” pattern the spiral nodes observed are indicating the position where the two streamwise vortices are connected to the wall [28].

Using a code written in Python, a similar approach to the one briefly described in Appendix A was implemented in order to detect the position and dimension of the separation. In particular, the first saddle point, namely the separation point, is calculated from the DDES simulation to be at $z/D_{AIP} = 1.3$ while the reattachment at $z/D_{AIP} = 2.3$. Furthermore, the dimension of the separated region is calculated as the Euclidean distance between the two saddle points. Consequently, the value of the dimension of separation, obtained from the DDES analysis, is $1.696D_{AIP}$. These values are in good agreement with the

results obtained by Garnier et al. [43] in the experimental work done. In addition, this analysis highlight one of the key features of the DDES compared to normal DES, namely the ability to avoid grid-induced separation [34].

It is interesting to note the difference between the values obtained in the DDES and the RANS simulation. In the second case in fact, the dimension of the separated region is $1.344D_{AIP}$. Consequently, as expected, the separation zone is better described in the transient simulation, while an underestimation is present in the steady calculation.

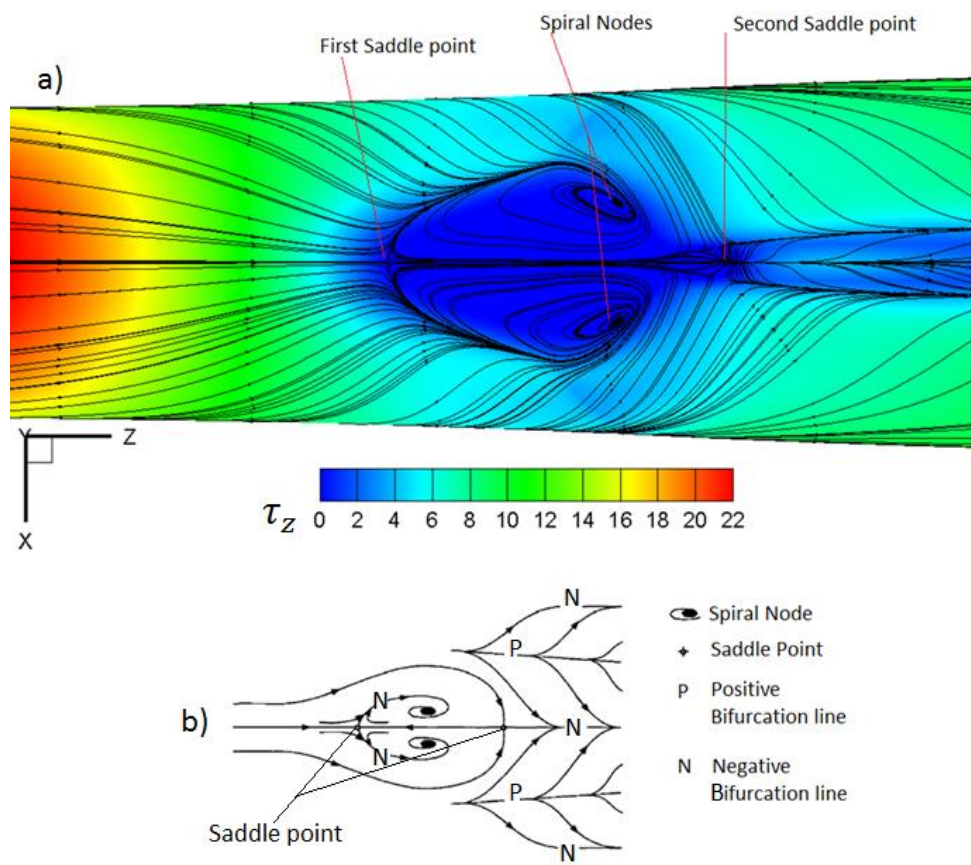


Figure 4-17 a) Skin friction lines along the wall; b) Schematic of the separation structure [42].

A final analysis was carried out. In particular the results presented in this section were compared with the data of the DDES simulation done in Cranfield University by A. Soli [12]. The geometry and the Mach number are the same but the fan simulator is not introduced, namely only the S-duct is present [12]. In particular, there is no appreciable difference in the shape of the separated

region and more importantly the position is the same in the two cases. Therefore, for both the case studied in this project and the case without the fan simulator, the first saddle point is determined at $z/D_{AIP} = 1.3$ while the reattachment at $z/D_{AIP} = 2.3$. The dimension in both cases is $1.696D_{AIP}$. This observation may seem trivial, but in reality, looking at the purposes of this work and the analysis done in the next sections, it is a remarkable conclusion. The action of the spinner is not affecting the separated region in terms of both shape and dimension. Consequently, at these positions the action of the spinner on the flow field inside the S-duct is not felt by the flow. On the contrary, as it will be underlined by means of the flow descriptors, the spinner affects the flow downstream, approaching the AIP.

4.5 Comparison: fan case vs no fan case

In this section a comparison between the fan case and the work done by A. Soli [12], is accomplished. In the following description symmetry plane and AIP plane are presented.

Figure 4-18 shows the streamlines of velocity superimposed to the contour of u-velocity at the AIP. In addition, standard deviation in both cases is presented. The main difference in terms of u-component, is related to the magnitude. In particular, without the fan simulator a value close to zero is observable in most of the section. Whereas, the fan simulator in the flow is an obstacle which tends to deflect the velocity. For this reason, two regions with higher values of u are present at the sides of the spinner. Similarly, two bottom regions of higher intensity are observed. The symmetrical structure of u, already observed in Figure 4-11, is still present in both cases.

Although the streamlines do not describe accurately the flow, they can be used to have a first insight to the vortex structure at a specific plane. As it can be seen from Figure 4-18, in both cases vortices are present at the AIP. However, looking at the case without fan simulator, the dimension of the vortex region is larger. At the same time two more vortices at the sides of the upper region (close to $+90^\circ$) are observed. On the other hand, in the fan simulator case

developed vortex structures are observed only below the spinner, with a smaller dimension. Only a qualitative description, without indication of magnitude and values, can be applied at this point. However, apparently the presence of the spinner seems to reduce the dimension of the vortex structure containing the separation. This is observed for both the larger separated area at the bottom, namely below the spinner, and the smaller separation in the upper region of the AIP (+90°).

As expected, where higher levels of fluctuations are present, namely in the separated region, in both cases standard deviation is at its maximum reaching similar values of magnitude within the two simulations.

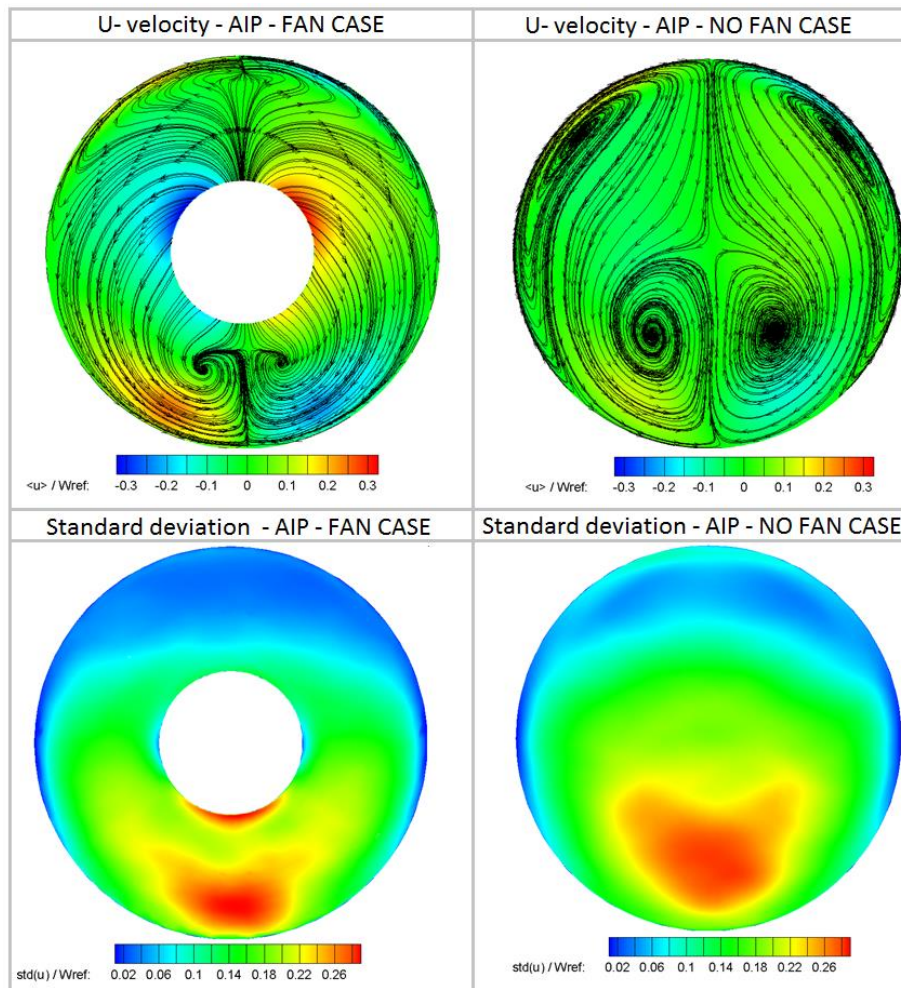


Figure 4-18 Comparison between U-velocities, standard deviation and streamlines at the AIP plane; time-averaged DDES.

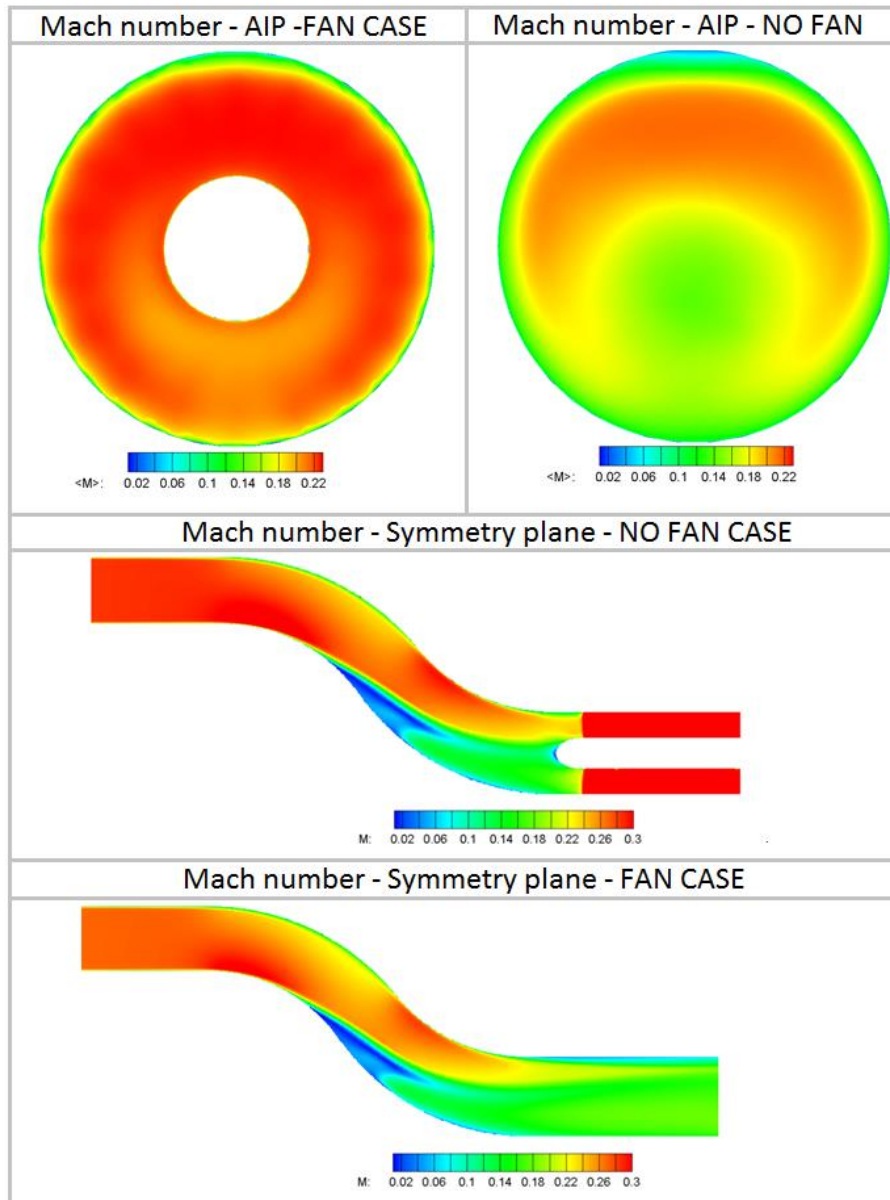


Figure 4-19 Comparison between Mach numbers at the AIP and symmetry plane; time-averaged DDES.

Figure 4-19 shows a comparison between Mach numbers at the AIP and the symmetry plane. First of all, along the symmetry plane a quite different distribution in terms of magnitude can be highlighted. The main reason is related to the presence of the throat section which chokes the flow. The fan simulator tends to decrease the area inside the duct, leading to a difference in mass flow between the two cases. As a consequence, simply looking at the continuity equation, the change in mass flow has also an effect on the values of

Mach number which tends to be higher if the mass flow decreases (for a fixed condition). In particular, a difference of 4.7% is observed at the inlet between the mass flow in the fan case and the clean case. Furthermore, at the inlet of the fan case an area-averaged value of Mach number of 0.280 is observed, while a correspondent value of 0.263, at the same plane, can be seen in the case without fan simulator. Consequently, between the two cases a difference in Mach number of 0.017 at a Mach number of 0.28 is observed.

Although the Mach numbers observed are higher in the fan case, the shape of the distribution is similar in the two cases. At the first and second bend a similar increase in velocity is present, for the reasons previously described (section 4.3.1). The values observed are in the same range. Moreover, the separated region, where very low values of Mach number are present, is not affected by the fan simulator (section 4.4) and consequently a very similar distribution is highlighted. Since the flow is choked at the throat, in the fan case the velocity tends to increase approaching the blades, whereas it decreases in A. Soli's case [12].

As previously observed in Figure 4-18, the upper region of the AIP where a second smaller separation is observed, is different in the two cases. In particular, the action of the fan simulator seems to decrease the dimension of the separation. Looking at the +90° position on the AIP section, the region at low Mach number is much smaller in the fan case, compared to A. Soli's case [12]. At the same time, the spinner constraints the bottom separation to a smaller region, if compared to the case without spinner. The higher values of Mach number at the AIP section of the fan case is related to the presence of a choked flow at the throat of the blades.

Figure 4-20 shows the contours of pressure recovery in the two cases and the correspondent standard deviation. Although the similarity with the contours of Mach number presented in Figure 4-19, in this case is better highlighted the spoiled region below the spinner and the correspondent region in A. Soli's case [12]. The effect of the spinner on the flow is evident comparing the two contours. The flow deflected by the obstacle tends to reshape around it,

assuming the distribution depicted. As expected from the analysis of total pressure, there is not a huge difference in terms of magnitude. Changes in total pressure are mainly related to losses inside the duct which are similar in the two cases.

In addition, also in Figure 4-20 it is possible to underline the difference in the dimensions of the upper region, where lower values of PR are present. In particular, in the case without fan simulator the upper separated region seems to affect a larger portion of the AIP section compared to the fan case.

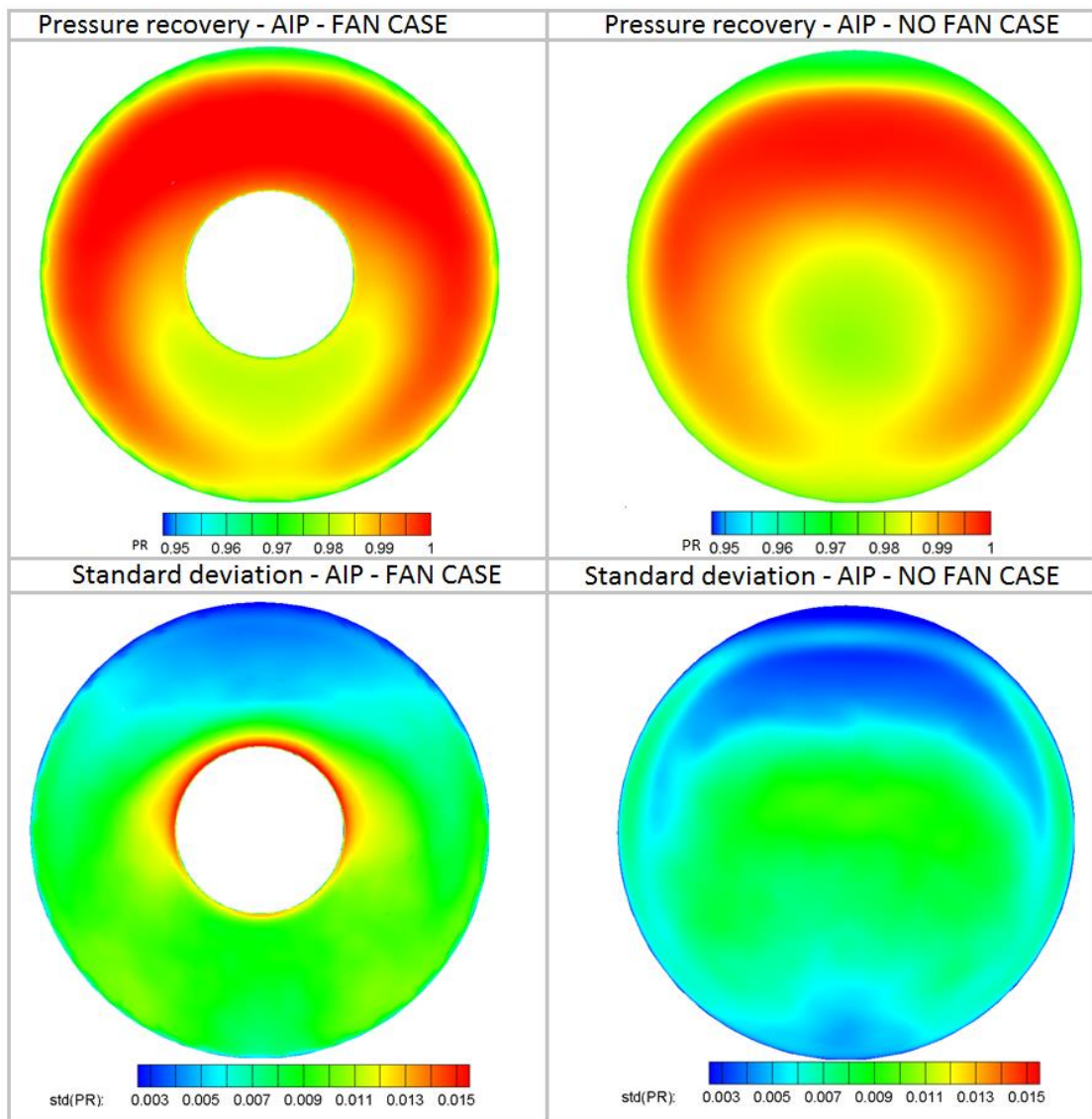


Figure 4-20 Comparison between PR values and correspondent standard deviation at AIP plane; time-averaged DDES.

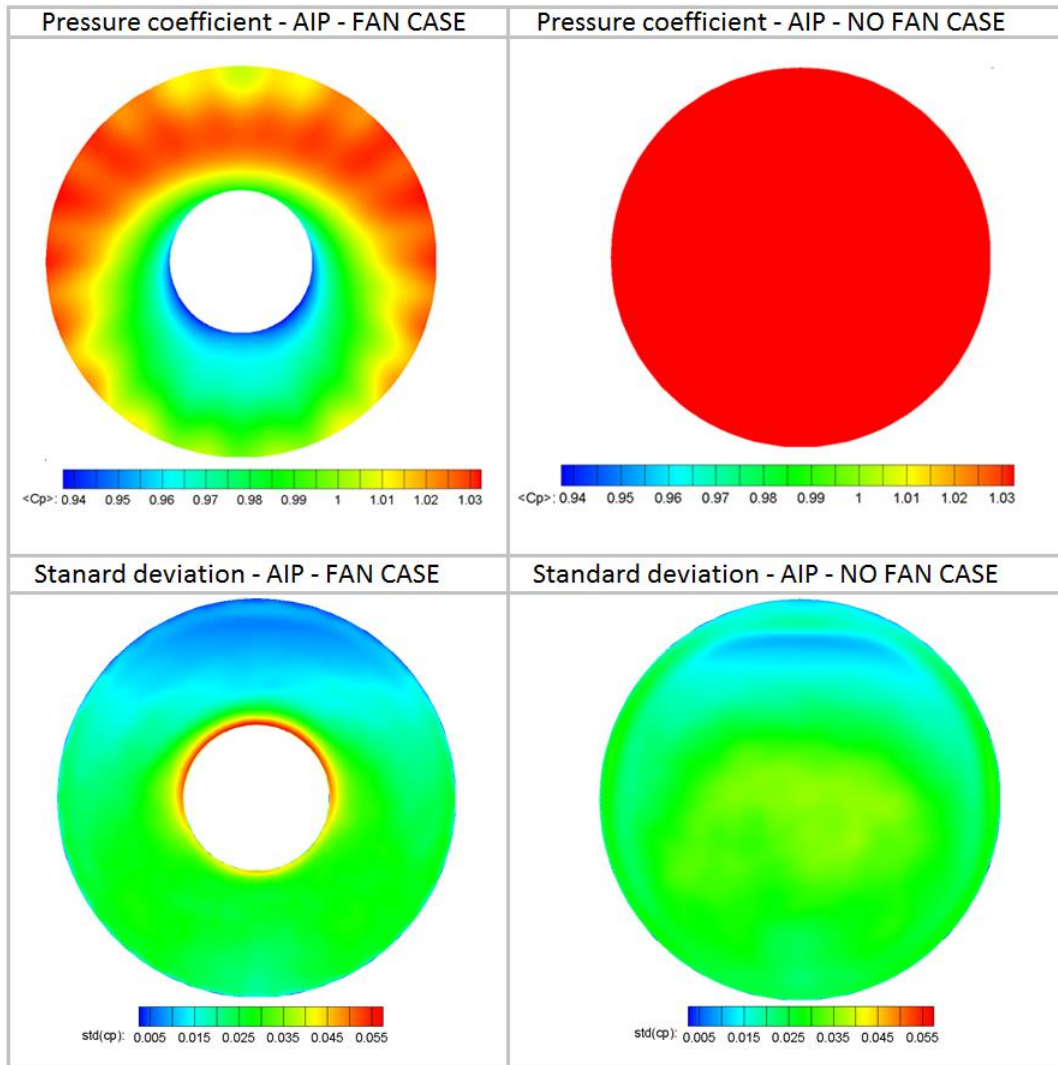


Figure 4-21 Comparison of pressure coefficient and correspondent standard deviation at the AIP section; time-averaged DDES.

Looking at standard deviation, the largest fluctuations of PR are present close to the wall of the spinner. Similar values in the two cases instead are observed in the upper and lower part of the AIP.

Figure 4-21 shows the pressure coefficient at the AIP plane for the two cases. The case without fan highlights higher values of c_p across all the section due to the lower velocity observed. By contrast, in the fan case lower values of pressure coefficient are present. In addition, it is possible to observe the influence of the blades on the pressure distribution. If downstream the wall of the blades is present, a higher value of pressure is observed at the AIP due to

the presence of a stagnation point. By contrast, if downstream there is the channel between two consecutive blades, due to the increase of the velocity to sonic condition a lower value of c_p is observed.

4.6 Descriptors of the distortion

This section will analyse both steady and transient data by means of the traditional SAE descriptors presented in Chapter 2. A comparison with A. Soli's study [12] is also accomplished. The descriptors are calculated with the common rings-per-rake arrangement where 5 equal area rings and 72 radial rakes with an angular resolution of 5° are placed along the section (Figure 4-22) [12]. In order to assess the impact of the distortion levels on the engine, the AIP will be studied with particular attention. In this work, due to the presence of the spinner at the AIP section, ring 1 is not of interest since it falls inside the wall. Only rings 3-4-5 are analysed. In order to have a better understanding of the problem, some other details related to the descriptors will be presented in this section. More basic concepts were exposed in section 2.1.5.

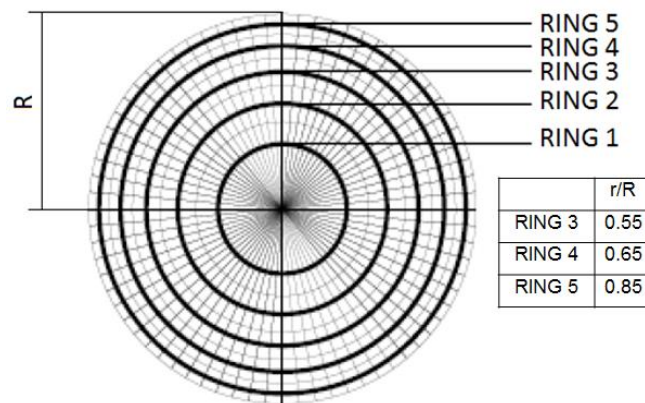


Figure 4-22 Ring arrangement in a general section.

4.6.1 Distortion statistics: AIP

In this section, the statistics of the distortion are firstly presented in Table 11 and then better described by means of cloud maps. However, a part for the extent, the descriptors analysed are averaged over the AIP section. In particular looking at SI_{mean} , SD_{mean} and SP_{mean} they are calculated by area-averaging the values at the rings, in order to have a single value per snapshot. Finally, there is

also a time-averaged operation which is described by $\langle \cdot \rangle$, leading to only one value. Obviously, there are many limitations in this approach but it provides a very handy and simple method to compare different parameters in different simulations. As far as the extent is concerned, there is not only one value in all the AIP since it is defined at every ring. For this reason, the time-averaged value is presented at three different radial positions, namely ring 3, 4 and 5. Moreover, multiple-per-revolution parameter (MPR) gives the number of equivalent low pressure regions and it is obtained from the ratio of the total integrated-area of all the regions with pressure below the ring mean value and the area with the largest defect [19].

Each parameter is presented in terms of time-averaged value, standard deviation and maximum value. In particular from the standard deviation is possible to highlight the fluctuation of the descriptors, while the maximum gives an indication of the peak reached. Furthermore, three cases are presented. First of all, the data are post-processed from the DDES with fan simulator, aim of this project. Secondly, for all the area-averaged parameters the mean value of the RANS simulation is presented. Lastly, starting from the results of the transient simulation done by A. Soli [12], the same investigation applied to the fan case is also accomplished in the geometry without static fan. As a consequence, a proper comparison between these three different simulations is done.

Looking at the values of the RANS simulation and comparing them with the DDES case, it is possible to underline a good agreement between the steady and unsteady calculation. However, RANS mean values are lower compared to the time-averaged DDES, highlighting that RANS is not able to capture peak values of the unsteady flow field that tend to decrease the time-averaged value ($\langle \cdot \rangle$) of Table 11. By contrast, this behaviour is not observed in the RDI comparison where a larger value in the steady case is present. The reason can be derived considering the description made in section 4.3.3 and in particular in Figure 4-14. As previously highlighted, two central core regions of total pressure

losses are present in the steady calculation and accordingly they are increasing the value of the RDI.

Moreover in both transient simulations, it is worth to note that for all the descriptors the peak value is around double compared to the correspondent time-averaged value, highlighting the unsteady nature of the flow analysed. In addition, this underlines that for compressor stability studies it is fundamental to consider these peaks otherwise the worst operating condition may not be included in the analysis.

Considering the Pressure Recovery in the two time-averaged DDES cases, a very close value is observed. This underlines the behaviour described previously in Figure 4-20, where, by comparison of the contours, a similar range of PR and a similar shape was observed. At the same time, peak events are not very strong since they are close to the averaged value and similarly they are rare due to the low value of standard deviation present. On the other hand, looking at DC60 the analysis shows high level of averaged distortion and high peaks in both cases. However, an higher value of DC60 is observed in the fan case. The reason for this behaviour could be related to the decrease in area at the AIP section in the fan case due to the presence of the spinner. Similarly, the spinner tends to control the spoiled region in a smaller part of the plane, namely below the spinner itself. Moreover, due to the presence of the obstacle in the flow, the actual flow area is smaller in the fan case compared to the clean case. As a consequence, looking at the definition provided in eq. (2-9), the area averaging of the pressures which leads to DC60 formulation, can provide a small difference in the values. In addition, in both cases the values of standard deviation are of the same order of the averaged values, suggesting that peaks cannot be neglected in the analysis of DC60. A similar conclusion can be drawn also looking at the standard deviation of SI_{mean} , SD_{mean} and SP_{mean} . A smaller value instead is present in CDI, RDI, MPR and Extent.

Moving to the analysis of the swirl descriptors and starting from the mean swirl directivity, it is possible to observe a value close to 0 in the fan case, highlighting that the swirl structures in the flow are compensating or totally

absent. Obviously, the first option is the one observed in this case. Even though in both cases the averaged value is very close to a twin swirl configuration, there is an appreciable difference comparing SD in the two transient simulations. In particular, without fan simulator an area-averaged value of SD of one order of magnitude higher is calculated. As it will be described in the next section, the most probable situation is very different in the clean case compared to the fan case. Peak values are higher in the case without fan simulator where the bulk swirl condition is approached. On the other hand, a lower value of time-averaged mean swirl intensity is appreciable in the fan case. Consequently, lower swirl angles are present in the flow at the AIP section from an averaged perspective, which is a good condition for the engine downstream. Similarly, also the peak value is lower in the fan case.

From a compressor operability perspective, extent is a very important variable since the compressor in most of the cases can handle only a maximum value of it, even at high frequencies [18]. Again, a lower value at all rings considered is observed in the fan case.

Table 11 Summary of distortion statistics at the AIP plane for time-averaged DDES and RANS.

		DDES: FAN CASE (AIP)			RANS: FAN CASE (AIP)	DDES: NO FAN CASE (AIP)		
		<·>	Std(·)	Max(·)	Mean value	<·>	Std(·)	Max(·)
DC60		0.31	0.13	0.76	0.28	0.29	0.10	0.69
PR		0.991	0.0008	0.994	1.03	0.992	0.0011	0.995
CDI		0.0282	0.0064	0.0507	0.0114	0.0219	0.0049	0.0465
RDI		0.0083	0.0045	0.0371	0.0092	0.0078	0.0017	0.0156
SI _{mean}		7.91	1.1573	12.6636	7.01	9.1317	1.4545	15.146
SD _{mean}		0.0006	0.32	0.84	0	-0.0089	0.46	0.91
SP _{mean}		0.96	0.12	1.54	0.8	0.88	0.14	1.53
MPR		1.09	0.21	2.97	0.91	1.13	0.25	2.9
Extent (°)	Ring 3	149.44	1.09	273.56		185.82	0.90	200.42
	Ring 4	147.21	1.37	248.16		175.42	0.81	187.37
	Ring 5	141.61	1.05	245.44		164.92	0.79	174.10

In general, a good agreement with previous results obtained by A. Soli [12], A. Giacomobello [36] and F. Wilson [13] in Cranfield University can be underlined.

Furthermore, it is to note the good agreement with the work of D. Macmanus et al. [2]. The main difference in this study is of course related to the presence of the fan simulator at the exit, which leads to the observed changes in the values.

A straightforward method to present unsteady distortion is using a cloud map which highlights the most probable events that may appear in the flow. In order to do so, the probability density function (PDF) is introduced. PDF gives the probability P of a certain phenomenon described by a specific descriptor to occur in a certain region Σ_0 of the domain. Such probability is given by eq. (4-6):

$$P(\Sigma_0) = \int_{\Sigma_0} PDF(\Sigma) d\Sigma \quad (4-6)$$

However, the non-dimensional form can be obtained from eq. (4-6) dividing PDF by the size of the domain (eq. (4-7)):

$$PDF^* = PDF[\max(x) - \min(x)][\max(y) - \min(y)] \quad (4-7)$$

where x and y are two general variables.

Figure 4-23 presents different area-averaged descriptors for both total pressure and swirl distortion at each time-step. Red regions highlight the most probable phenomena. The behaviour described with the time-averaged analysis seems to be in accordance with the cloud maps, despite for the RDI where smaller values are expected. The reason is mainly related to the large dispersion observed in the map, which tends to move at higher values the time-averaged RDI. However, all the other time-averaged descriptors fall close to the most probable region. For the purposes of the next section, it is interesting to note the behaviour of the averaged swirl descriptors and the differences between the two cases. In particular looking at SP-SD, it is possible to observe a lower dispersion of the data in the fan case, compared to A. Soli's geometry [12]. Moreover, the red regions tend to concentrate around a value of zero of SD. Consequently, a twin-swirl pattern is the most probable situation. By contrast, even if the other case is more spread around all the values of SD, it concentrates more at $SD = \pm 1$, namely the bulk swirl dominated region.

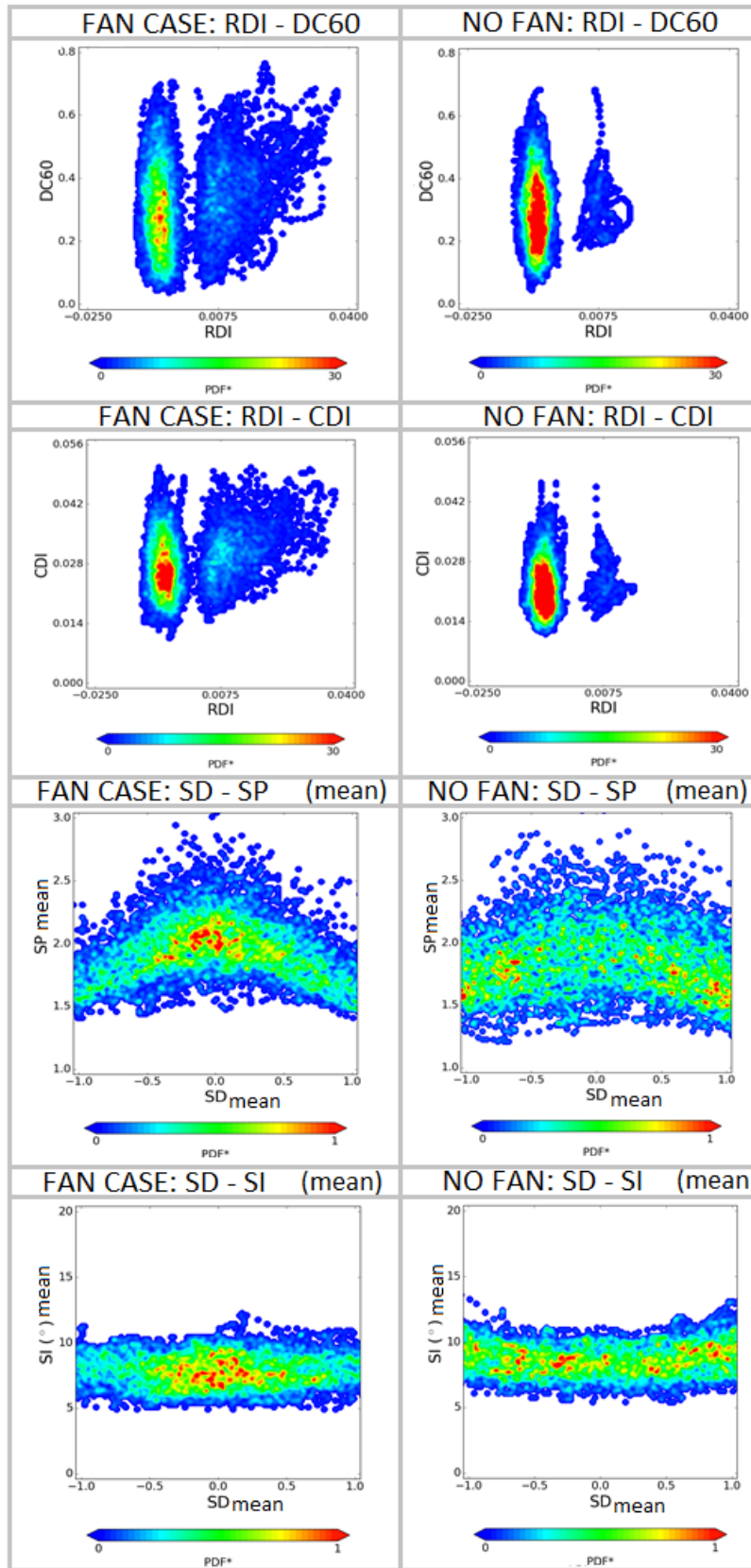


Figure 4-23 Cloud maps investigating distortion descriptors at AIP plane.

The same behaviour of SD is more clear from SD-SI map. Similarly, considering the swirl intensity (SI), a decrease in the overall range of the map is observable. Moreover, the most probable event seems to appear at lower values of SI.

Although the analysis applied so far will be developed in more detail in the next section, two important aspects related to the action of the fan simulator that must be further investigated can be underlined. Looking at the precedent maps:

1. The flow pattern at the AIP is highly modified. In the clean case bulk swirls are observed, while in the fan case twin swirls are more probable.
2. The swirl intensity is decreased by the presence of the static fan.

However, in order to have a more reliable approach, in the following section swirl descriptors will be analysed and compared at different ring position.

4.6.2 Swirl descriptors at different rings of the AIP

Figure 4-24 shows and describes the meaning of SP-SD cloud map with the hyperbolic pattern determined by Gil-Prieto et al. [4]. The function that governs the diagram is expressed by eq. (4-8):

$$SP = \frac{1}{1 + |SD|} \quad (4-8)$$

In particular, the peak for SP=1 and SD=0 corresponds to the symmetrical swirl pattern, while moving to positive values of swirl directivity with a decreasing swirl pair, a positive offset swirl is achieved. At a value of SP=0.5 and SD=1, the positive bulk swirl configuration is reached [4]. Similarly, the same behaviour is observed moving towards negative values of SD, where a negative bulk swirl configuration is observed at SP=0.5 and SD=-1. Consequently, the flow undergoes a series of different states (from negative bulk swirl to symmetrical pair and finally positive bulk swirl), with a motion called vortex switching. During this phenomena one of the vortex structures become alternatively predominant on the others [44]. Figure 4-25 shows a comparison of the SD-SP map at different rings of the AIP for the two transient simulations.

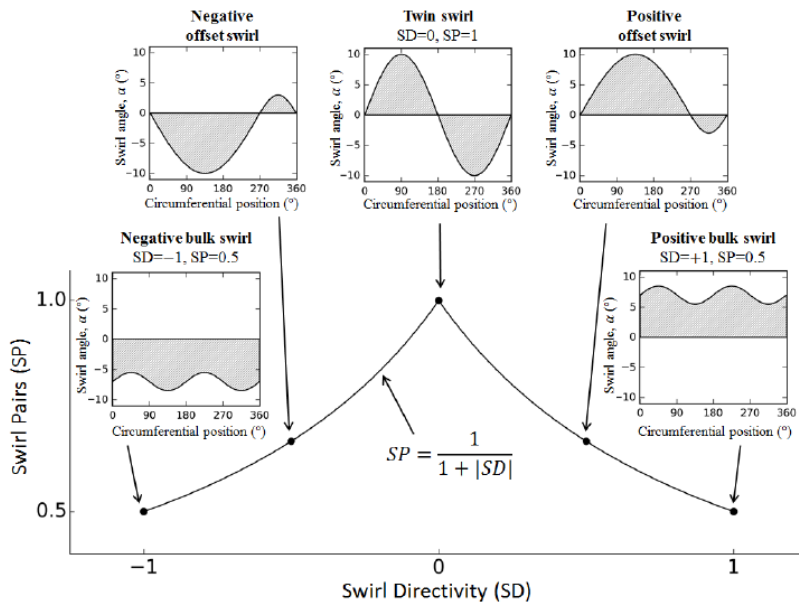


Figure 4-24 Description of the SD-SP map [4].

Looking at the results over all the rings in the fan case simulation, it is possible to highlight how the most probable configuration is the symmetrical flow structure, namely the twin swirl. This is particularly true for the inner ring where the red region of high probability falls in a small range of SD. Basically, it extends between -0.15 and +0.15 of SD. Moving to outer rings instead, the dimension of the highest probability region increases, allowing the presence of positive and negative offset swirls. However, in all rings the probability to have a bulk swirl configuration seems to be much lower compared to the probability to have a twin swirl. Consequently, for the fan case a single peak behaviour around the twin swirl is observed. Furthermore, the probability for $SP > 1$ can be explained by the presence of a second, more external, swirling pair which is present in both cases.

The data described so far suggest that the vortex switch mechanism in terms of highest probability is present but, especially at inner rings, the switch happens around structures very close to the symmetrical pattern. Looking at the cloud maps of A. Soli's geometry [12], the behaviour observed is very different. In particular comparing inner rings, in this case a two peak configuration with both negative and positive bulk swirl is the most probable. Moving to outer rings, the behaviour is still present at a radial position of $r/R=0.65$.

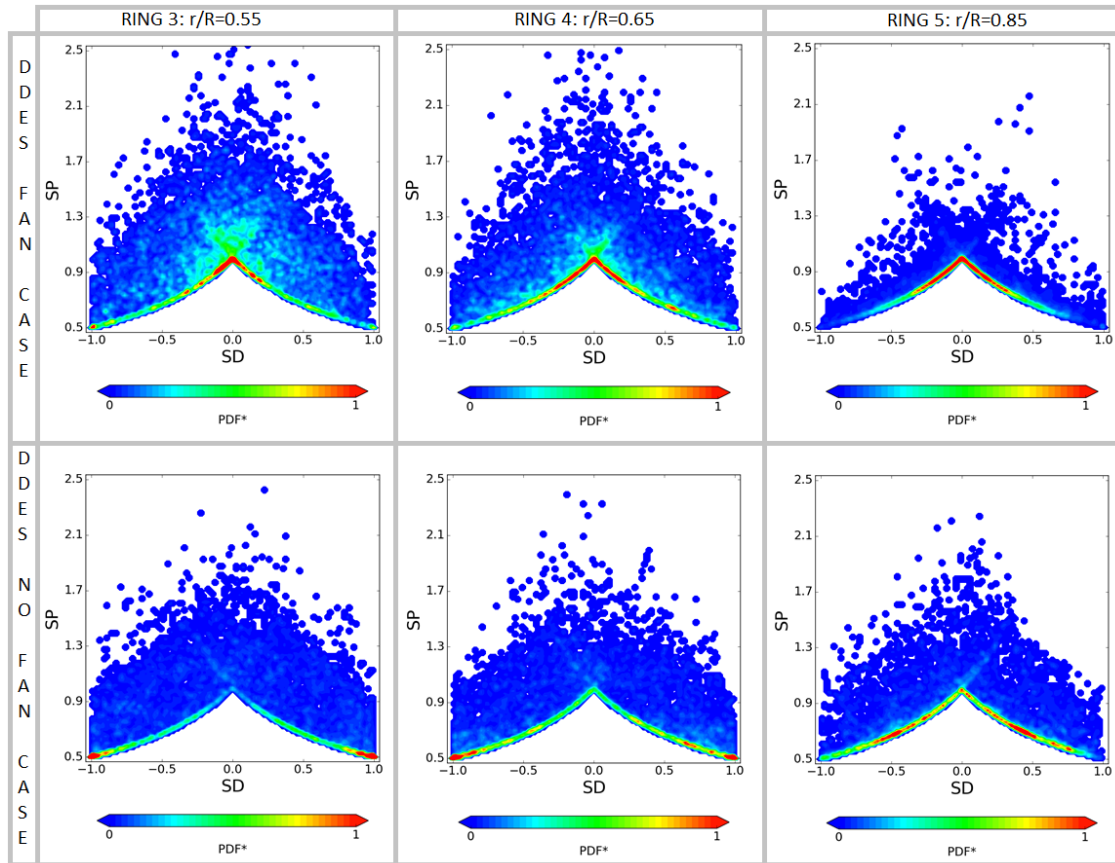


Figure 4-25 SP-SD cloud maps; Comparison of the two DDES simulations at the AIP.

By contrast, at ring 5 red regions are present at intermediate values of SD, underlining a negative or positive offset swirl with one vortex significantly larger than the others.

Figure 4-26 shows swirl intensity against swirl directivity for the two cases, adopting PDF* in order to highlight the most probable regions. The same precedent observation regarding the shape of the pattern, can be underlined also in Figure 4-26. In particular, looking at SD in both simulations, a symmetrical structure is the most probable situation in the fan case while a bulk swirl dominates the case without static fan. Only the outer ring, as mentioned describing Figure 4-25, allows positive and negative offset swirl thanks to the intermediate values of SD observed.

Focusing our attention on SI instead, it is important to note the different range of values reached. Without fan geometry, larger values of SI are present. At the

inner and medium ring, the most probable region goes from around 12° to 17° and in general it spreads from 5° to 24° at ring 3, while from 5° to 18° at ring 4. Lower values are present at the outer ring where the most probable region is concentrated at values of 8°. Looking instead to the fan case, swirl intensity oscillate between 5° and 18°. Lower values are present only at the outer ring. For SD=0, an averaged value of 7° is observed at all the rings. In addition, looking at the most probable region and comparing it with the clean case, SI range generated by a bulk swirl event is more scattered than that generated by a twin pair. Consequently a larger range of values of the most probable region are present in the case without fan simulator.

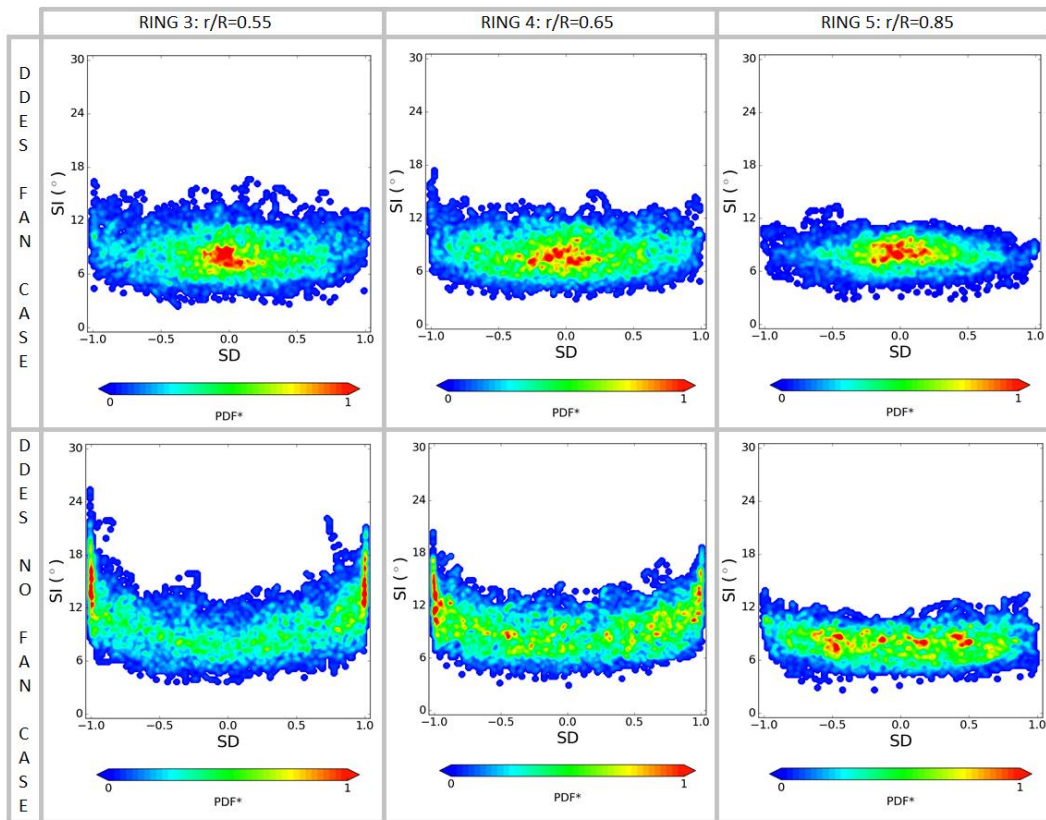


Figure 4-26 SI-SD cloud maps; Comparison of the two DDES simulations at the AIP.

Figure 4-27 shows SI-SP cloud maps and it highlights the same characteristics previously mentioned just with a different combination of the descriptors. Consequently similar conclusions can be drawn from the description of Figure 4-27.

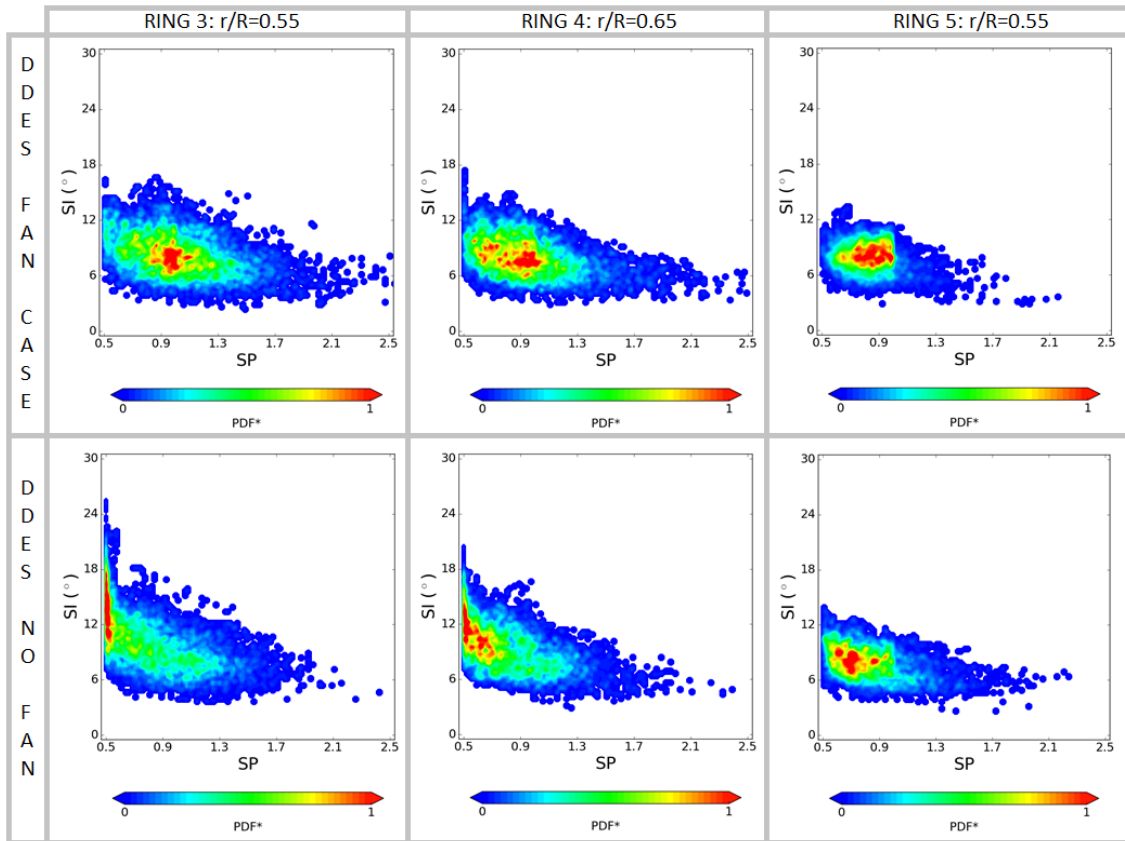


Figure 4-27 SI-SP cloud maps; Comparison of the two DDES simulations at the AIP.

Table 12 and Table 13 show the probability P of an event to appear and they quantify the behaviours previously depicted. It is not calculated on a specific point but on an area and for this reason a range in terms of $SP \times SD$ or $SI \times SD$ is provided. The three positions $SP [0.95, 1.05] \times SD [-0.1, 0.1]$, $SP [0.5, 0.6] \times SD [0.8, 1]$ and $SP [0.5, 0.6] \times SD [-1, -0.8]$ (similarly for SI) correspond to the most probable regions highlighted previously where twin swirls or bulk swirls can be observed. From the analysis of Table 12, it is evident that the probability to have a twin swirl in the system with the fan simulator is much higher compared to the clean case. Moreover, moving from inner to outer rings, such probability increases and the difference between the two cases become more evident. The highest probability ($P=14.62\%$) is at ring 5. By contrast, as expected from the previous analysis, looking at the regions where bulk swirls are predicted to appear the fan case highlights minimum values of probability,

while A. Soli's geometry [12] has the highest P. Similar values are observed for both clock and counter-clock bulk swirls.

Table 12 Probability P of a phenomena to appear over the area range SPxSD

	RING 3		
	SP [0.95, 1.05] x SD [-0.1, 0.1]	SP [0.5, 0.6] x SD [0.8, 1]	SP [0.5, 0.6] x SD [-1, -0.8]
DDES FAN CASE	7.40%	1.23%	2.55%
DDES NO FAN CASE	1.51%	10.78%	9.42%
	RING 4		
	SP [0.95, 1.05] x SD [-0.1, 0.1]	SP [0.5, 0.6] x SD [0.8, 1]	SP [0.5, 0.6] x SD [-1, -0.8]
DDES FAN CASE	8.43%	2.27%	2.24%
DDES NO FAN CASE	3.13%	8.25%	9.43%
	RING 5		
	SP [0.95, 1.05] x SD [-0.1, 0.1]	SP [0.5, 0.6] x SD [-0.8, 1]	SP [0.5, 0.6] x SD [-1, -0.8]
DDES FAN CASE	14.62%	1.14%	1.28%
DDES NO FAN CASE	4.10%	2.46%	4.41%

In terms of SI (Table 13), in order to study twin swirl and bulk swirl regions two different ranges are presented. First of all, it is possible to observe that the fan case has an high probability to have a swirl intensity within the range of SI [6°, 8°] x SD [-0.1, 0.1] while almost zero in SI [11°, 18°] x SD [±0.8, ±1]. Basically, this does not underline only the already mentioned aspect related to the type of swirl pattern observed, but also that the static fan tends to allow swirls with lower swirl angles. Only at ring 5, the two cases show a similar behaviour in terms of SI, as also described in Figure 4-26 and Figure 4-27.

Table 13 Probability P of a phenomena to appear over the area range SixSD

	RING 3		
	SI [6°, 8°] x SD [-0.1, 0.1]	SI [11°, 18°] x SD [0.8, 1]	SI [11°, 18°] x SD [-1, -0.8]
DDES FAN CASE	7.01%	0.81%	1.83%
DDES NO FAN CASE	2.01%	10.42%	8.84%
	RING 4		
	SI [6°, 8°] x SD [-0.1, 0.1]	SI [11°, 18°] x SD [0.8, 1]	SI [11°, 18°] x SD [-1, -0.8]
DDES FAN CASE	6.91%	0.60%	1.23%
DDES NO FAN CASE	2.52%	7.86%	8.22%
	RING 5		
	SI [6°, 8°] x SD [-0.1, 0.1]	SI [11°, 18°] x SD [-0.8, 1]	SI [11°, 18°] x SD [-1, -0.8]
DDES FAN CASE	7.72%	0.00%	0.22%
DDES NO FAN CASE	3.20%	1.21%	2.47%

From the diagrams shown, the two aspects highlighted in the averaged statistics analysis previously made are also verified in this section, studying the swirl descriptors at different rings. First of all, the shape of the flow is different in the two configurations, moving from a bulk swirl pattern at the AIP of the clean case, to a twin swirl at the AIP of the fan case. It may seem an aspect of secondary importance but on the contrary is one of the most important conclusion related to this project. The engine tends to reshape the flow field at the AIP from a bulk swirl to a twin swirl.

In addition, introducing the fan simulator at the exit of the S-duct, the swirl intensity at ring 3 and 4 is reduced by almost 50%. As mentioned in section 2.1.5.2, SI measures the swirl angle at the considered plane, namely the

distortion levels at the AIP. Consequently, the decrease of SI observed by introducing the engine face, is followed by a decrease in the actual flow distortion level at the AIP plane.

The consequences on the performance of the whole engine of the two main findings just presented is not the real aim of this project but inevitably an obvious question arises: which is the impact of the reshape of the flow and the decrease of the swirl intensity introducing the static fan simulator at the AIP on the overall performance of the engine? An answer related to this specific case studied cannot be given in this instance since a proper analysis is not accomplished and in general it is a very complex topic where the current research is strongly working. However, a brief presentation of some recent results on similar studies done by different institutions is considered appropriate in order to have a better understanding of the importance of the problem and the findings as well as guidelines for future works that will be done in Cranfield University.

The CFD analysis over a compressor stage carried out by J. Marty et al. [45] showed some interesting consequences of steady distortion on compressor performance. The unsteadiness at the AIP is responsible for a modification of shock and separation over the rotor blades as well as a modification of the separation over the stator suction surface [45]. The main consequence is a decrease of the surge margin observed comparing it with a undistorted flow field. However, in the experimental work done by P. M. Rademakers [46] some more aspects can be pointed out. In this case they assessed the impact on the engine performance of the distortion at the AIP experimentally, for different configurations. The main aspects can be summarized as follow:

1. The LPC efficiency is influenced significantly only when a disturbed incident angle on the compressor inlet flow is observed due to swirl distortion. By contrast, SFC is mainly influenced by inlet total pressure distortion [46].
2. For many test cases there is a linear correlation between surge margin of the compressor and descriptors of the flow distortion which is an

essential information for the design of an S-duct. In particular both SFC and inlet compressor total pressure ratio are linearly correlated to total pressure distortion, namely increasing the distortion a linear decrease of the two performance parameters is highlighted [46].

3. Although the stability of the compressor is not very influenced by a twin-swirl pattern, the performance of the engine seems to be highly negatively affected by it [46].

5 ADVANCED PROCESSING METHODS

5.1 Dynamic mode decomposition: recent applications and studies

Section 5.2 will provide a detailed description of the methodology, theory and objectives of Dynamic Mode Decomposition (DMD) while in this section the most recent results obtained in different studies will be analysed. The explanation, the mathematics and the theory beyond the model is given in section 5.3.

The two most important advantages of the DMD are [47]:

1. Compared to a Proper Orthogonal Decomposition (POD), time evolution is available for each mode obtained from the DMD study [47].
2. Time averaged description of the flow is present inside DMD modes [47].

Consequently, the DMD method allows a better approximation of the flow by means of the modes computed by the algorithms. In particular, several types of DMD have been studied in the past but the most recent one, namely Sparsity-promoting Dynamic Mode Decomposition (SP-DMD), significantly reduces computational time providing a good description of the flow behaviour. For this reason, SP-DMD is the method studied and presented in this work. One of the first studies was carried out by H. Koizumi et al. [47] in a work for JAXA (Japan Aerospace Exploration Agency). The validation of the code developed was applied on a well-known flow over a 2D flat plate at $Re=100$, with an angle of attack α of 30° . DMD was applied on data from LES of that geometry with a mesh of 24080 cells [47]. Even though the flow analysed was simple, this study provides good visualization and application of DMD. The number of snapshots to build the matrix for the SP-DMD were of 501 components of u-velocity. Figure 5-1 shows three modes for a flow over a flat plate. Mode 1 represents the time averaged flow, mode 2 a Strouhal number (St) typical for a Karman's vortex and mode 3 is a harmonic of mode 2 [47]. The time evolution of mode 2 is determined by twice multiplying the real part of mode 2 with the corresponding eigenvalue. As with POD, because modes are complex

numbers, magnitude and phase information can be plotted in a frequency space. From phase it is possible to highlight wave fronts [47].

As can be seen, the flow reconstructed using the time averaged mode and mode 2, provides a good approximation of the CFD analysis. In H. Koizumi et al. [47] an error of 10^{-4} is found.

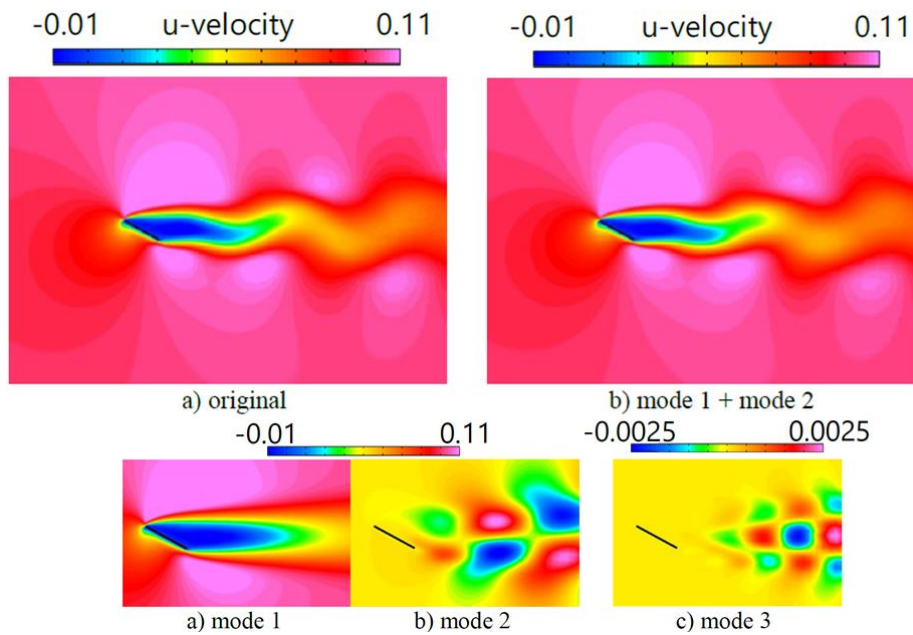


Figure 5-1 Modes and reconstructed flow over a flat plate with SP-DMD [47].

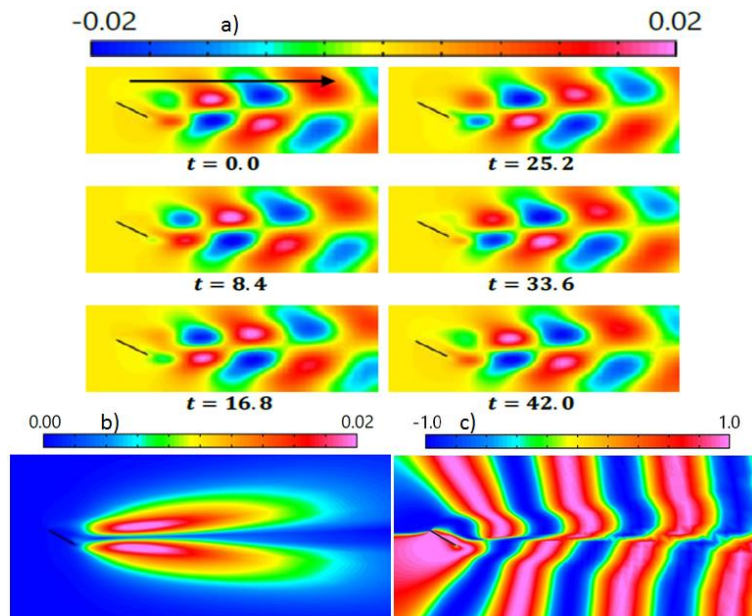


Figure 5-2 a) time evolution mode 2, b) magnitude mode 2, c) phase mode 2 [47].

A second study, conducted by L. Ragnar et al. [48], on a DES of a separated nozzle flow for space applications, highlighted not only the potential of SP-DMD to identify periodic flow behaviour but also the most recent limitations of such a method in advanced aerodynamics [48]. Two different cases were simulated by applying the DES method. The first one at a nozzle pressure ratio (NPR) of 14.67, while the second for a NPR=19.74 [48]. DMD was able to determine the ovalization mode predicted by the simulation in the case with the lower nozzle pressure ratio and properly reconstruct the flow in the case with the higher NPR [48]. However, the most important limitation observed in both cases is the lower ability of SP-DMD to detect modes responsible for low-frequency peak, probably due to the influence of resolved turbulence, compared to peaks at higher frequencies [48]. Figure 5-3, shows the peak in pressure and axial velocity at NPR=14.67. On the x-axis St is presented as a function of $\|\alpha\mu^k\|$ (where μ are the eigenvalues) on the y-axis. In both cases a dominant mode at $St=0.12$ for the snapshot $k=140$, determined with SP-DMD, is present. This mode is described in Figure 5-4. In particular the symmetrical structure on the axial plane is worth noting [48]. In Figure 5-4 it is possible to see, at two different locations (the symmetry plane of the control volume and the exit plane of the nozzle), the previously mentioned ovalization mode due to the symmetrical structure on the axial plane and a wave number of $m=2$ [48]. Despite the problems in detecting low-frequency modes, DMD is able to detect and understand behaviours which can contribute to nozzle side load or ovalization [48].

Finally, one last important analysis was accomplished by D. Lengani et al. [49] in an experimental study of a laminar separation bubble over a low pressure turbine blade [49]. They reconstructed the flow starting from a time-resolved particle image velocimetry (TR-PIV) by means of POD and DMD techniques, producing a low order model ranked by the energy content (POD) or by the contribution of each mode on the dynamics of the system (DMD). A comparison between a POD mode and a DMD mode is presented in Figure 5-5, where it is possible to see periodical fluctuations (from negative to positive values) in the vertical direction due to the presence of a vortex structure in the separation

bubble. The description of the fluctuation is similar in both methods, with similar distribution along the y -axis [49].

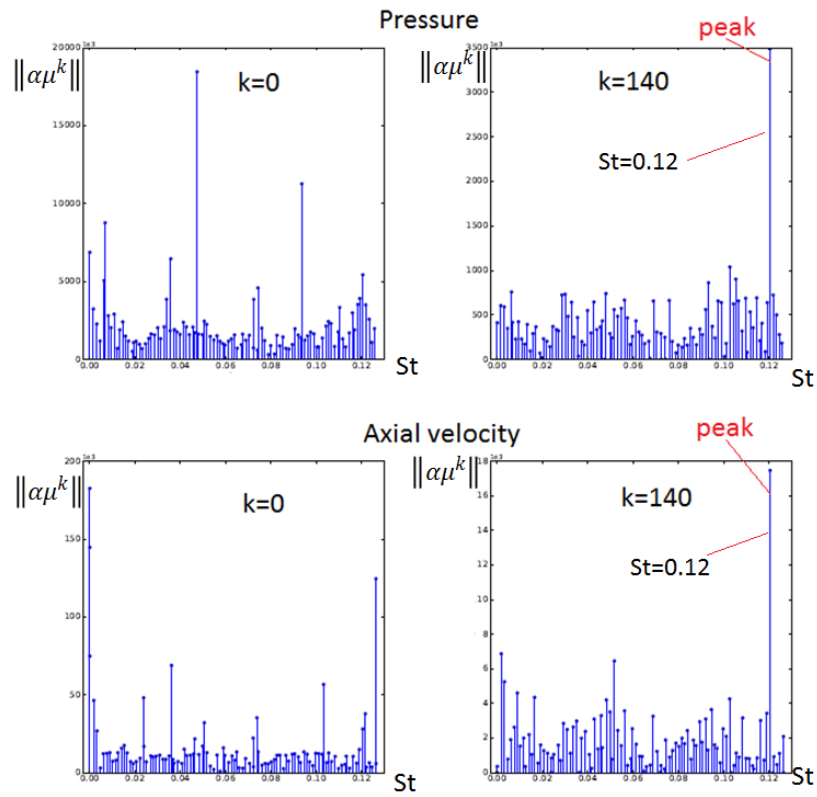


Figure 5-3 Pressure and axial velocity peaks from S-P DMD, NPR=14.67 [48].

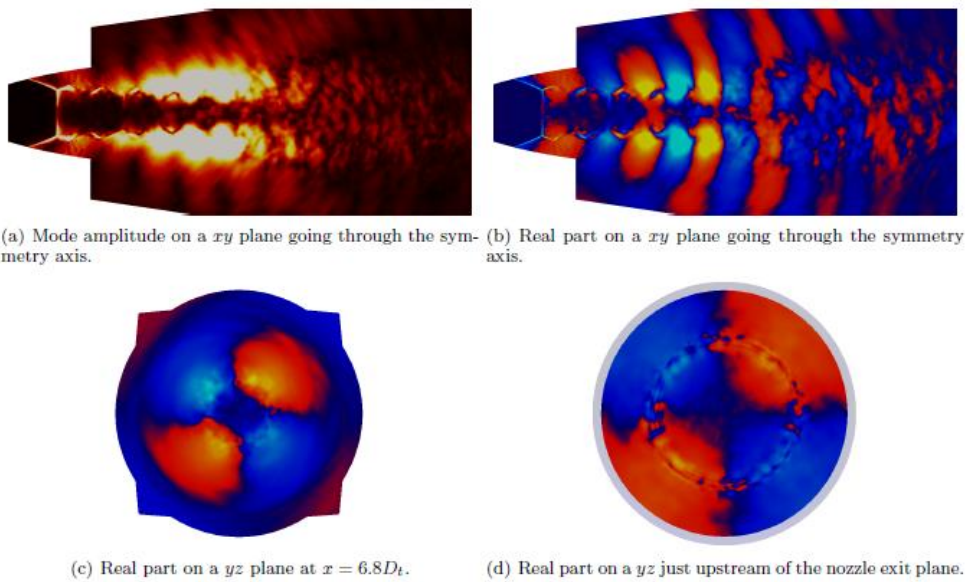


Figure 5-4 Ovalization mode on symmetry plane and axial plane from SP-DMD analysis [48].

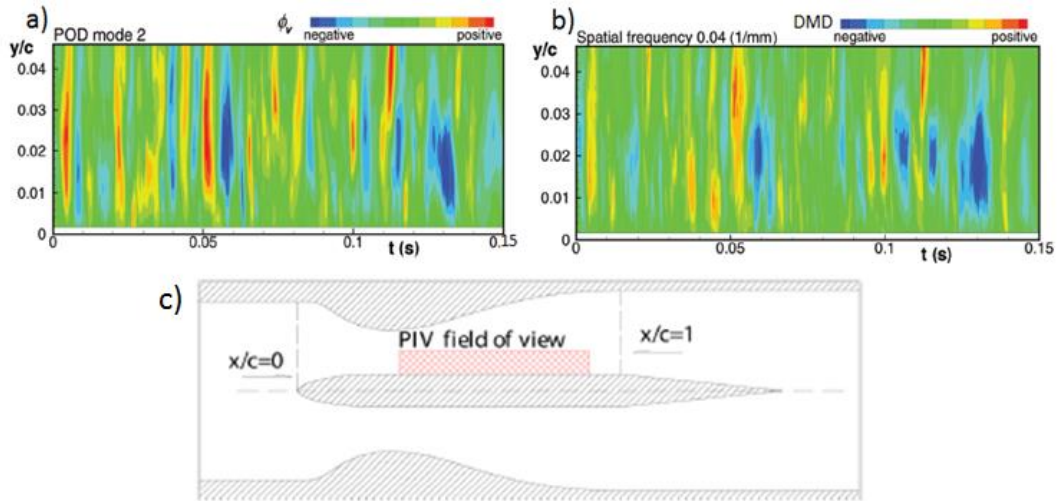


Figure 5-5 Comparison between POD and DMD spatial mode; c) TR-PIV location on the LPT blade [39].

The most important aspect achieved by the DMD relates to the number of information that can be obtained and consequently the better description of the properties of the flow. In particular, from the study of the eigenvalues the spatial frequency and the growth rate are derived (Figure 5-6 (a)) [49].

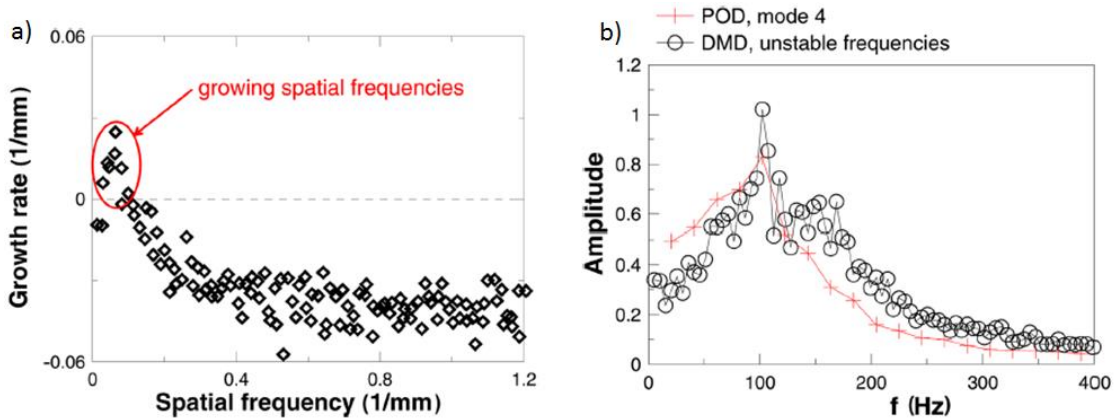


Figure 5-6 Growth rate distribution and comparison between DMD and POD temporal frequency [49].

Spatial frequency is the reciprocal of the wavelength while growth rate is defined as the ratio between the amplitude of the mode $|\phi_i|$ and the time-step Δt [50]. Positive values indicate spatially evolving structures and in particular, increasing the spatial frequency, they tend to decay earlier. Moreover, applying a Fast Fourier Transform (FFT) to the DMD modes with positive growth rate,

temporal frequency can be derived and a comparison with POD shows the good agreement between the two techniques (Figure 5-6 (b)) [49].

5.2 DMD and SP-DMD: methodology

The description of unsteadiness and distortion in complex geometries from both experiments and simulations represents a great challenge if we consider in particular the algorithms able to extract the needed information to quantify the behaviour of the flow. In this context, direct methods become prohibitively expensive and iterative procedures were developed [51]. In many practical situations engineers employ data-based modal decomposition to study dynamical systems such as an unsteady flow. By means of these techniques it is possible to simplify very sophisticated dynamical operators by numerically analysing empirical data from experiments or simulations and so obtain modes with dynamically significant structures [52]. For example, during post processing of a simulation using decomposition techniques it is possible to identify coherent structures such as vortices or eddies, fundamental for the correct description of the flow field [53].

One common decomposition model, widely used in recent years, is called Proper Orthogonal Decomposition (POD). It aims to decompose the flow into a sum of spatially orthogonal modes starting from snapshots of the flow field; it is applicable to both experiments and simulations. It identifies the most energetic structures by diagonalizing the spatial correlation matrix computed from the snapshots with a quadratic norm [51]. Consequently, POD is close to the original data set in a least-squares sense. Although the good description and the lower computational cost of POD compared with other decomposition methods, it suffers from the following issues [51]:

1. Energy does not always describe the flow field accurately [51].
2. It uses second order statistics as an approximation for the decomposition [51].

Highly relevant structures with zero-energy modes are sometimes found in the flow, so the first issue is particularly serious [54].

Dynamic mode decomposition (DMD) is a recent method developed by Schmidt and Sesterhenn [51] that describes the dynamic information of a flow from both experimental data and simulation results [51], thereby overcoming the limitations of the POD analysis. It is a data-driven, matrix-free method which relies only on input data and ignores the underlying matrix system [51]. DMD approximates the modes of a Koopman operator computing, from empirical data, eigenvalues and eigenvectors of a linear model that approximates the dynamics of the flow, even if the dynamic is not linear [52]. The Koopman operator is a mathematical entity defined by I. Mezic as an infinite-dimensional linear operator that describes flow field data defined on a state space of a dynamical system [55]. The practical idea behind a Koopman analysis is to start from a set of data, understand which observables are of interest and then express them in terms of Koopman modes and eigenvalues [52]. In particular, DMD algorithm modes constitute a subset of Koopman modes and eigenvalues from a finite set of data. Unlike the POD method, DMD decomposition leads to growth rates and frequencies associated to each mode determined from the magnitude and phase of each corresponding eigenvalue [52].

To conclude, DMD provides two different results that will be presented in the following section: the modes ϕ_i and the eigenvalues λ_i . From the study of ϕ_i , which are not orthogonal like in POD, it is possible to identify coherent structures in the flow [49]. To each mode there is a different frequency associated. On the other hand, λ_i provides the frequency information from the imaginary part of the number while the growth rate of the dynamic structure is obtained from the real part [49]. Consequently, POD and DMD are quite different since POD modes are orthogonal in space, while DMD modes extract spatial structures for a given frequency [49].

5.2.1 Mathematical background of DMD and SP-DMD

The data coming from simulations or experiments should be presented in the form of a snapshot sequence, given by the matrix V_1^N in eq. (5-1) [51]:

$$V_1^N = \{v_1, v_2, \dots, v_N\} \quad (5-1)$$

Where v_i stands for the i -th flow field vector. In V_1^N , the subscript 1 stand for the first member of the sequence, while N stands for the last one. Each flow field vector is separated by the constant time step Δt [51]. The structure of the matrix can be now presented eq. (5-2):

$$V_1^N = \begin{bmatrix} u_1^{(1)} & u_1^{(2)} & \dots & u_1^{(N)} \\ \vdots & \dots & \dots & \vdots \\ u_M^{(1)} & \dots & \dots & u_M^{(N)} \\ v_1^{(1)} & v_1^{(2)} & \dots & v_1^{(N)} \\ \vdots & \dots & \dots & \vdots \\ v_M^{(1)} & \dots & \dots & v_M^{(N)} \end{bmatrix} \quad (5-2)$$

In particular, the in-plane velocities (u , v) are studied. Moving along a column, from 1 to M , the velocity at each different node is represented. Moving instead along a row, for the same node, the velocity is introduced at different time steps (from 1 to N). This is the most important matrix, coming from the DDES calculation and at the basis of this method.

Assuming a linear mapping A that connects the vectors v_i with v_{i+1} than it is possible to write (eq.(5-3)) [51]:

$$v_{i+1} = Av_i \quad (5-3)$$

From eq. 5-2 and eq. 5-3, we can observe the basic of the DMD is to assume that the dynamical shifting of the whole data set ensemble over a small time interval Δt can be expressed by a linear matrix A [56]. DMD provides a method to determine a lower order representation of A , which is able to capture the dynamics contained in the data [57]. As the number of snapshots increase the vectors given by eq. (5-1) become independent and can be rewritten as follow (eq. (5-4)) [51]:

$$V_2^N = AV_1^{N-1} = V_1^{N-1}S + re_{N-1}^T \quad (5-4)$$

Where e_{N-1}^T is the $(N-1)$ th unit vector, r the residual vector and S a companion matrix with the unknown coefficients $\{a_1 \dots a_{N-1}\}$ of the linearization of v_N in the last column. The determination of S cannot be applied directly because the problem as stated in eq. (5-4) is ill-conditioned and it is impossible to extract

more than the first two dynamic modes [51]. Several algorithms have been developed recently but the most widely used is based on an algebraic method called singular value decomposition (SVD), where \mathcal{S} is replaced by introducing a similarity-transformed matrix $\tilde{\mathcal{S}}$ [56]. SVD is applied to the data sequence \mathbf{V}_1^{N-1} and substituting the result of the decomposition in eq. (5-4), thus obtaining eq. (5-5) [51]:

$$\tilde{\mathcal{S}} = \mathbf{U}^* \mathbf{A} \mathbf{U} = \mathbf{U}^* \mathbf{V}_2^N \mathbf{W} \mathbf{\Sigma}^{-1} \quad (5-5)$$

Appendix B provides a more detailed description of the SVD method and the terms involved. Eq. (5-5) is the starting point of the DMD method and for this reason is of fundamental importance. The symbol $(\cdot)^*$ is used to indicate the conjugate-transpose of a matrix. In particular it is fundamental to characterize \mathbf{U} , because it is not simply a result of the SVD procedure, but it also contains the POD modes of the data sequence \mathbf{V}_1^{N-1} [51]. Consequently, the operation described in eq. (5-5) corresponds to the projection of the linear basis \mathbf{A} onto the POD basis [51]. More importantly, $\tilde{\mathcal{S}} = \mathbf{U}^* \mathbf{A} \mathbf{U}$ from equation eq. 5-5 correlates POD modes \mathbf{U} with the structures shifted over one time step Δt , expressed by $\mathbf{A} \mathbf{U}$. For this reason, $\tilde{\mathcal{S}}$ gives more information about the temporal evolution of the process than the time-averaged POD modes from \mathbf{U} [51]. Once $\tilde{\mathcal{S}}$ is determined by applying the SVD decomposition, the eigenvalues λ_i and eigenvectors y_i are computed. In this way, the dynamic modes ϕ_i are found applying eq. (5-6) [51]:

$$\phi_i = \mathbf{U} y_i \quad (5-6)$$

So far the DMD method can be summarized in the following four steps:

1. Split the time series of data \mathbf{V}_1^N in two matrices \mathbf{V}_2^N and \mathbf{V}_1^{N-1} .
2. Apply the SVD algebraic method to \mathbf{V}_1^{N-1} obtained calculating \mathbf{U} (Appendix B).
3. Form the matrix $\tilde{\mathcal{S}}$ and compute its eigenvalues and eigenvectors of it.
4. Use eq. (5-6) to determine the i -th dynamic mode ϕ_i .

5.2.1.1 Optimal amplitudes of DMD modes and algorithm structure

The matrix $\tilde{\mathcal{S}}$ determines an optimal low-dimensional representation of the inter-snapshot mapping \mathbf{A} on the subspace of the POD modes of \mathbf{V}_1^N [57]. The dynamics on this r -dimensional subspace $\tilde{\mathcal{S}}$ (Appendix B) are governed by a relationship similar to eq. (5-3) but in a different subspace with different dimension, namely $\mathbf{x}_{t+1} = \tilde{\mathcal{S}}\mathbf{x}_t$. Consequently the matrix of the POD modes can be used to move \mathbf{x}_t into a higher dimensional space \mathbb{C}^M (the space of \mathbf{v}_i) with a simple mapping expressed in eq. (5-7) [57]:

$$\mathbf{v}_t = \mathbf{U}\mathbf{x}_t \quad (5-7)$$

Starting from the eigenvectors y_i and eigenvalues λ_i of $\tilde{\mathcal{S}}$, eq. (5-7) can be brought into a diagonal form and the snapshots can be approximated using a linear combination of the DMD modes (eq. (5-8)) [57]:

$$[\mathbf{v}_1, \mathbf{v}_2, \dots, \mathbf{v}_{N-1}] \approx [\Phi_1, \Phi_2, \dots, \Phi_r] \begin{bmatrix} \alpha_1 & & 0 \\ & \ddots & \\ 0 & & \alpha_r \end{bmatrix} \begin{bmatrix} 1 & \lambda_1 & \dots & \lambda_r^{N-1} \\ \vdots & \vdots & \ddots & \vdots \\ 1 & \lambda_2 & \dots & \lambda_r^{N-1} \end{bmatrix} \quad (5-8)$$

where, starting from the left side of eq. (5-8), the first matrix is \mathbf{V}_1^{N-1} . On the right side of the expression instead the first term is the matrix of the dynamic modes determined using eq. (5-6), the second is a diagonal matrix \mathbf{D}_α and finally the last matrix is the Vandermonde matrix $\mathbf{V}_{and} \in \mathbb{C}^{r \times N}$ [57]. In particular, \mathbf{D}_α is composed of r coefficients of amplitude α_i which quantify the i -th modal contribution of the initial condition \mathbf{x}_0 on the subspace spanned by the POD modes of \mathbf{V}_1^N [57]. The Vandermonde matrix instead governs the temporal evolution of the dynamic modes [57]. This is shown in Figure 5-7. When $\Phi\mathbf{D}_\alpha\mathbf{V}_{and}$ is expanded like in Figure 5-7, each term is described as the time evolution of a mode with its amplitude [47]. In POD, the eigenvalue can be interpreted as a physical quantity, in particular as energy. By contrast, DMD eigenvalues have no order despite frequencies. For this reason it is necessary to determine α [47]. The optimal vector of DMD amplitudes α_i is chosen in order to minimize the Frobenius norm of the difference between \mathbf{V}_1^N and $\Phi\mathbf{D}_\alpha\mathbf{V}_{and}$ [57] and expressed by eq. (5-9)

$$\alpha = \mathbf{P}^{-1}q \quad (5-9)$$

where $\mathbf{P} = (\mathbf{Y}^* \mathbf{Y}) \cdot (\overline{\mathbf{V}_{and} \mathbf{V}_{and}^*})$ and $q = \overline{\text{diag}(\mathbf{V}_{and} \mathbf{V}_{and}^* \mathbf{Y})}$. \mathbf{Y} is the matrix of eigenvectors. It is important to note that “.” represents the elementwise multiplication of two matrices. The optimum approximation of the data sequence is obtained by a superimposition of the DMD modes, weighted using the amplitudes α_i and multiplied by the temporal decay rate.

To conclude, Dynamic mode decomposition can be used to represent experimentally or numerically generated snapshots as a linear combination of DMD modes, appropriately weighted by their amplitudes and advanced in time according to their temporal growth rate [57].

Starting from the mathematical background a schematic was created of the algorithm to implement. The map in Figure 5-8 describes the concept and the structure of the code to develop for the use in complex aerodynamics.

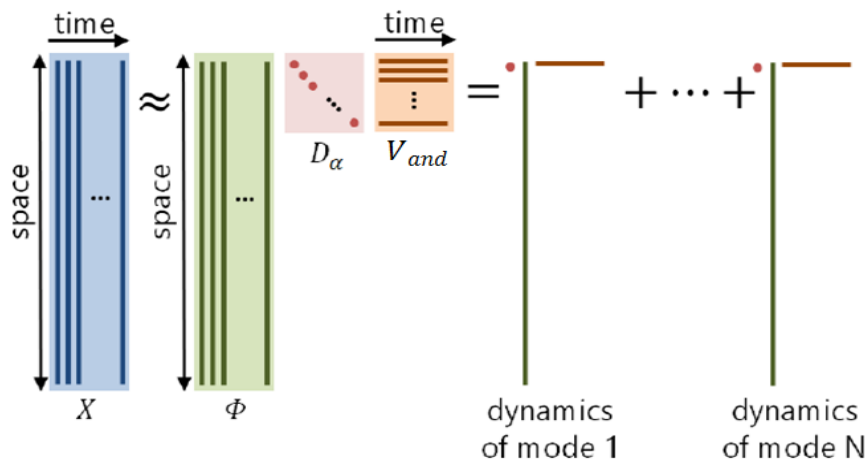


Figure 5-7 Description of eq. (5-8) in DMD; meaning of each matrix [47].

5.2.1.2 Sparsity-promoting DMD

The selection of the modes which have the most important impact on the flow is one of the key aspects of the current research related to DMD modelling and is based on the study and determination of the amplitudes of \mathbf{D}_α . The model proposed by Jovanovic et al. [57] is called Sparsity-promoting DMD and is based on the minimization of the following expression in eq. (5-10):

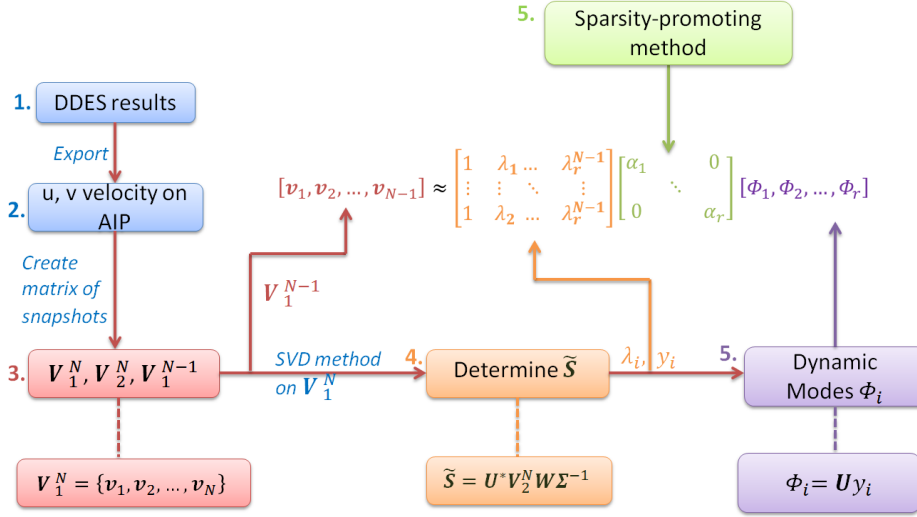


Figure 5-8 General map of the algorithm used to implement DMD method.

$$\text{minimize}_{\alpha} J(\alpha) + \gamma \sum_{i=1}^r |\alpha_i| \quad (5-10)$$

where γ is a regularization parameter and $J(\alpha)$ is determined by eq. (5-11):

$$J(\alpha) = \alpha^* P \alpha - q^* \alpha - \alpha^* q + s \quad (5-11)$$

and $s = \text{trace}(\Sigma^* \Sigma)$. Consequently, the Sparsity-promoting DMD problem expressed by eq. (5-10), is a convex optimization problem solved using standard optimization solvers. Basically, the optimization process of eq. (5-10) determine the location of non-zero values in the vector of amplitudes [57]. The method of optimization proposed by Jovanovic et al. [57] is called Alternating Direction Method of Multipliers (ADMM). A description of the algorithm is provided in Appendix C. A second optimization is then applied (eq. (5-12)):

$$\text{minimize}_{\alpha} J(\alpha), \quad \text{subjected to } E^T = 0 \quad (5-12)$$

where E contains the information of the sparsity structure of the vector α . A sparse matrix is intended a matrix in which most of the terms are zero. In particular, the non-zero elements in the column of E represents the zero values of the α vector [57]. A more complete description is provided in Appendix C. This second optimization adjusts the values of these non-zero entries to optimally approximate the whole data sequence [57]. The algorithm used for

this step is described in Appendix C. A map of the overall algorithm is presented in Figure 5-9 which continues the description of the algorithm started in Figure 5-8.

Consequently, as described in Figure 5-9, the output of this procedure is the vector of the amplitude α which is the diagonal of the matrix \mathbf{D}_α . \mathbf{V}_1^{N-1} is fully decomposed.

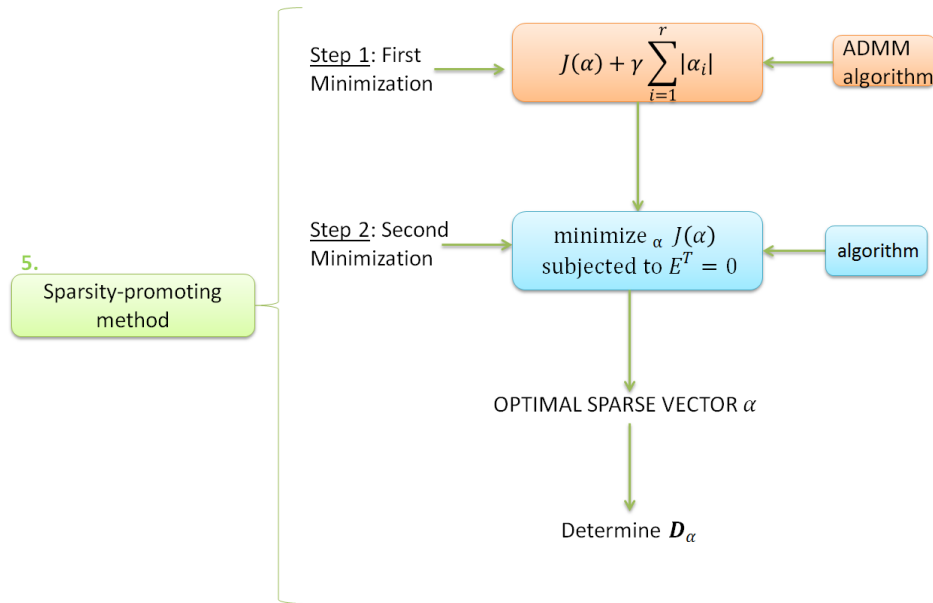


Figure 5-9 Sparsity-promoting algorithm.

To conclude, two important properties of the overall SP-DMD method are exposed at this point [47]:

1. From a real input data, complex DMD eigenvalues and DMD modes forms complex conjugate pairs.
2. From a real input data, the amplitudes pairs of a DMD mode obtained by minimization of $J(\alpha)$ also form a complex conjugate pair.

From the second property, since the sum of any complex conjugate DMD modes pair eliminate its imaginary part, the pair corresponds to the component oscillating at a specific frequency [36]. Basically, these two properties show that twice the real part of a DMD mode corresponds to the physical quantity [36].

5.3 Application of Dynamics Mode Decomposition

5.3.1 Verification of MATLAB code for SP-DMD analysis

The aim of this section is firstly to introduce the work and the code which implements the SP-DMD developed in MATLAB by Jovanović et al. [49]. Secondly, this section wants to highlight the reliability of the code and to show it really performs as it should by obtaining the same results presented in Jovanović et al. scientific paper [49]. In this way, a validation of the code can be achieved and consequently, in the future, it can be improved to study DDES data from the analysis carried out in Cranfield University. At the same time, a first comprehension of DMD is achieved.

Jovanović et al. [49] have investigated three different flow fields and consequently three different sets of data can be introduced in the code. The first type of flow is a two-dimensional Poiseuille flow with $Re=10000$, which has a numerical solution from the linearized Navier-Stokes equations. The code solve the equation numerically and the matrix of snapshot to introduce in the DMD algorithm is easily obtained. The second flow field analysed is a screeching supersonic jet in a convergent rectangular nozzle (Figure 5-10) with aspect ratio of 4 where the geometry is obtained from an experimental work. Screech is a component of supersonic jet noise associated with a train of shocks within the jet column [49]. In this case, the matrix of snapshot was generated using data from a LES simulation. The third case uses PIV data from an experiment of a flow through a cylinder bundle. For the purposes of this work and the future applications of SP-DMD the second case, namely the supersonic jet flow, is studied. This is a very good example not only because the data come from a transient simulation (LES) similarly to the work carried out in this thesis, but also because the presence of a tonal process in a highly turbulent flow makes it an excellent test case [49].

The stagnation pressure and temperature inside the nozzle were set so that the jet Mach number $M_j=1.4$ and the fully expanded jet temperature are equal to the ambient temperature [49]. A rectangular nozzle whose interior cross section area was decreasing monotonically from inlet to exit was used. Since the nozzle

did not have a diverging section before its exit, the flow left the nozzle in an under-expanded (sonic) condition and kept to expand downstream to reach the supersonic fully expanded state [49]. This induced a train of diamond-shaped shock cells as shown in Figure 5-10 (b).

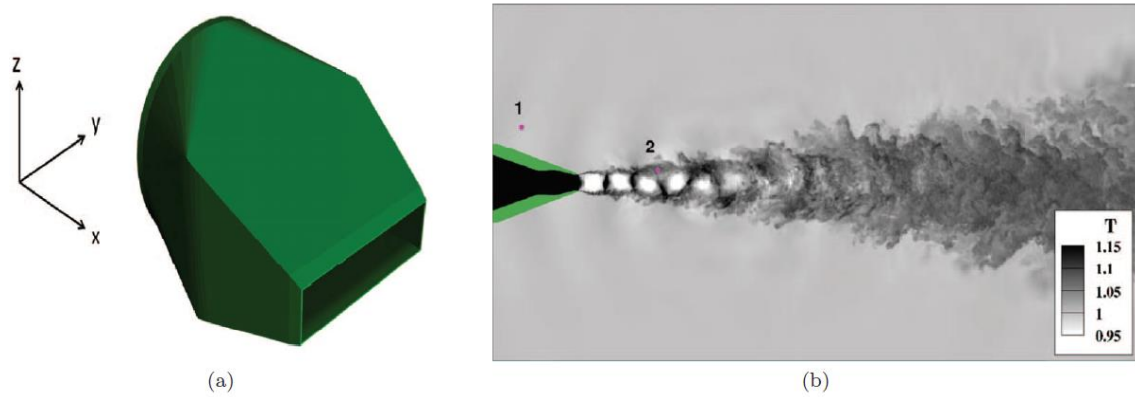


Figure 5-10 a) Geometry used for the LES simulation of the screeching supersonic jet; b) train of diamond-shaped shock cells in static temperature contour [57].

The objective of the DMD analysis carried out by Jovanović et al. [49] using its own MATLAB code on the flow presented was to extract the entire coherent screech feedback loop from the turbulent data and to describe the mechanism of screech with the lowest number of modes possible [49].

The database used for the DMD is composed by $N=257$ snapshots in terms of three-dimensional velocity and pressure field. The time step that divides each snapshot is $\Delta t=0.0528 \times D_e/\mu_j$ where D_e is the nozzle equivalent diameter and μ_j is the fully expanded jet velocity [49]. The DMD analysis is applied to a domain of approximately $10D_e$ with a total number of cells equal to 8×10^6 , quite close to the number of nodes used in the medium mesh of the S-duct studied in this project [49].

Figure 5-11 (a) and (d) illustrate how the amplitudes of the DMD modes determined from the optimisation process (section 5.2.1) depend on the frequency. In particular, the same dependence determined with the MATLAB code is compared to the diagram reported in Jovanović et al. [49] and good agreement is found. $|\alpha_i|$ stands for the amplitude while the frequency is

determined as the imaginary part of the eigenvalues (μ_i in Jovanović et al. [49]). Similarly, Figure 5-11 (b-c) and (e-f) show the dependence of amplitudes on the real part of the eigenvalues. In particular, Figure 5-11 (e-f) is a zoomed version of (b-c) and it focuses on the amplitudes that correspond to lightly damped eigenvalues [49]. It is important to note that it is not trivial to determine by a simple inspection a certain number of DMD modes which represent the strongest impact on the quality of the least-square approximation of the flow [49].

Figure 5-12 underlines that keeping only a subset of DMD modes with large amplitudes it may have a bad impact on the quality of the solution providing a poor quality of the approximation of the numerically generated snapshots [49]. However, a compromise between quality of the approximation and computational time have to be met; consequently the choice of the number of modes must respect not only the wanted loss in performance but also the time required. It is worth to remember that DMD tries to determine a low order representation of A , since in general A have a large number of complex entries. This was previously described with eq. (5-5), where $\tilde{\mathcal{S}}$ was derived. On $\tilde{\mathcal{S}}$ it is possible to apply the decomposition, obtaining eq. (5-8) where the modes are present explicitly. Figure 5-12 shows how the performance loss ($\% \Pi_{loss}$) depend on the number of modes (N_z) and a parameter γ which is a user defined parameter that is a measure of preference between approximation and solution sparsity [49]. Larger values of γ encourage a sparser solution and consequently γ_{max} corresponds to an α with a single non-zero element. By contrast a minimum value of γ leads to a dense vector of α (in this example 256 non-zero elements) [49]. Moreover, performance is determined as a Frobenius norm of the approximation error between the low-dimensional representation of the full data sequence and the data sequence itself. Increasing the number of modes the performance of SP-DMD increases as well. As it is possible to observe from Figure 5-12, agreement between the code and Jovanović et al. [49] is reached. The optimal solution for this problem is found directly from the SP-DMD algorithm obtaining an optimal number of DMD modes $N_z=47$, once the optimal sparse vector α_{sp} is determined (Appendix B).

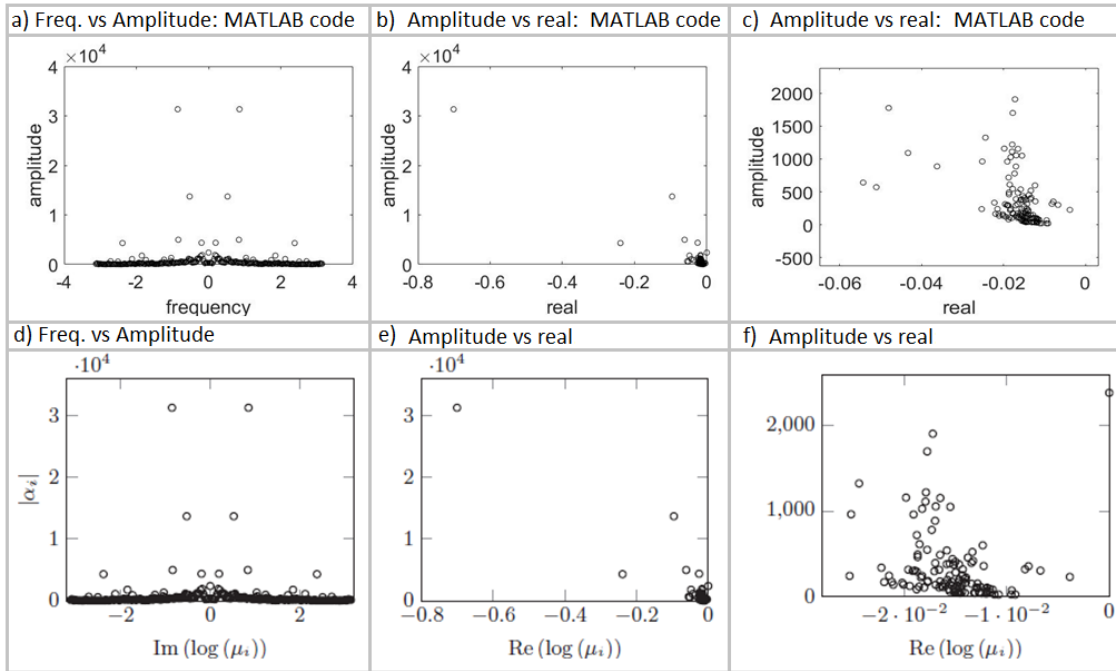


Figure 5-11 Comparison between amplitude vs frequency plots of Jovanović et al. scientific paper and the MATLAB code; Agreement is found [49].

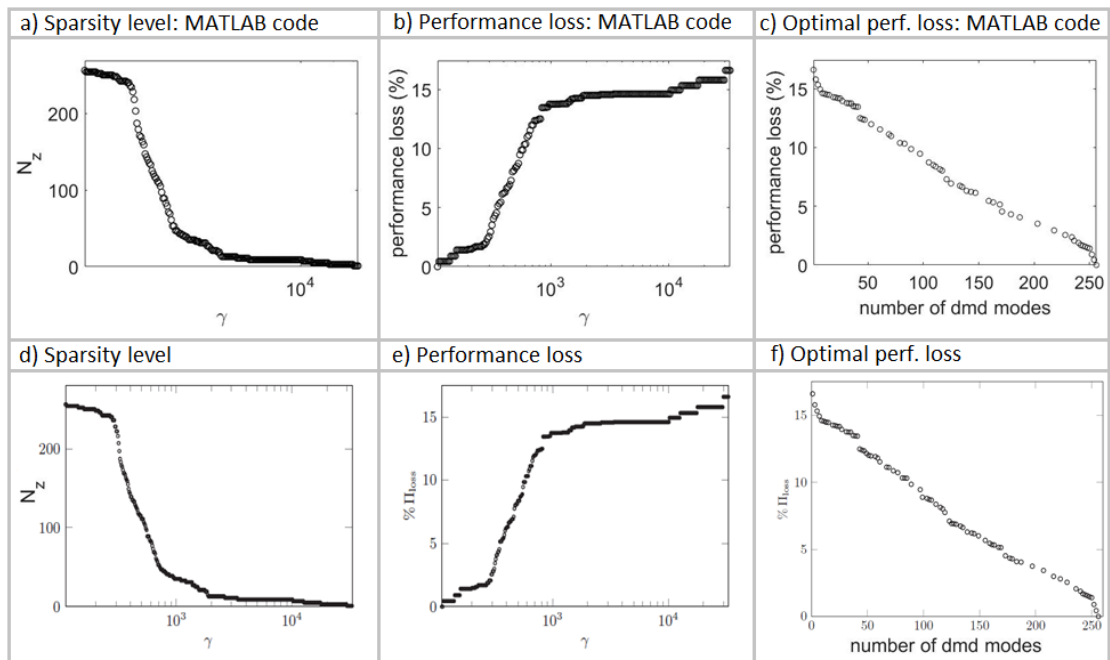


Figure 5-12 Comparison of performance loss plots and number of modes of Jovanović et al. scientific paper and the MATLAB code; Agreement is found [49].

Figure 5-13 (a) shows all the eigenvalues resulting from the DMD analysis (circles) and the subset identified by the SP-DMD algorithm (red crosses). All the eigenvalues falling inside the unit circle are strongly damped. The amplitude $|\alpha_i|$ in that case can be large because strongly damped modes influence only early stages of time evolution. This aspect is depicted also in Figure 5-11 (b-e). In addition, it is possible to highlight how SP-DMD does not focus the attention only on large amplitude modes like a normal DMD method but it considers the modes who have the highest influence on the entire time history of the available snapshots [49]. Figure 5-13 (b) shows the dependence of the absolute values of amplitudes $|\alpha_i|$ on the frequency (imaginary part) of the corresponding eigenvalue μ_i . Again, the circles represent the full set of DMD modes while the red crosses are the selected modes using the SP-DMD method. It is important to underline how the original DMD modes are not able to provide sufficient guidance to reduce the full set of modes to some more relevant than others [49]. Figure 5-14 illustrates the same trend and behaviour previously seen in Figure 5-11 in terms of total eigenvalues and amplitude. However, in this case a total number of 5 and 3 eigenvalues are selected and consequently $N_z=5$ or $N_z=3$.

While the selection of the eigenvalues as already stated is not trivial, decreasing N_z SP-DMD increasingly tends to focus on low-frequency modes [49]. For example, in the case of $N_z=3$ only the mean flow and one dominant frequency are taken into consideration. In particular in this case, the frequency considered is the fundamental frequency of the screech tone. Similarly, with $N_z=5$ a second lower frequency is identified [49].

Consequently, it is clear that in the case of a low number of modes ($N_z=3$ or 5) SP-DMD uses the most prevalent structures to approximate the data. Obviously, as seen in Figure 5-12 a decrease in quality, namely an increase in performance loss, is expected. However, considering the St number typical of the screeching phenomena studied by Jovanović et al. [49] with the higher value of $N_z=47$ and comparing it with the one obtained using $N_z=3$, a good

agreement can be highlighted. In particular in the first case $St=0.3104$ while in the second case an approximated value of $St=0.3$ is determined [49].

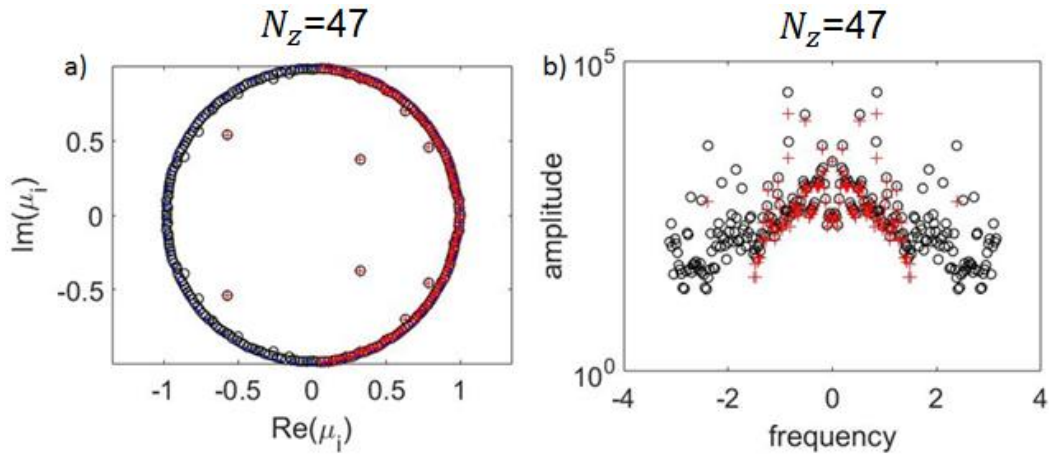


Figure 5-13 a) Eigenvalues resulting from standard DMD algorithm (circles) and the selected eigenvalues from SP-DMD algorithm (crosses); b) Correspondent amplitude of modes; a)-b) from MATLAB code.

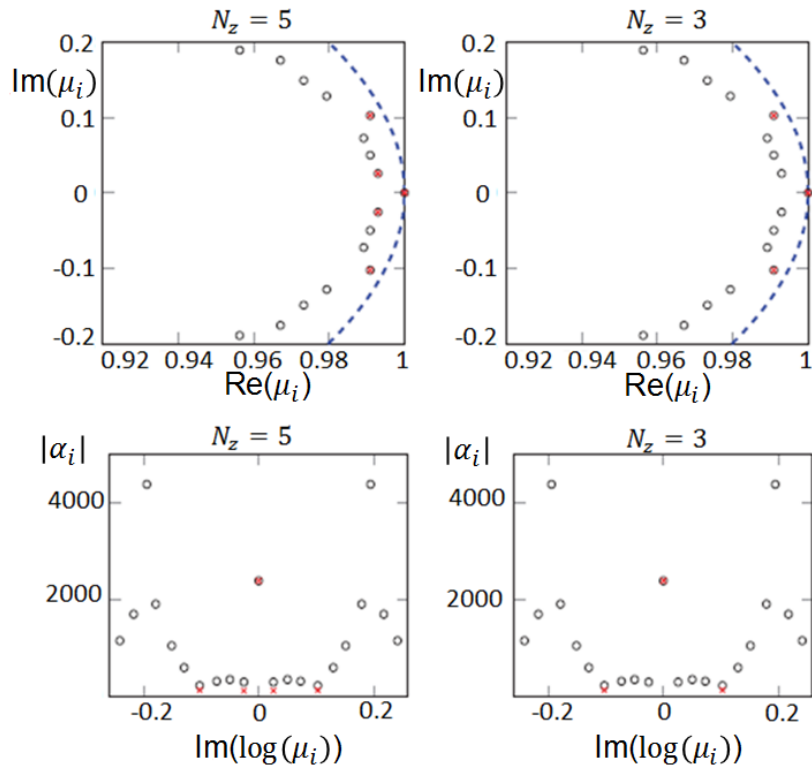


Figure 5-14 Eigenvalues resulting from standard DMD algorithm (circles) and the selected eigenvalues from SP-DMD algorithm (crosses) and correspondent amplitudes for a lower number of optimal modes N_z ; MATLAB code.

Consequently, depending on the application, it is possible to use a lower number of modes capturing only the most relevant structures but at the same time accomplishing a faster algorithm and achieving a very good agreement with the same study but with higher resolution. This underlines the solid and reliable algorithm behind SP-DMD, making it a very useful and added tool for post-processing of huge amount of data coming from both CFD analysis, like in this work, or experimental data adopting the same approach and the same code.

Figure 5-13 and Figure 5-14 illustrate some interesting behaviours of the modes that can be derived from the analysis of the plot of the eigenvalues in the complex plane. First of all, a typical circular pattern with the eigenvalues in complex conjugate pairs is observed. As already stated, only a few eigenvalues fall inside the circle, showing a damped behaviour. The reason why the complex normalised eigenvalues follow a circular distribution is still not well understood [58] and the only attempt to properly characterize this behaviour can be found in Girko's circular law [59]. However, is still not fully verified mathematically [58] and for the purposes of this work it is taken as a fact. Moreover, it is possible to say that most of the modes are stable since a negative value of the real part of the selected eigenvalues is observed [50] in the plot of Figure 5-13 and Figure 5-14. One final observation relevant for future analysis is related to the eigenvalues positioned in the positive range but at a zero value of the imaginary part. These eigenvalues are related to the modes which capture only the mean flow [60]. Eigenvalues close to zero capture the mean flow and the most dominant structures evolving in time [60].

5.3.2 DMD code applied to DDES data

A first investigation of the transient data from the DDES using the DMD technique is carried out. The code adopted is a modified version of the one studied in the previous section and developed by Jovanović et al. [49]. The algorithm implemented in terms of functionality and outputs is maintained the same of Jovanović et al. [49] but it is accordingly changed in order to read the data of the CFD simulation processed using CUDatapro 3.6. The development

of the code was accomplished bearing in mind that different simulations not only of S-ducts but also related to other activities in Cranfield University can be analysed directly using this code. Both experimental data and CFD data processed through CUDatapro 3.6 can be easily seen as an input of this code. The code is still written in MATLAB.

The input of the code is the matrix of snapshots as previously described in section 5.2.1 by eq. (5-2). In particular, the matrix contains a number of 500 snapshots and each snapshot is divided by a time-step of $\Delta t = 1.2 \times 10^{-5} s$. Moreover, the matrix is composed using three different flow variables: u-velocity, v-velocity and w-velocity at the AIP section. The number of snapshot, the variables used and the time-step are not a requirement for the functionality of the code. This means that they can be changed choosing different flow properties, different time-steps or a larger number of snapshots, as long as the structure of the input matrix (eq. (5-2)) is respected.

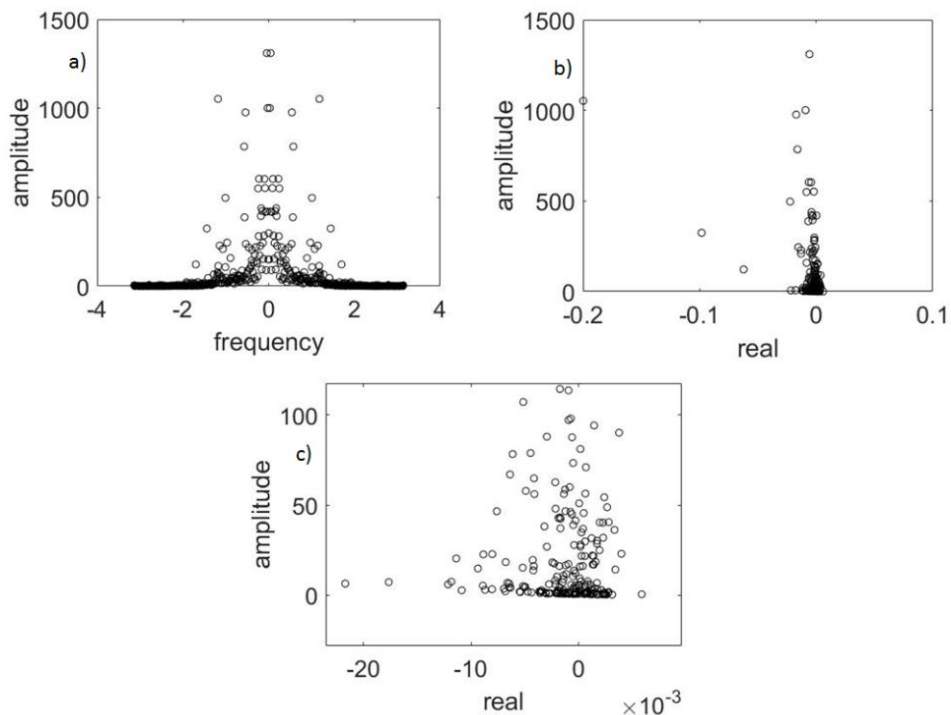


Figure 5-15 a) Amplitude vs frequency of the eigenvalues; b-c) Amplitude vs Real part eigenvalues; MATLAB code applied on DDES data of the fan simulator case.

Figure 5-15 shows the same parameters previously described in Figure 5-11 and a certain accordance with Jovanović et al. [49] can be underlined. However, the real aim of this section is not to enter into the physical meaning or into a careful analysis of the outputs obtained for the DDES simulation of the S-duct. On the other hand, what is achieved in this work is a first important step to the implementation of a code related to SP-DMD applicable to all data processed through CUdatapro inside Cranfield University.

6 CONCLUSIONS AND RECCOMENDATIONS

In this project both a steady (RANS) and a transient (DDES) simulation of an S-duct with a fan simulator at the AIP plane are carried out. The geometry studied is the high off-set with $H/L=5.0$ at an inlet Mach number of 0.27. Moreover, a comparison of the contours and the descriptors determined from the simulations with A. Soli's case [12] is accomplished. Finally, a first attempt to study and to apply the Dynamic Mode Decomposition for the post-processing of the result is done.

6.1 Main findings

Firstly, the analysis of the velocity and pressure field by means of the contours of the RANS simulation allowed the description of the flow field inside the S-duct. The attention was focused mainly on the downstream region, approaching the AIP. The typical flow field distribution already investigated in previous works in Cranfield University is observed. Basically, the presence of a separated region at the bottom wall triggered by the first compression bend is present, with the consequent development of a total pressure and an out-of-plane velocity defect. The streamwise vortices generated propagate to the AIP section. At the exit plane of the S-duct, the so referred AIP, the analysis of the transient data was accomplished in order to have a better understanding of the unsteadiness levels. The contours analysed in terms of velocity and pressure fields, averaging all the time-steps of the DDES, showed the presence of two spoiled regions; the largest below the spinner and a smaller one at $+90^\circ$ position above the spinner. The limits of a RANS simulation compared to a DDES were underlined by comparison of PR contours at the AIP section. Not only the shape but also the dimension of the spoiled regions were differently approximated showing in particular an underestimation of the separated region at the AIP plane using the RANS. Furthermore, a comparison with A. Soli's transient simulation [12] is accomplished. In this case it is possible to highlight the impact of the fan simulator on the flow. First of all, the action of the fan simulator seems to decrease the dimension of the separation at the $+90^\circ$ position on the AIP section. At the same time, the spinner constraints the bottom separation to a

smaller region, if compared to the case without spinner. In general a reshape of the flow around the obstacle, namely the spinner itself, is observed. Another important study done is related to the analysis of the 3D boundary layer separation happening upstream and comparing it with both RANS and A. Soli's transient simulation [12]. In first place, an underestimation of the dimensions of the separated region is highlighted using the RANS method, comparing it with the DDES data. However, no appreciable difference in terms of both position and dimension of the separation is underlined comparing the results of the geometry with the fan simulator and the clean case of A. Soli [12]. As a consequence, the presence of the static fan is not felt upstream, namely it is not affecting the flow field inside the S-duct in the upstream region.

A second important investigation accomplished is related to the analysis of flow distortion descriptors in terms of both total pressure and swirl. First of all, the most important time-averaged and area-averaged descriptors were presented for the DDES of the fan case and they were also compared to the RANS simulation of the same geometry and the DDES of the clean case. A good agreement between the steady and the transient simulation is observed. However, the analysis of the averaged behaviour of the descriptors is not considered accurate enough for the purposes of this work and consequently a more detailed analysis at ring 3,4 and 5 is carried out. By comparison of the cloud maps of the two transient simulations on the two geometries, fundamental behaviours are highlighted. First of all, the shape of the flow is different in the two configurations, moving from a bulk swirl pattern at the AIP of the clean case, to a twin swirl at the AIP of the fan case. The engine tends to reshape the flow field at the AIP from a bulk swirl to a twin swirl. In addition, introducing the fan simulator at the exit of the S-duct, the swirl intensity at ring 3 and 4 is reduced by almost 50%. Consequently, the decrease of SI observed by introducing the engine face, is followed by a decrease in the actual swirl distortion level at the AIP plane. A probability of $P=14.62\%$ to have a twin swirl is observed at ring 5 of the fan case while a value of $P=4.1\%$ in the clean case for a range of $SP [0.95, 1.05] \times SD [-0.1, 0.1]$. Similarly a probability to have a SI

in the range of SI $[6^\circ, 8^\circ]$ x SD $[-0.1, 0.1]$ is $P=7.72\%$ in the fan case while $P=3.20\%$ in the clean case.

The last outcome of this project is related to the work and the effort put into the study and implementation of the cutting edge post-processing method called Dynamic Mode Decomposition and in particular to the Sparsity-Promoting DMD. The first part of the work was related to the understanding of the advantages and disadvantages of the method as well as the mathematics and the methodology to follow in order to have a correct algorithm. Compared to other decomposition techniques such as POD, it does not use energy to describe the flow and the DMD eigenvalues have no order despite frequencies [51]. Consequently, unlike the POD method, DMD decomposition leads to growth rates and frequencies associated to each mode determined from the magnitude and phase of each corresponding eigenvalue. Moreover, DMD does not use second order statistics as an approximation of the decomposition [51]. In particular the two most important advantages of the DMD are [47]:

1. Compared to a Proper Orthogonal Decomposition (POD), time evolution is available for each mode obtained from the DMD study [47].
2. Time averaged description of the flow is present inside DMD modes [47].

Consequently, the DMD method allows a better approximation of the flow by means of the modes computed by the algorithm [47].

The second step done is related to the understanding and verification of the MATLAB code written by Jovanović et al. [49] for the purposes of their scientific paper. In particular in Chapter 4, not only the figures underlined the agreement between the analysis of Jovanović et al. [49] and the code personally used, but also they provided a better comprehension of the inputs, outputs and features of the DMD. First of all, eigenvalues plotted in a complex plane follow a circular law and if they fall inside a damped behaviour is observed. Moreover, if a negative value of the real part of the selected eigenvalues is observed, modes are stable. Finally, the eigenvalues positioned in the positive range but at a zero value of the imaginary part are related to the modes which capture only the mean flow [60]. Eigenvalues close to zero capture the mean flow and the most dominant structures evolving in time [60].

The third step in the SP-DMD analysis is mainly related to the modification of the code in order to introduce not only the transient data at the AIP plane of the fan case simulation but in general every data processed with CUDatapro. This must be regarded as a very basic but fundamental and needed step.

6.2 Recommendations for future research

One of the main aspects that emerged from this project is related to the importance of the DMD as a tool for post-processing not only CFD simulations but also experimental data. For this reason, it is considered of paramount importance for future research to improve the code written by Jovanović et al. [49] adopting the new version personally modified during this project in order to plot not only eigenvalues and performance behaviours but also the modes within the flow and all the other parameters presented in Chapter 5. Basically, a real investigation of the data using the code presented have to be made. It can be considered useful to rewrite the code using an open source software such as Python™. Furthermore, in order to have a more specific understanding of the advantages of the DMD related to the investigations of complex intakes, a comparison between the already developed POD method and the new SP-DMD algorithm can be considered an interesting and useful analysis.

Looking at the current research and the industrial interest in complex intakes, new geometries and configurations should be investigated in order to understand the impact of swirl and total pressure distortion on the main parameters of the engine such as SFC and efficiencies, following an approach similar to J. Marty et al. [45]. Basically, starting from the AIP plane data obtained in this work, a CFD analysis of the first compressor stage may give detailed information of the impact of the distortion levels on the performance of the engine. Similarly, the introduction of a rotary fan can provide a more realistic description of the flow distortion in the S-duct.

In addition, a study that was not applied so far is to simulate the flow using only the spinner, without the blades and the other parts of the static fan geometry. In particular, this may decrease the computational time of the DDES simulation offering the possibility to use a finer mesh obtaining a more detailed description

of the flow. The assumption behind this simplification of the geometry is that the highest impact on the flow field is related to the presence of the spinner itself, which is one of the outcomes of the work carried out in this project.

REFERENCES

- [1] G. Tanguy, P. Zachos, D. G. MacManus, D. Gil-Prieto, and E. Garnier, "Passive flow control study in a convoluted intake using Stereo Particle Image Velocimetry," in *34th AIAA Applied Aerodynamics Conference*, 2016, no. June, p. 3563.
- [2] D. G. MacManus, N. Chiereghin, D. G. Prieto, and P. Zachos, "Complex Aeroengine Intake Ducts and Dynamic Distortion," *AIAA J.*, vol. 55, no. 7, pp. 2395–2409, Apr. 2017.
- [3] P. K. Zachos, D. G. MacManus, D. G. Prieto, and N. Chiereghin, "Flow Distortion Measurements in Convoluted Aeroengine Intakes," *AIAA J.*, vol. 54, no. 9, pp. 2819–2832, Jun. 2016.
- [4] D. Gil-Prieto, D. G. MacManus, P. K. Zachos, G. Tanguy, and K. R. Menzies, "Convoluted Intake Distortion Measurements Using Stereo Particle Image Velocimetry," *AIAA J.*, vol. 55, no. 6, pp. 1878–1892, 2017.
- [5] M. Gunston, B., Daly, *Jane's Aero-Engines*. Jane's Information Group, 2011.
- [6] R. A. Watson, P. P. G. Tucker, and K. Menzies, "Unsteady Simulations of the Wellborn Diffusing S-Duct," in *54th AIAA Aerospace Sciences Meeting*, no. January, American Institute of Aeronautics and Astronautics, 2016, pp. 1–12.
- [7] C. S. Thomas, K. I. Hume, and P. D. Hooper, "Aircraft Noise, Airport Growth and Regional Development," in *10th AIAA/CEAS Aeroacoustics Conference*, 2004, pp. 1–17.
- [8] D. Gil-Prieto, D. G. Macmanus, P. K. Zachos, G. Tanguy, and F. Wilson, "Dynamic flow distortion investigation in an S-duct using DDES and SPIV data," *34th AIAA Appl. Aerodyn. Conf.*, no. June, pp. 1–21, 2016.
- [9] D. Gil-Prieto, D. G. MacManus, P. K. Zachos, G. Tanguy, F. Wilson, and N. Chiereghin, "Delayed Detached-Eddy Simulation and Particle Image

- Velocimetry Investigation of S-Duct Flow Distortion,” *AIAA J.*, vol. 55, no. 6, pp. 1–16, 2017.
- [10] P. Zachos, D. G. MacManus, and N. Chiereghin, “Flow distortion measurements in convoluted aero engine intakes,” *33rd AIAA Appl. Aerodyn. Conf.*, no. June, pp. 1–24, 2015.
- [11] S16 Turbine Engine Inlet Distortion Committee., “A Methodology for Assessing Inlet Swirl Distortion.,” *Soc. Automot. Eng.*, no. AIR5686, p. 110, 2009.
- [12] A. Soli, “Flow Distortion analysis in S-Ducts using DDES,” Msc Thesis, Cranfield University, 2016.
- [13] F. Wilson, “CFD analysis of the flow field generated by convoluted ducts,” MSc Thesis, Cranfield University, 2014.
- [14] A. Delot, T. M. Berens, M. Tormalm, M. Säterskog, and N. Ceresola, “DES Computations for a Subsonic UAV Configuration with a Highly Integrated S-Shaped Inlet Duct,” in *52nd Aerospace Sciences Meeting*, 2014, vol. AIAA 0723, no. January, pp. 1–44.
- [15] N. C. Bissinger and T. Breuer, “Basic principles-Gas turbine Compatibility-Intake Aerodynamic Aspects,” in *Encyclopedia of Aerospace Engineering*, Wiley, 2010.
- [16] D. Nalianda, *Propulsion systems Performance and Integration: volume 1*. Cranfield University, 2017.
- [17] A. El-sayed and M. S. Emeara, “Intake of aero-engines: a case study,” in *The International conference of engineering sciences & applications*, 2016, no. February.
- [18] “Gas Turbine Engine Inlet Flow Distortion Guidelines,” *Soc. Automot. Eng.*, no. ARP 1420B, Jul. 2011.
- [19] “Inlet Total-Pressure-Distortion Considerations for Gas-Turbine Engines,” *Soc. Automot. Eng.*, vol. AIR1419B, May 2013.

- [20] N. Chiereghin, D. MacManus, M. Savill, and R. Dupuis, "Dynamic Distortion Simulations for Curved Aeronautical Intakes," in *Advanced Aero Concepts, Design and Operation*, 2014, no. July.
- [21] T. H. Okiishi, S. R. Wellborn, and B. A. Reichert, "An experimental Investigation of the flow in a diffusing S-Duct," in *28th joint propulsion conference and exhibit*, 1992, vol. AIAA, no. 3622.
- [22] A. Delot and R. K. Dr Scharnhorst, "A Comparison of Several CFD Codes with Experimental Data in a Diffusing S-Duct," in *49th AIAA/ASME/SAE/ASEE Joint Propulsion Conference*, 2013, vol. AIAA 3796, pp. 1–25.
- [23] N. Cumpsty, *Jet propulsion: A simple guide to the aerodynamic and thermodynamic design and performance of jet engines*, 2nd edn. Cambridge University Press, 2007.
- [24] J. Seddon and E. L. Goldsmith, *Intake aerodynamics*, 2nd Edn. AIAA Education Series, 1999.
- [25] B. K. Hodder, "An investigation of Engine Influence On Inlet Performance," 1981.
- [26] D. L. Motycka, "Reynolds number and fan/inlet coupling effects on subsonic transportinlet distortion," *J. Propuls. Power*, vol. 1, no. 3, pp. 229–234, May 1985.
- [27] G. M. Callahan and A. H. Stenning, "Attenuation of inlet flow distortion upstream of axial flow compressors," *J. Aircr.*, vol. 8, no. 4, pp. 227–233, Apr. 1971.
- [28] J. M. Delery, *Three-Dimensional Separated Flow Topology: Singular Points, Beam Splitters and Vortex Structures*. Wiley, 2013.
- [29] P. A. Davidson, *Turbulence: an introduction for scientists and engineers*, 2nd Edn. Oxford University Press, 2015.
- [30] O. Zikanov, *Essential computational fluid dynamics*. Wiley, 2010.

- [31] F. R. Menter, "AIAA 93 · 2906 Zonal Two Equation $k - \omega$ Turbulence Models for Aerodynamic Flows . Mailing Address : 24th Fluid Dynamics Conference FOR AERODYNAMIC FLOWS," 1993.
- [32] P. R. Spalart, "Detached-Eddy Simulation," *Annu. Rev. Fluid Mech.*, vol. 41, no. 1, pp. 181–202, Aug. 2009.
- [33] F. R. Menter and M. Kuntz, "Adaptation of Eddy-Viscosity Turbulence Models to unsteady separated flow behind vehicles," in *Lecture Notes in Applied and Computational Mechanics*, vol. 19, Springer, 2004, pp. 339–352.
- [34] R. Spalart, "Young-Person's Guide Simulation Grids Detached-Eddy," *NASA Tech. Note*, vol. 211032, no. July, pp. 1003–1008, 2001.
- [35] P. R. Spalart, S. Deck, M. L. Shur, K. D. Squires, M. K. Strelets, and A. Travin, "A new version of detached-eddy simulation, resistant to ambiguous grid densities," *Theor. Comput. Fluid Dyn.*, vol. 20, no. 3, pp. 181–195, May 2006.
- [36] A. Giacomobello, "Complex aero-engine intake aerodynamics and flow distortion," MSc Thesis, Cranfield University, 2016.
- [37] Ansys, "ANSYS ICEM CFD 17.1 Tutorial Manual," vol. 15317, no. November, pp. 1–1294, 2016.
- [38] ANSYS, "ANSYS FLUENT User's Guide," *ANSYS FLUENT User's Guid.*, vol. 15317, no. November, p. 2498, 2016.
- [39] T. M. Berens, A. Delot, M. Chevalier, and J. van Muijden, "Numerical Simulations for High Offset Intake Diffuser Flows," *AIAA SciTech*, no. 13–17 January, pp. 1–28, 2014.
- [40] P. J. Roache, *Verification and validation in computational science and engineering*. Hermosa, 1998.
- [41] J. W. Slater, "Examining spatial (grid) convergence.," 2008. [Online]. Available:

<https://www.grc.nasa.gov/www/wind/valid/tutorial/spatconv.html>.
[Accessed: 13-Jul-2017].

- [42] S. R. Wellborn, B. A. Reichert, and T. H. Okiishi, "Study of the compressible flow in a diffusing S-duct," *J. Propuls. Power*, vol. 10, no. 5, pp. 668–675, Sep. 1994.
- [43] E. Garnier, "Flow Control by Pulsed Jet in a Curved S-Duct: A Spectral Analysis," *AIAA J.*, vol. 53, no. 10, pp. 2813–2827, Aug. 2015.
- [44] L. H. O. Hellström, M. B. Zlatinov, G. Cao, and A. J. Smits, "Turbulent pipe flow downstream of a 90° bend," *J. Fluid Mech.*, vol. 735, Oct. 2013.
- [45] J. Marty, R. Barrier, and E. Garnier, "Impact of distortions due to separation in S-duct inlet on compressor stage behavior and performances," in *23rd AIAA Computational Fluid Dynamics Conference*, American Institute of Aeronautics and Astronautics, 2017.
- [46] R. P. M. Rademakers, S. Bindl, and R. Niehuis, "Effects of Flow Distortions as They Occur in S-Duct Inlets on the Performance and Stability of a Jet Engine," *J. Eng. Gas Turbines Power*, vol. 138, no. 2, 2015.
- [47] H. Koizumi, S. Tsutsumi, and T. Haga, "Sparsity-Promoting Dynamic Mode Decomposition Analysis on Aeroacoustics of a Clustered Supersonic Jet," in *23rd AIAA Computational Fluid Dynamics Conference*, 2017, no. June, pp. 1–19.
- [48] R. Larusson, M. Olander Burak, N. Andersson, and J. Östlund, "Dynamic Mode Decomposition applied to a Detached-Eddy Simulation of Separated Nozzle Flow," in *55th AIAA Aerospace Sciences Meeting*, American Institute of Aeronautics and Astronautics, 2017.
- [49] D. Lengani, D. Simoni, M. Ubaldi, P. Zunino, and F. Bertini, "Experimental Investigation on the Time-Space Evolution of a Laminar Separation Bubble by POD and DMD," no. 49705, pp. 1–22, 2016.

- [50] Y. T. D. Frankel, K. Anupindi, A.-E. M. Kerlo, M. D. Rodefled, and H. F. Steven, “Dynamic mode decomposition of Fontan hemodynamics in an idealized total cavopulmonary connection,” *Fluid Dyn. Res.*, vol. 46, no. 4, Jul. 2014.
- [51] P. J. Schmid, “Dynamic mode decomposition of numerical and experimental data,” *J. Fluid Mech.*, vol. 656, no. July 2010, pp. 5–28, 2010.
- [52] K. K. Chen, J. H. Tu, and C. W. Rowley, “Variants of dynamic mode decomposition: Boundary condition, Koopman, and fourier analyses,” *J. Nonlinear Sci.*, vol. 22, no. 6, pp. 887–915, 2012.
- [53] G. B. Philip Holmes, John L. Lumley, *Turbulence, Coherent Structures, Dynamical Systems and Symmetry*, 2nd Edn. Cambridge University Press, 1998.
- [54] B. R. Noack *et al.*, “A finite-time thermodynamics of unsteady fluid flows,” *J. Non-Equilibrium Thermodyn.*, vol. 33, no. 2, pp. 103–148, 2008.
- [55] I. Mezić, “Analysis of Fluid Flows via Spectral Properties of the Koopman Operator,” *Annu. Rev. Fluid Mech.*, vol. 45, no. 1, pp. 357–378, 2013.
- [56] C. Pan, J. Wang, J. Wang, and M. Sun, “Dynamics of an unsteady stagnation vortical flow via dynamic mode decomposition analysis,” *Exp. Fluids*, vol. 58, no. 3, p. 21, 2017.
- [57] M. R. Jovanović, P. J. Schmid, and J. W. Nichols, “Sparsity-promoting dynamic mode decomposition,” *Phys. Fluids*, vol. 26, no. 2, pp. 1–22, 2014.
- [58] A. Edelman, “The Circular Law and the Probability that a Random Matrix Has k Real Eigenvalues,” pp. 1–20, 1993.
- [59] V. Girko, “Circular Law,” *Theory Probab. Its Appl.*, vol. 29, no. 4, pp. 694–706, Jan. 1985.
- [60] P. J. Schmid, L. Li, M. P. Juniper, and O. Pust, “Applications of the

dynamic mode decomposition,” *Theor. Comput. Fluid Dyn.*, vol. 25, no. 1, pp. 249–259, May 2011.

- [61] G. H. Golub and C. Reinsch, “Singular value decomposition and least squares solutions,” *Numer. Math.*, vol. 14, no. 5, pp. 403–420, 1970.

APPENDICES

Appendix A

A.1 Basic definitions: critical points and skin friction lines

Usually separation phenomena in three dimensions is dependent on two factors: the flow properties close to the surface of the object, namely it is linked to the Reynolds number, and the presence of local singularities. A more practical way of defining and studying separation based on data coming from both experiments or CFD simulations, allows us to describe the flow field structure in space, starting from its own trace on a surface. The following sections will explain the right way to achieve this.

Looking at a flow over a body of surface S defined in a orthonormal local system described by the following unit vectors $(\vec{n}, \vec{i}, \vec{j})$, respectively along the normal direction and in the tangential plane of the surface, the interaction between the two produces a force F that can be written as $\vec{F} = \vec{P}dS$ [28]. The term \vec{P} in particular is the vector tension that can be decomposed along the surface itself in a normal component $(p\vec{n})$, namely the normal action of pressure, and a tangential stress $(\vec{\tau})$, obtaining $\vec{P} = -p\vec{n} + \vec{\tau}$ [28]. Consequently, for a three dimensional flow the shear stress is a vector; it can be written as (eq. (A-1)):

$$\vec{\tau} = \tau_x \vec{i} + \tau_y \vec{j} \quad (\text{A-1})$$

Where, considering a Newtonian fluid, $\tau_x = \mu_x \left(\frac{\partial u}{\partial y} \right)_w$ and $\tau_z = \mu_w \left(\frac{\partial w}{\partial y} \right)_w$. In order to understand the formula better, see Appendix A.2.

Starting from the preceding equation, the shear stress on a surface is defined as a vector field and the solution of this field, i.e. the solution of the differential system (eq. (A-2)), is a family of curves called streamlines or lines of force of the vector field [28].

$$\frac{dx}{\tau_x(x, z)} = \frac{dy}{\tau_z(x, z)} = dt \quad (\text{A-2})$$

Calling t the integration parameter, the solution of eq. (A-2) at the surface are referred to as skin friction lines, having the property to be tangent to the local skin friction vector at the contact point [28]. As a matter of fact, the general solution of the vector field (streamlines) tends to become a skin friction line approaching as it approaches the walls, where the velocity is zero. The use of skin friction lines is particularly convenient to describe the flow since they can be determined with experiments or calculations.

The general rule of a skin friction line on a body, solution of the system expressed by eq. (A-26), is that only one line passes through one point on the surface. However, there are some points that do not respect this rule and more than one line passes through them; these points are called critical points of the system and simultaneously it is possible to have $\tau_x(x, z) = 0$ and $\tau_z(x, z) = 0$ [28]. Depending on the geometrical properties of the skin friction lines close to these points, different types of critical points can be specified and three categories are presented:

1. Node points
2. Saddle points
3. Focus points

In the first case, all the lines, except for one, passing through the point have a common tangent. The second one has only two lines crossing the critical point, while the others have a hyperbolic shape. As far as saddle points are concerned instead, all the lines collapse at the critical point spiralling around it [28]. Each point is represented in Figure A-1.

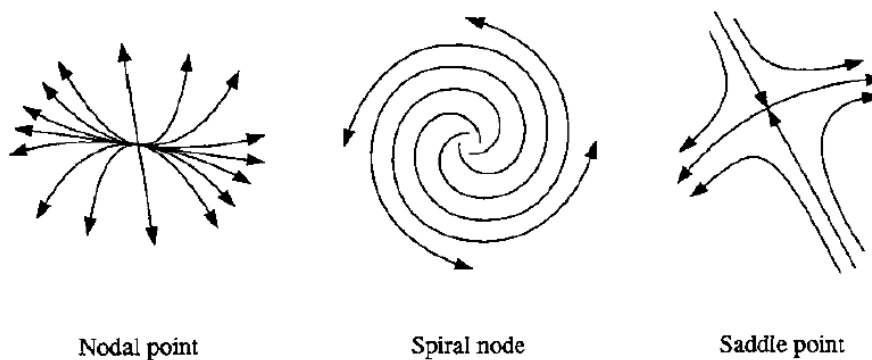


Figure A-1 Critical points usually observed in separation phenomena [28].

A.2 : 3D boundary layer

Usually the velocity profile in a 3D boundary layer is defined in a curvilinear system, where the longitudinal Ox axis is defined in the direction of the velocity \vec{V}_e , the axis Oz is perpendicular to Ox and on the plane tangent to the surface of the body and finally Oy normal to the body surface. The velocity field inside the 3D boundary layer is defined using two functions in Ox and Oz direction, basically considering zero the velocity in the normal direction (Oy) [28]. These two components are:

1. Streamwise function: $u/u_e = f(y)$
2. Crosswise function: $w/u_e = g(y)$

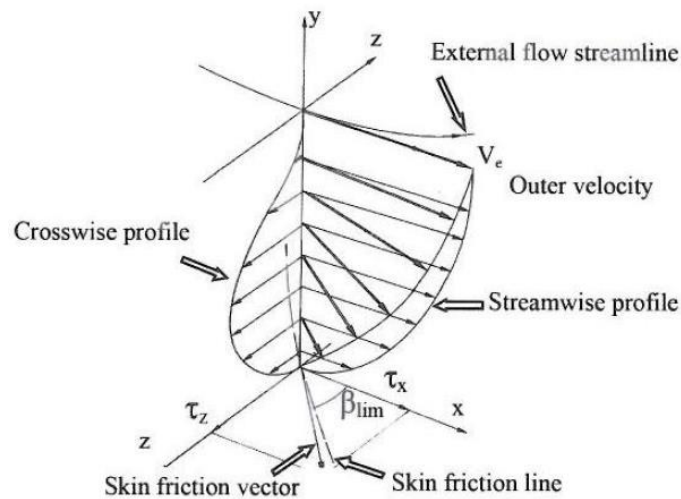


Figure A-2 3D boundary layer structure [28].

Looking at Figure A-2 and following the definition of the reference system, the value of w tends to zero as it approaches the boundary with the external flow streamline. This means that the flow tends to be parallel to the stream direction, or Ox . The crosswise function and in particular the value of w , describe the 3D effect on the flow, namely the distortion inside the boundary layer and it is represented by the distortion angle $\beta = \tan^{-1}(w/u)$ [28]. Moving towards the wall instead, both u and w components tends to zero and it is possible to express these two variables with an expansion, shown in eq. (A-3):

$$u = y \left(\frac{\partial u}{\partial y} \right)_w ; w = y \left(\frac{\partial w}{\partial y} \right)_w \quad \text{(A-3)}$$

And at the same time the value of β at the wall is (eq. (A-4)):

$$\beta_{lim} = \tan^{-1} \left[\frac{\left(\frac{\partial w}{\partial y} \right)_w}{\left(\frac{\partial u}{\partial y} \right)_w} \right] = \tan^{-1} (\tau_z / \tau_x) \quad (\text{A-4})$$

Comparing a 3D with a 2D boundary layer, the main difference is related to the fact that in the 3D case the flow creates a transverse component of velocity, defined as w . In the 2D instead the flow remains developed on a plane. The presence of a third dimension in the flow field introduces a new movement in the lateral direction of the flow itself, leading to a lower value of pressure gradients in the 3D case compared to the 2D boundary layer. This means that the flow in a 2D boundary layer will be subject to larger accelerations and deceleration during its movement [28].

The presence of another flow direction leads to a more complex phenomena and consequently greater difficulties in the mathematical modelling. However, in the real situations 2D boundary layers are rarely observed while a 3D development is more often seen [28].

Appendix B

B.1 Singular Value Decomposition Method

This section gives a better description of the SVD method introduced in 5.2.1. The same notations in terms of the matrix will be used. V_1^{N-1} is a matrix $M \times N$ whose entries comes from the field $K \in \mathbb{C}$ and $v_i \in \mathbb{C}^M$, then there exists a factorization, called a singular value decomposition of V_1^{N-1} , of the form (eq. (B-1)) [61]:

$$V_1^{N-1} = U \Sigma W^* \quad (\text{B-1})$$

Where U is a $M \times N$ unitary matrix, namely $U U^* = U^* U = I$ and the columns of U are the eigenvectors of $V_1^{N-1} V_1^{N-1*}$. W is a $n \times n$ unitary matrix (similarly to U) but the columns are the eigenvectors of $V_1^{N-1*} V_1^{N-1}$. Finally, Σ is a diagonal matrix $M \times N$ with non-negative real numbers on the diagonal. The terms on the

diagonal are the singular values of V_1^{N-1} , namely the square root of the eigenvalues of $V_1^{N-1}V_1^{N-1*}$ or $V_1^{N-1*}V_1^{N-1}$ arranged in a descending order [61]. In particular with reference to section 5.2.1, in eq. (B-1), V_1^{N-1} is known from the input data of the flow field and consequently it is possible to apply the SVD method. U , matrix of the POD modes.

Eq. (2-35) is derived in the following way starting from eq. (B-2):

$$V_2^N = AV_1^{N-1} + re_{N-1}^T \quad (\text{B-2})$$

By multiplying by U^* previously determined from the SVD decomposition and rearranging the equation (eq. (B-3)):

$$\tilde{S} = U^*AU = U^*V_2^N W \Sigma^{-1} \quad (\text{B-3})$$

From this expression then we can determine the eigenvalues and eigenvectors of \tilde{S} and consequently the dynamic modes. If r is the rank of V_1^{N-1} and it is a matrix $M \times N$, than [61]:

- $U \in \mathbb{C}^{M \times r}$
- $W \in \mathbb{C}^{r \times M}$
- $\tilde{S} \in \mathbb{C}^{r \times r}$
- $A \in \mathbb{C}^{M \times M}$
- $\Sigma = \text{diag}(\sigma_1 \dots \sigma_r)$

B.2 DMD algorithm

B.2.1 ADMM

ADMM is an iterative algorithm that minimize the augmented Lagrangian multiplier. Basically it composed by three steps [57]:

1. α -minimization
2. β -minimization
3. Lagrangian multiplier update

The Lagrangian multiplier is a function that redefine the Sparsity-promoting problem (eq. (3-9)) by introducing a new variable β and obtaining eq. (B-4):

$$L_\rho = J(\alpha) + \gamma g(\beta) + 0.5(\lambda^*(\alpha - \beta) + (\alpha - \beta)^*\lambda + \rho\|\alpha - \beta\|_2^2) \quad (\text{B-4})$$

where $g(\beta) = \sum_{i=1}^r |\beta_i|$ redefine the expression of eq. 3-10 with a variable change. ρ is a positive parameter that determines the rate of convergence of the algorithm [57].

- *α -minimization step:* in general terms it means that we are looking for the minimization of $\alpha^{k+1} := \arg \min_\alpha L_\rho(\alpha, \beta^{k+1}, \lambda^{k+1})$. In practical terms the solution is obtained with the following eq. (B-5) [57]:

$$\alpha^{k+1} = (\mathbf{P} + (\rho/2)\mathbf{I})^{-1}(\mathbf{q} + (\rho/2)\mathbf{u}^k) \quad (\text{B-5})$$

- *β -minimization step:* a general expression for this process is expressed by $\beta^{k+1} := \arg \min_\beta L_\rho(\alpha^{k+1}, \beta, \lambda^k)$ and consequently the solution is obtained from eq. (B-6) [57]:

$$\beta^{k+1} = S_k(v_i^k), k = \gamma/\rho \quad (\text{B-6})$$

and in particular S_k is a thresholding operator in the form of eq. (B-7):

$$\begin{cases} v_i^k - k, & v_i^k > k \\ 0, & v_i^k \in [-k, k] \\ v_i^k + k, & v_i^k < -k \end{cases} \quad (\text{B-7})$$

- *Lagrangian multiplier update:* in this case the expression is (eq. (B-8)) [57]:

$$\lambda^{k+1} = \lambda^k + \rho(\alpha^{k+1} + \beta^{k+1}) \quad (\text{B-8})$$

The iterations are conducted until the following relation is respected (eq. (B-9)):

$$\|\alpha^{k+1} - \beta^{k+1}\|_2 < \varepsilon_{prim} \text{ and } \|\beta^{k+1} - \beta^k\|_2 < \varepsilon_{dual} \quad (\text{B-9})$$

where ε are the desired tolerances [57].

B.2.2 Algorithm: second minimization

As stated in section 5.2.1.2, the second minimization is the resolution of the problem expressed by eq. (3-11) where the $J(\alpha)$ is given by eq. (3-10). Starting from the definition of the Lagrangian of eq. (B-4), its variation can be expressed in the following way (eq. (B-10)) [57]:

$$L_{\rho}(\alpha, \nu) = J(\alpha) + \nu^*(E^T \alpha) + (E^T \alpha)^* \nu \quad \text{(B-10)}$$

where ν is the Lagrangian multiplier. The eq. (B-10) can be solved in order to find the optimal L_{ρ} that gives the optimal sparse vector α_{sp} . After some algebra the value of α_{sp} can be computed with eq. (B-11) [57]:

$$\alpha_{sp} = \begin{bmatrix} \mathbf{I} & \mathbf{0} \end{bmatrix} \begin{bmatrix} \mathbf{P} & \mathbf{E} \\ \mathbf{E}^T & \mathbf{0} \end{bmatrix} \begin{bmatrix} q \\ 0 \end{bmatrix} \quad \text{(B-11)}$$